Title
Numerical and experimental investigations of the head/disk interface

Author
Duwensee, Maik

Publication Date
2007

Peer reviewed|Thesis/dissertation

UNIVERSITY OF CALIFORNIA, SAN DIEGO

Numerical and Experimental Investigations of the Head/Disk Interface

A dissertation submitted in partial satisfaction of the
requirements for the degree
Doctor of Philosophy

in

Engineering Sciences (Mechanical Engineering)

by

Maik Duwensee

Committee in charge:

Professor Frank E. Talke, Chair
Professor David J. Benson
Professor Thomas Bewley
Professor Eric Fullerton
Professor Jack Keil Wolf

2007

The dissertation of Maik Duwensee is approved, and it is acceptable in quality and form for publication on microfilm:

_____

_____

_____

_____

_____
Chair

University of California, San Diego

2007

to my parents Bärbel† and Dieter Duwensee

TABLE OF CONTENTS

LIST OF FIGURES

LIST OF TABLES

ACKNOWLEDGEMENTS

First of all, I would like to thank Professor Frank E. Talke for inviting me to the Center for Magnetic Recording Research (CMRR) at the University of California, San Diego. Without his advise and support this thesis would not have been possible. He helped me getting started with "magnetic recording" and provided me with the equipment and advise I needed. His encouragement and tireless effort in pointing out mistakes and corrections in my publications and this thesis were necessary and very valuable.

Many people contributed to the success of this thesis. I would like to thank the members of Professor Talke's group, current and former, who were very helpful during my research and provided a warm working environment. In particular I would like to thank Dr. Saurabh Deoras, and my office mate for years Aravind Murthy for countless discussions and fruitful conversations. I am especially grateful to Dr. Eric Jayson for proof reading this thesis. Dr. Peter Baumgart and Dr. Bernhard Knigge were of great support throughout my time at the CMRR and especially during my summer internship at Hitachi GST. I am looking forward working with them at Hitachi GST.

I am very grateful to Marcia Levitt, Betty Manoulian, and Iris Villanueva for their help and support during my time at the Center for Magnetic Recording Research.

Acknowledgement for published work:

The text of chapter 2 is a partial reprint of material as it appears in: "***Voltage Pulsing for Localized Clearance Measurements***", by Maik Duwensee, Bernhard Knigge, Peter Baumgart, and Frank E. Talke, IEEE Transactions on Magnetics, vol.41, no.12, p.4454-4456, (2005). The dissertation author was the primary researcher and author and the co-authors listed in this publication directed and supervised the research which forms the basis for chapter 2.

The text of chapter 3 is a partial reprint of material as it appears in: "***A Scanning Method to Study the Influence of Roughness, Microwaviness, and Lubricant Thickness Variation on Slider Dynamics***", by Maik Duwensee, Bernhard Knigge, Peter Baumgart, and Frank E. Talke, World Tribology Congress III. September 12-16, 2005, Washington, D.C. USA. The dissertation author was the primary researcher and author and the co-authors listed in this publication directed and supervised the research which forms the basis for chapter 3.

The text of chapter 5 is a partial reprint of material as it appears in:

- "***Air Bearing Simulation of Discrete Track Recording Media***", by Maik Duwensee, Shoji Suzuki, Judy Lin, David Wachenschwanz, and Frank E. Talke, IEEE Transactions on Magnetics, vol.42, no.10, p. 2489 - 2491, (2006)

- "***Simulation of the Head/Disk Interface for Discrete Track Media***", by Maik Duwensee, Shoji Suzuki, Judy Lin, David Wachenschwanz, and Frank E. Talke, published online in Microsystem Technologies (2006).

The dissertation author was the primary researcher and author and the co-authors listed in these publications directed and supervised the research which forms the basis for chapter 5.

The text of chapter 7 is a partial reprint of material as it appears in: "***Direct Simulation Monte Carlo Method for the Simulation of Rarefied Gas Flow in Discrete Track Head/Disk Interfaces***", by Maik Duwensee, Shoji Suzuki, Judy Lin, David Wachenschwanz, and Frank E. Talke, submitted for publication to ASME Journal of Tribology (2007). The dissertation author was the primary researcher and author and the co-authors listed in this publication directed and supervised the research which forms the basis for chapter 7.

VITA

1993–1995	Apprenticeship, BMW AG, Munich, Germany
1995–2001	Study of Mechanical Engineering, University of Rostock, Germany
1998–1999	Research position Robert Bosch GmbH, Schwieberdingen, Germany
2001	German "Diplom-Ingenieur" degree, *Summa Cum Laude*, Mechanical Engineering, University of Rostock, Germany
2001–2002	Research Assistant, University of Rostock, Germany
2002–2007	Research and Teaching Assistant, Center for Magnetic Recording Research, University of California, San Diego
2004	M.S., Mechanical Engineering, University of California, San Diego
Summer 2004	Research position, Hitachi Global Storage Technology, San Jose, California
Summer 2005	Research position, Western Digital Inc., Fremont, California
2007	Ph. D., University of California, San Diego

PUBLICATIONS

Duwensee, M.; Heim, A., Woernle C.; *Vertikaldynamik von Straßenfahrzeugen mit Gas-Feder-Dämpfer-Elementen*, (English: Simulation of Vertical Dynamics of Cars with Air-Spring-Damper), PAMM, Volume 2, Issue 1, Published Online: Mar. 2003, Pages: 116 - 117

Duwensee, M.; Knigge, B.; Baumgart, P.; Talke, F.E.; *Voltage Pulsing for Localized Clearance Measurement*, IEEE Transactions on Magnetics, Volume 41, Issue 12, Dec. 2005, Pages: 4454 - 4456

Duwensee, M.; Suzuki, S.; Lin, J.; Wachenschwanz, D.; Talke, F.E.; *Air Bearing Simulation of Discrete Track Recording Media*, IEEE Transactions on Magnetics, Volume 42, Issue 10, Oct. 2006, Pages: 2489 - 2491

Duwensee, M.; Suzuki, S.; Lin, J.; Wachenschwanz, D.; Talke, F.E.; *Simulation of the Head/Disk Interface for Discrete Track Media*, Microsystem Technologies, Published Online: Nov. 2006

Suzuki, S.; Dorsey, P.; Nishihira, H.; Lin, J.; Wachenschwanz, D.; Duwensee, M.; Talke, F.E.; *Discrete Track Recording Media and its Tribological Challenges in Head/Disk Interface*, accepted for Journal of Japanese Society of Tribologists, Vol.52 No. 6, June 2007.

Duwensee, M.; Suzuki, S.; Lin, J.; Wachenschwanz, D.; Talke, F.E.; *Direct Simulation Monte Carlo Method for the Simulation of Rarefied Gas Flow in Discrete Track Head/Disk Interfaces*, submitted for publication to ASME Journal of Tribology, 2007

Duwensee, M.; Yoon, P.; Lee, D.E.; Suzuki, S.; Lin, J.; Wachenschwanz, D.; Peng, J.P.; Talke, F.E.; *Flyability Testing of Sliders on Patterned Media*, to be submitted to Microsystem Technologies, 2007

ABSTRACT OF THE DISSERTATION

Numerical and Experimental Investigations of the Head/Disk Interface

by

Maik Duwensee

Doctor of Philosophy in Engineering Sciences (Mechanical Engineering)

University of California San Diego, 2007

Professor Frank E. Talke, Chair

Experimental techniques were developed for the investigation of slider dynamics for ultra-low spacing head/disk interfaces. Voltage pulsing and mapping techniques were established for the investigation of clearance and flying height modulation as functions of head/disk interface parameters. Numerical methods were developed to analyze forces acting on sliders of discrete track recording head/disk interfaces. A finite-element-based air bearing simulator was used to predict the steady state flying characteristics of arbitrarily shaped slider contours flying over discrete track recording disks. The direct simulation Monte Carlo method was used to simulate the rarefied gas flow in nano-channels.

1

Introduction

This chapter provides a short introduction to the history of computer hard disk drives and the basic principles of magnetic recording. Additionally, the main components and functions of a computer hard disk drive are explained and illustrated, and the organization of this thesis is presented.

1.1 History of Computer Hard Disk Drives

The emerging computer industry in the middle of the twentieth century created a demand for high-capacity and fast access digital data storage. The magnetic storage of digital data provided a promising solution to fulfill this demand and became the main storage technology for digital data today. One can distinguish between two main magnetic storage principles, i.e., magnetic tape storage and

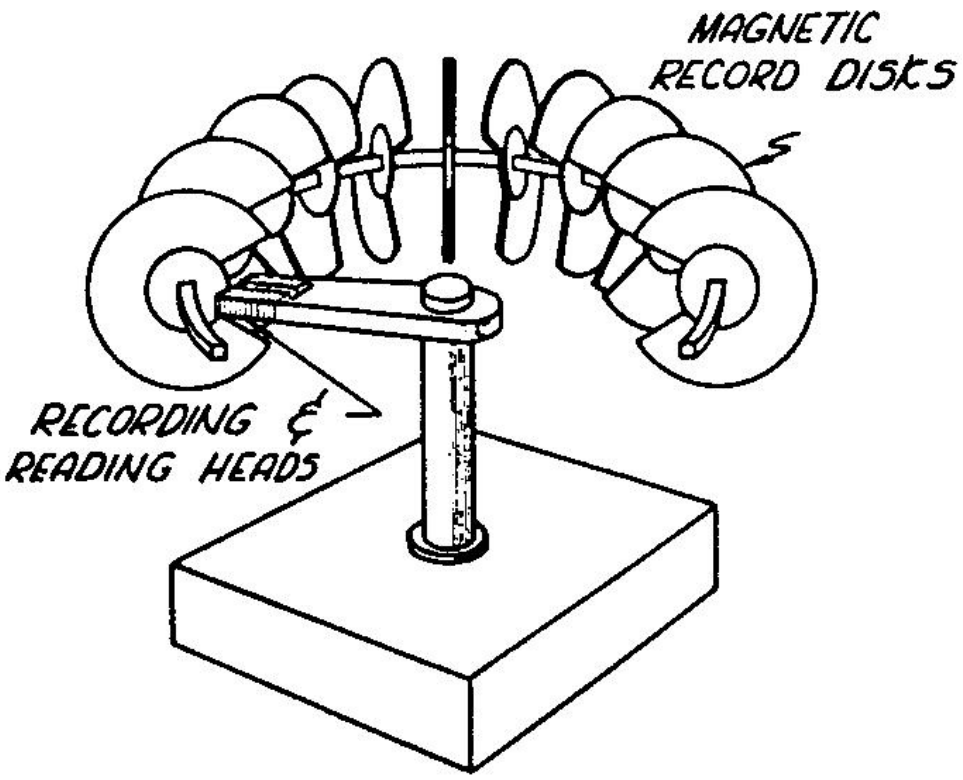

Figure 1.1: Schematic of notched-disk memory as suggested by Rabinow [32] (source [32])

magnetic disk storage. While tape is still the preferred backup and long term storage medium of digital data, it has always lacked fast data access times. An article written by Jacob Rabinow [32] from the National Bureau of Standards in August 1952 triggered the invention of what is known today as the computer hard disk drive. The article by Rabinow [32] dealt with "The Notched-Disk Memory." Figure 1.1 shows the storage device suggested by Rabinow. As can be seen in Figure 1.1, several magnetic disks were arranged on a circular shaft in the form

of a toroid. The magnetic heads were attached to a rotating shaft at the center of the disk-toroid. Each disk was equipped with an opening, the so-called notch. The notch was large enough to allow the magnetic heads to rotate freely about the center shaft. The magnetic heads were used to write and read information from the notched disks. For writing and reading of a certain disk, the heads were positioned in front of the disk. After positioning the heads, the disk was spun and the data could be written or read. A bank of radially aligned heads was used to maximize the area of the disks used for data storage. The information was stored in the form of magnetic pulses.

In 1956, a so-called Random Access Memory Accounting Machine (RAMAC) was demonstrated to the public by the International Business Machines (IBM) Corporation. The RAMAC is considered to be the first computer hard disk drive (HDD). The RAMAC consisted of fifty $24''$ diameter disks mounted vertically on a rotating shaft. The disks had a thickness of $0.1''$. Figure 1.2 shows a photograph of a RAMAC system [38]. The shaft revolved at 1200 rotations per minute (rpm). The disks were accessed by a single servo controlled read/write head. Each disk had 100 circular tracks, and 500 characters could be stored per track resulting in a total storage capacity of five megabytes ($5MB$). One megabyte refers to $1,000,000$ single bytes and one byte refers to 8bit. The data transfer rate of the RAMAC was $8,800$ characters per second.

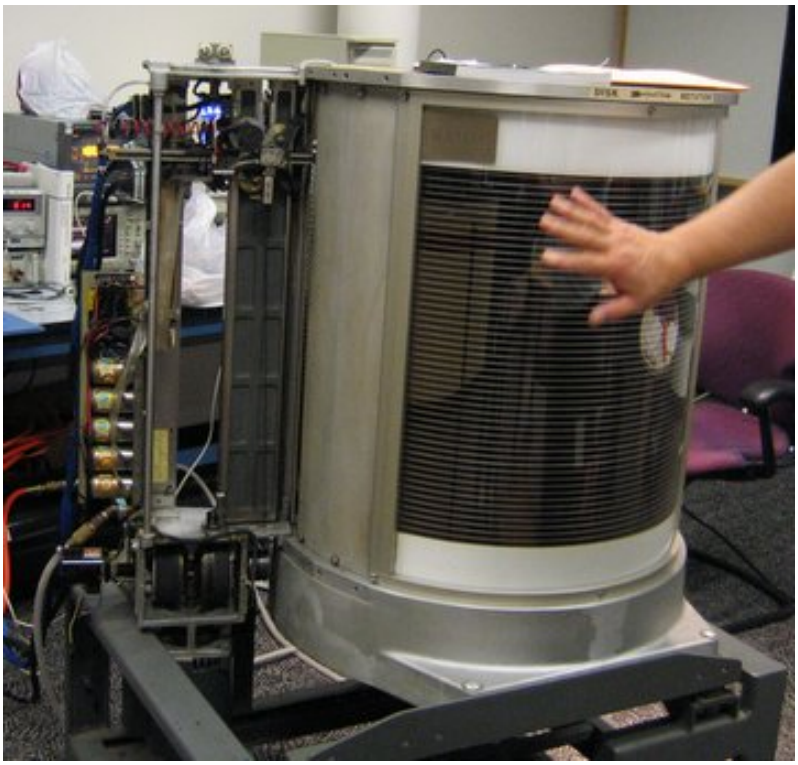

Figure 1.2: Random Access Memory Accounting Machine (RAMAC) (picture source [38])

The next generation of computer hard disk drives introduced by IBM was called the IBM 1301 Disk Storage. It was introduced in 1961 and had a storage capacity of $28MB$. 25 disks were used in the IBM 1301. An improved model of the IBM 1301 Disk Storage, the so-called IBM 1302 Disk Storage, was introduced in 1963. The storage capacity of the IBM 1302 was four times as high as the storage capacity of the IBM 1301. The IBM 1302 could read and write at the rate of $184,000$ characters per second [18, 36].

Initially, computer hard disk drive systems were expensive, large, and used

only by insurance companies, government agencies, or airline companies. The introduction of personal computers resulted in a higher demand for affordable, high-capacity, reliable hard disk drives. An entire industry evolved around the development and manufacturing of computer hard disk drives. The main parameter influencing the capacity of a computer hard disk drive is the areal storage density. This subject is introduced in the next section of this thesis.

1.2 Areal Storage Density

Magnetic recording has become the main technology for the storage of digital data. With the introduction of hard disk drives in consumer products such as video recorders or cell phones, the demand for high-performance, high capacity hard disk drives continues to increase at a rapid pace. The primary parameter influencing the storage capacity of a computer hard disk drive is the areal storage density. The driving force in research and development of computer hard disk drives is to increase the areal storage density.

The areal storage density is measured in bits per unit area of disk surface. Over the last 10 years, the areal storage density has been doubled every 12 to 18 months. The first computer hard disk drive, the so-called RAMAC, introduced by IBM in 1956, had an areal storage density of 2000 bits per square inch ($2000 b/in^2$). A current state-of-the-art computer hard disk drive has an areal storage density of

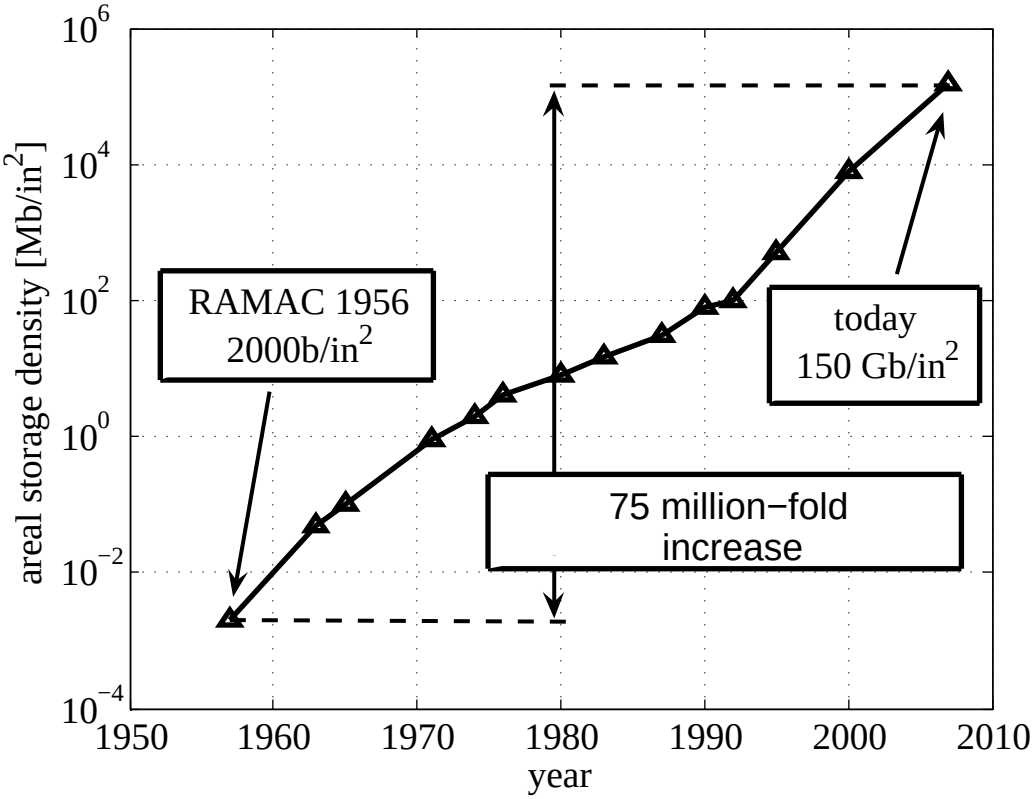

Figure 1.3: Development of areal storage density versus time

150 gigabit per square inch ($150 Gb/in^2$), representing a 75 million-fold increase in areal storage density, compared to the RAMAC. Figure 1.3 shows the areal storage density as a function of time for the past 50 years.

The areal storage density is the product of track density and linear density. The track density is measured in the number of tracks per unit length in the radial direction of the disk, while the linear density is measured in the number of bits per unit length in the circumferential direction. Increasing either the track density

or the linear density by a factor of two would directly result in doubling the areal storage density. The track density of the first computer hard disk drive was 20 tracks per inch ($20tpi$) and the linear density was 100 bits per inch ($100bpi$) [18]. The values for track and linear density in current computer hard disk drives are on the order or $140,000tpi$ for the track density and $830,000bpi$ for the linear density [13].

The growth in areal storage density is limited by a number of factors [51]. Of most concern are the super-paramagnetic effect [8, 11, 23, 31] and the signal-to-noise ratio (SNR) [5, 10, 26, 43, 44]. The super-paramagnetic effect is related to the thermal stability of magnetic domains. The increase in areal storage density has led to a decrease in the size of a single bit. Less energy is required to change the magnetization of a small bit compared to the energy required for a larger bit. For very small length scales, i.e., very small bits, the energy required for changing the magnetization of the bits becomes comparable with the thermal energy of the bit. At this point, the bit can randomly change its magnetization; thus, the stored magnetic information would be lost. Several researchers have estimated the areal storage density at which the super-paramagnetic limit is reached. Charap et al. [8] estimated a limiting storage areal density of $40Gb/in^2$. Weller and Moser [49] predicted an areal storage density of $100Gb/in^2$.

In general, an increase in areal storage density results in a reduced signal-to-

noise ratio (SNR) of the read-back signal. The decrease in signal-to-noise ratio is related to the granular character of the magnetic media. Each bit consists of several grains. A perfect bit would have a rectangular shape. In that case, the transition to adjacent bits would be infinitely sharp. However, since the grains are not perfectly shaped or aligned in the magnetic layer, the edges of each bit are rather "frayed." The shape of the bit edges results in transition noise. The noise increases as the bit size decreases, thereby putting an additional constraint on the achievable storage capacity of a hard disk drive. Mallary et al. [26] estimated that signal-to-noise ratio related problems would prevent a further growth in areal storage density at an areal storage density of $100 Gb/in^2$. Their work was based on the assumption of longitudinal recording technologies. Traditionally, longitudinal recording technologies have been used in computer hard disk drives.

Current and future approaches to further increase the areal storage density are perpendicular magnetic recording, heat assisted magnetic recording (HAMR), or patterned media technologies. Perpendicular magnetic recording is currently being introduced in commercially available computer hard disk drives. Heat assisted magnetic recording and patterned media technologies are still in development. Perpendicular magnetic recording, heat assisted magnetic recording, and patterned media recording technologies are outlined in the next section of this thesis.

1.3 Current and Future Technologies for Areal Storage Density Increase

The super-paramagnetic effect and signal-to-noise ratio are believed to constrain the growth in storage areal density of computer hard disk drives [51]. Alternative approaches are perpendicular magnetic recording, heat assisted magnetic recording (HAMR), and patterned media technologies. These technologies are introduced in this section of the thesis.

1.3.1 Perpendicular Magnetic Recording

Longitudinal magnetic recording has traditionally been used in the magnetic storage of digital data in computer hard disk drives. Perpendicular recording is currently being introduced in commercially available computer hard disk drive products. Figure 1.4 shows a schematic of longitudinal magnetic recording. As seen in Figure 1.4, the magnetic bits are oriented parallel to the disk surface. Figure 1.5 shows a schematic of perpendicular magnetic recording. In perpendicular magnetic recording the magnetization direction of bits is oriented perpendicular to the disk surface. As seen in Figure 1.5, an additional magnetically soft underlayer is needed in perpendicular recording compared to longitudinal recording. The magnetically soft underlayer can be considered a part of the write head [4].

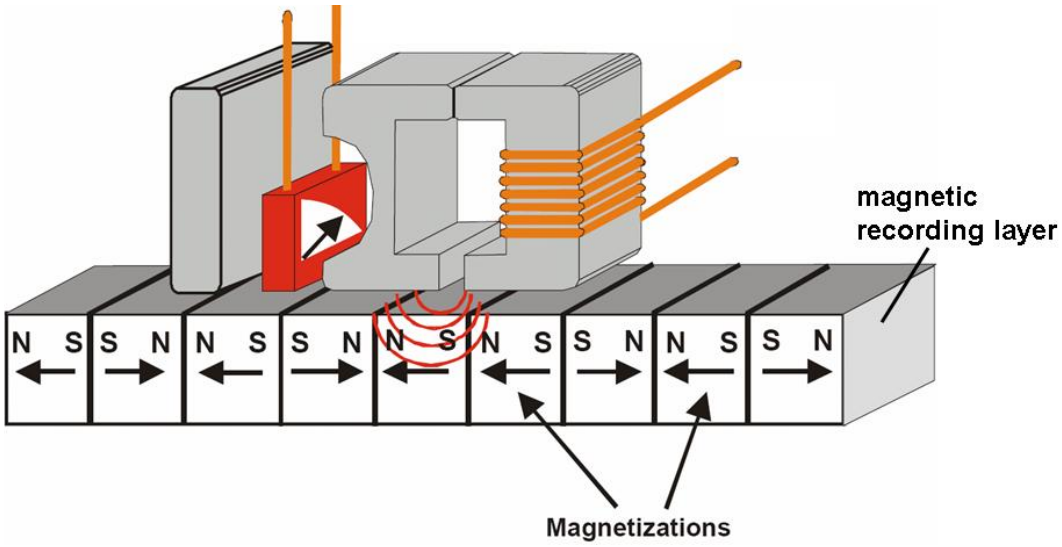

Figure 1.4: Schematic longitudinal magnetic recording (source [13])

The write head is used to write magnetic information on the magnetic medium. The use of a soft underlayer results in magnetic write fields with a strong field gradient [4, 5], as depicted in Figure 1.5. The thermal stability of a bit is proportional to the product of its volume and the coercivity of the magnetic material used. Coercivity is defined as the intensity of the applied magnetic field required to reduce the magnetization of the material to zero. Coercivity is related to the magnetization stability of the material. Magnetic materials with a high coercivity require strong write fields. An increase in the volume of a bit and an increase in the coercivity results in an increase in the thermal stability of a single bit.

Bertram et al. [5, 34] estimated the limiting areal storage density for perpendicular recording to be $500 Gb/in^2$, before signal-to-noise related problems would

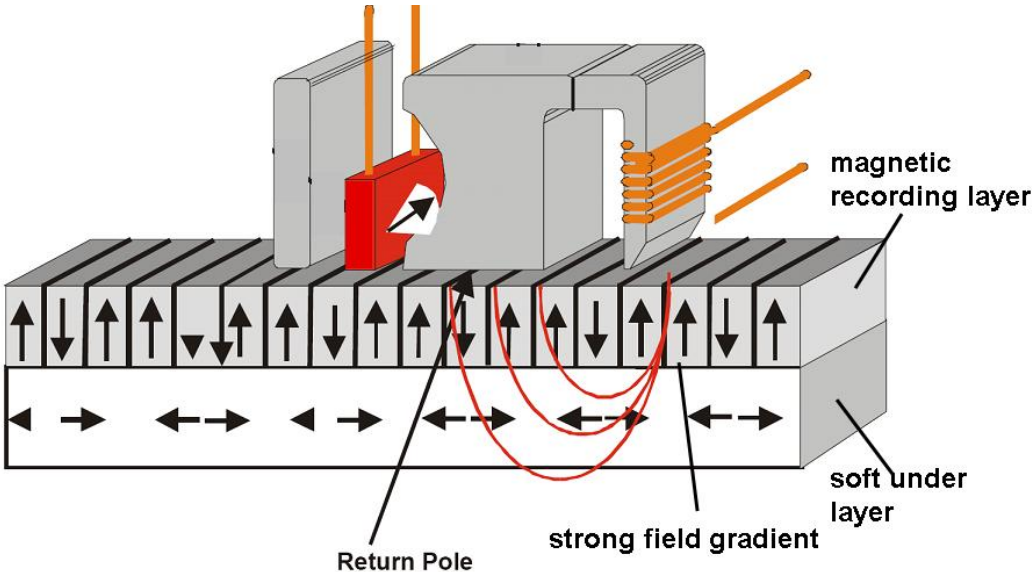

Figure 1.5: Schematic perpendicular magnetic recording (source [13])

become severe. Victora et al. [44] and Gao et al. [11] estimated storage areal densities of up to $1000 Gb/in^2$ to be achievable with perpendicular recording. It is believed that heat assisted magnetic recording (HAMR) and/or patterned media technologies must be used to further increase the areal storage densities in future computer hard disk drives.

1.3.2 Heat Assisted Magnetic Recording

Thermal stability or signal-to-noise ratio related problems will constrain the growth in areal storage density for perpendicular magnetic recording [5, 10, 11, 34, 44]. Heat assisted magnetic recording (HAMR) [14, 24, 34] is a promising approach

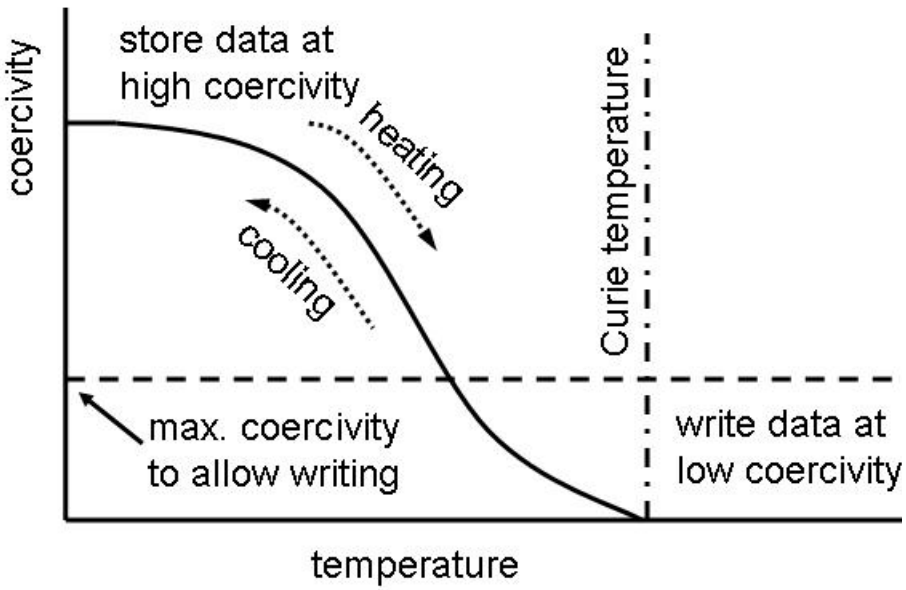

Figure 1.6: Schematic of write process in heat assisted magnetic recording (HAMR)

for increasing the storage capacity of future computer hard disk drives.

In this approach, a magnetic material with very high coercivity is used, resulting in an increase in the magnetic energy of a single bit. Since the write field strength of present day magnetic heads is not strong enough to write on very high coercivity materials, a bit to be written is heated up prior to writing to a temperature above the Curie temperature; during cooling, the magnetization is changed, when the coercivity is still low.

The change of coercivity with temperature is depicted in Figure 1.6. As seen in the figure, the coercivity decreases with increasing temperature. The temperature at which the coercivity of the material approaches zero is called the Curie temper-

ature. The write process in heat assisted magnetic recording can be described as follows:

1. The bit cell is heated above its Curie temperature.

2. During cooling, when the temperature is slightly below the Curie temperature, the magnetic write field aligns the bit in the desired direction.

3. While the magnetic write field is applied, the material cools down, leaving the desired magnetization "frozen" in the bit cell.

In Figure 1.7 a schematic of heat assisted magnetic recording is shown. As can be seen, laser light is used to heat the magnetic material locally, prior to writing. Temperatures on the order of several hundred degrees Centigrade are likely to be required in heat assisted magnetic recording [54].

In heat assisted magnetic recording, the thermal stability of the stored information is improved using a high coercivity magnetic material. In patterned media storage technologies the stability of the stored information is achieved by eliminating transition noise partially or entirely. Patterned media technologies are discussed in the next section of this thesis.

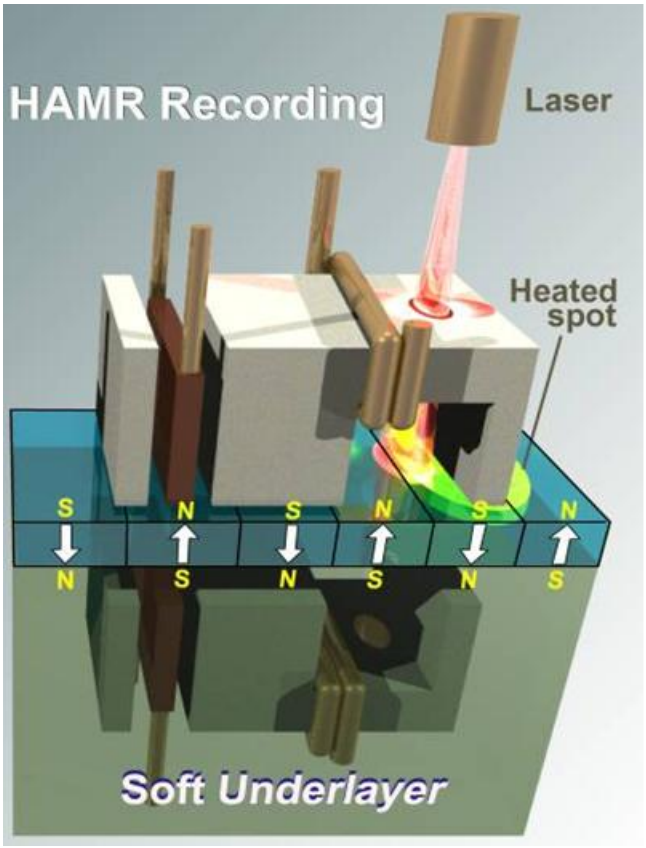

Figure 1.7: Schematic of heat assisted magnetic recording (HAMR) (source [37])

1.3.3 Patterned Media Technologies

Another promising approach towards achieving ultra high densities in excess of $500 Gb/in^2$ [5, 10, 11, 34] is to partially or completely isolate each magnetic bit from its neighboring bits, thereby reducing cross talk and transition noise between adjacent bits [24, 51]. This so-called "patterned media" approach can be implemented in the form of discrete track recording (DTR) or bit patterned media

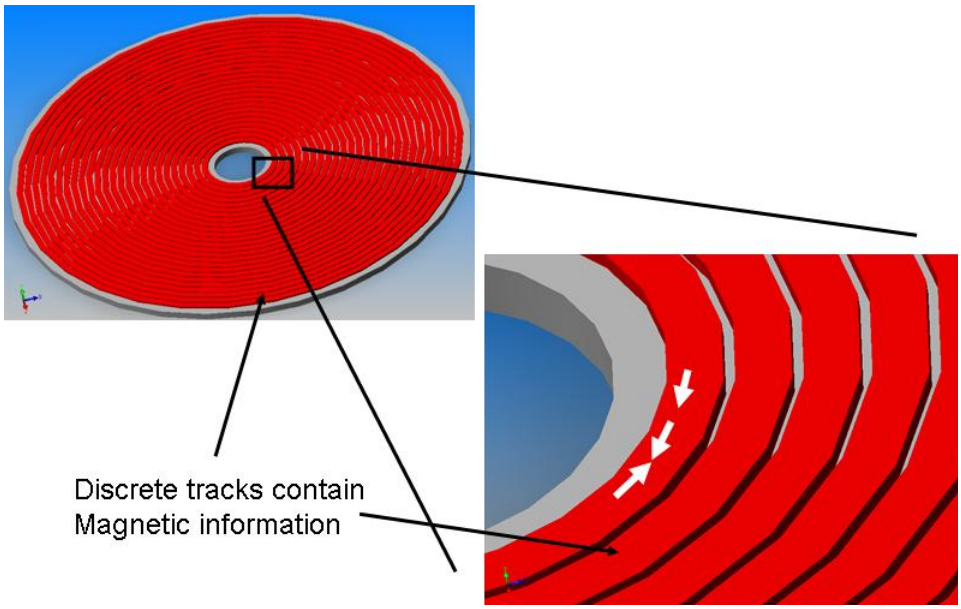

Figure 1.8: Schematic of discrete track recording (DTR)

(BPM) recording. In Figure 1.8, a schematic of the disk surface for discrete track disks is shown, and in Figure 1.9, a bit patterned media disk is depicted.

In discrete track recording (Figure 1.8), the magnetic information is stored along circumferential tracks. The tracks are physically separated from each other, resulting in an elimination of transition noise in the radial direction of the disk. Transition noise is still present in the circumferential direction of the disk [41]. An increased signal-to-noise ratio and a better write efficiency has been reported for discrete track recording [40, 45], supporting the idea of discrete track recording as a technology for future high areal density hard disk drives. So far, areal storage densities of up to $200 Gb/in^2$ have been reported for discrete track recording [45].

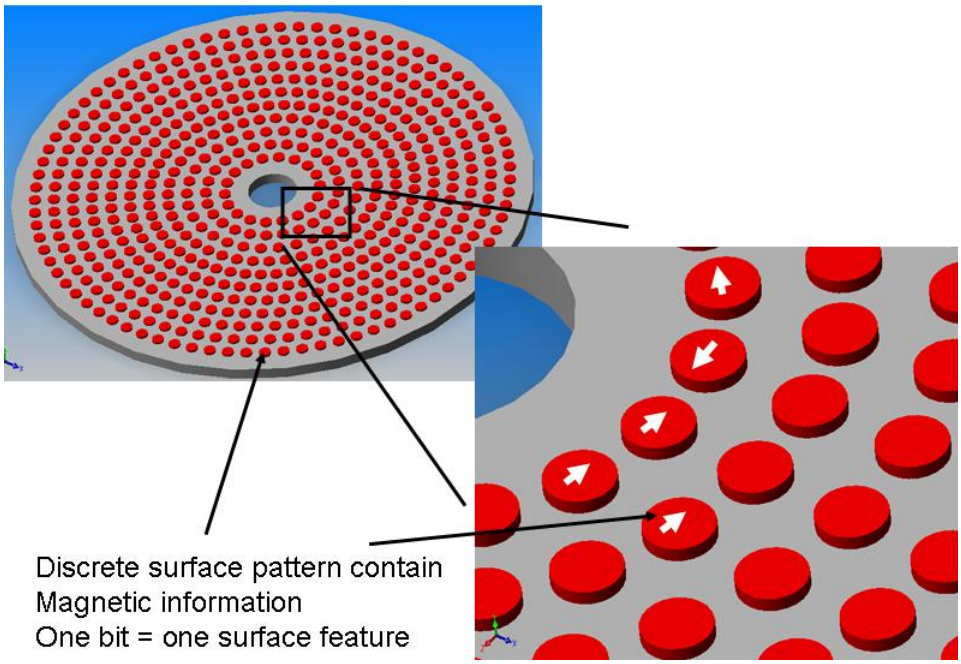

Figure 1.9: Schematic of bit patterned media (BPM)

The width of the tracks at such a density were reported to be $63nm$. The tracks were separated by a distance of $63nm$.

In bit patterned media recording the information is stored in single "pillar-like" structures on the disk surface (Figure 1.9). The bits are physically separated from each other, resulting in elimination of transition noise in the radial and the circumferential direction of the disk. At a storage density of $1000Gbit/in^2$ ($1Tb/in^2$, one terrabit, $1Tb = 1000Gb$), each bit would be stored in a pillar with a diameter of approximately $12nm$. The bits would be separated by a distance of $12nm$. Richter et al. [33] showed that bit patterned media technologies allow an increase in areal

storage density of up to $5Tb/in^2$, thereby increasing the capacity of today's hard disk drives more than thirtyfold.

While patterned media technologies seem to be a promising approach for areal storage densities beyond $500Gb/in^2$, cost efficient manufacturing technologies for patterned media disk have yet to be developed. Without a cost efficient way of producing patterned media disks, it seems unlikely that patterned media technologies will be implemented.

The main technologies of current computer hard disk drives have been introduced as well as potential future technologies. The basic principles of writing and reading magnetic information are explained in the following part of this thesis.

1.4 Principles of Magnetic Recording

The basic principles of writing and reading magnetic information are introduced in this section. A short description of the evolution of magnetic read/write heads is given.

1.4.1 Magnetic Hysteresis

Magnetic recording is based on the theories of magnetism and electromagnetism. The relationship between the magnetic field and the external field strength

is

$$M = \mu_0 H + J \tag{1.1}$$

where, M is the flux density, H is the field strength, μ_0 is the permeability of the material, and J is the spontaneous magnetization of the material. In air, J is equal to zero ($J = 0$) [7].

The most fundamental requirement of a digital storage device is the existence of at least two stable states. Magnetic domains in a magnetic material have a well defined magnetization direction. An external field can be used to change the orientation of the magnetization.

The underlying principle of magnetic recording is the phenomenon of magnetic hysteresis. Figure 1.10 shows a magnetic hysteresis curve. An explanation of the hysteresis curve is important for the understanding of the fundamental binary storage principle in magnetic recording.

Prior to any writing the magnetic material does not hold any field. This stage corresponds to point a in Figure 1.10. When an increasing external magnetic field H is applied to the material, the magnetization M increases until saturation is reached (point b). At the saturation no further increase in the material magnetization is possible, even if the external field is increased beyond point b. If the external field is reduced to zero, the magnetization of the material reaches point c. This point is called the remanent magnetization $+M_r$. If the external field becomes

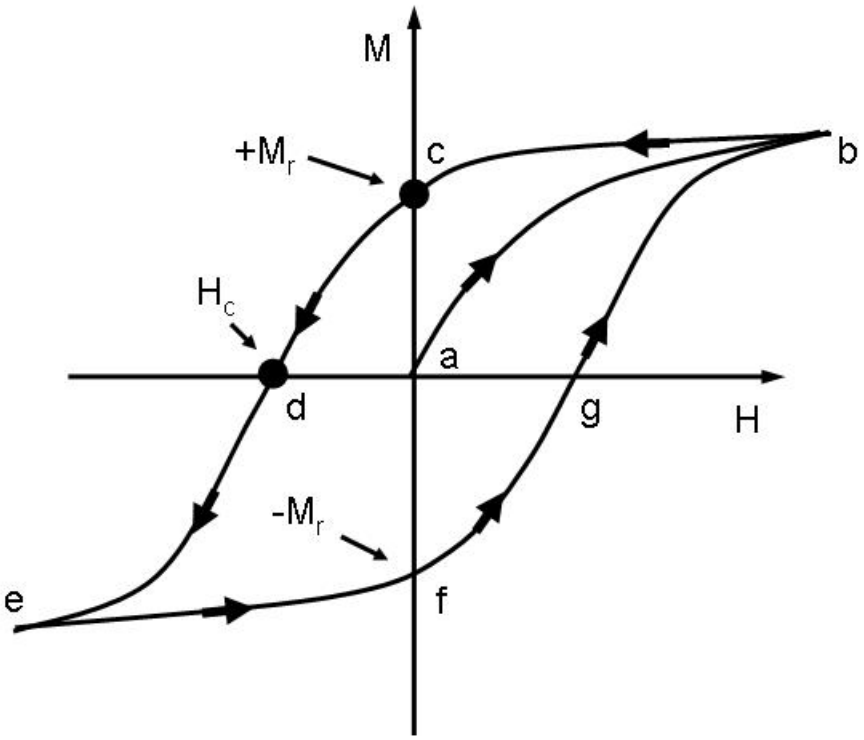

Figure 1.10: Magnetic hysteresis curve

negative, the magnetization becomes zero (point d). The external field necessary to achieve zero magnetization is called the coercivity of the material H_c. By further reducing the field, a negative saturation state is reached (point e). Increasing the field to zero results in a negative remanent magnetization $-M_r$ of the material (point f). The two states of remanent magnetization $+M_r$ and $-M_r$ represent the two stable states needed for a binary storage application. In magnetic recording, a material has to be chosen with a coercivity H_c large enough to assure thermal stability and small enough so that the state of magnetization can be changed by

the magnetic field of the write element.

In the next section of the thesis a short description of the evolution in the design of magnetic read/write heads is given.

1.4.2 Evolution of Magnetic Read/Write Heads

Magnetic read/write heads have been continually developed and improved, with the goal of increasing the storage capacity of disk drives. Before giving an introduction to the write and read processes in magnetic recording, an outline of the read/write head evolution is given. In Figure 1.11 the evolution of magnetic read/write heads [13] is shown.

Initially, inductive read/write heads with machined pole pieces and wire wound coils were used. The same transducer (head) was used for writing and reading of the magnetic information. With improvements in photolithography technologies pioneered by the semiconductor industry, inductive thin film heads were introduced in 1980. Compared to machined inductive heads, the pole and coil geometries were controlled by photolithographic processes. Additionally, the use of manufacturing processes, similar to semiconductor fabrication, allowed batch production of magnetic read/write heads. Batch production led to a decrease in manufacturing costs. At the beginning of the 1990's, magnetoresistive (MR) read heads were introduced, thereby separating the read-back process from the inductive coil. Magnetoresistive

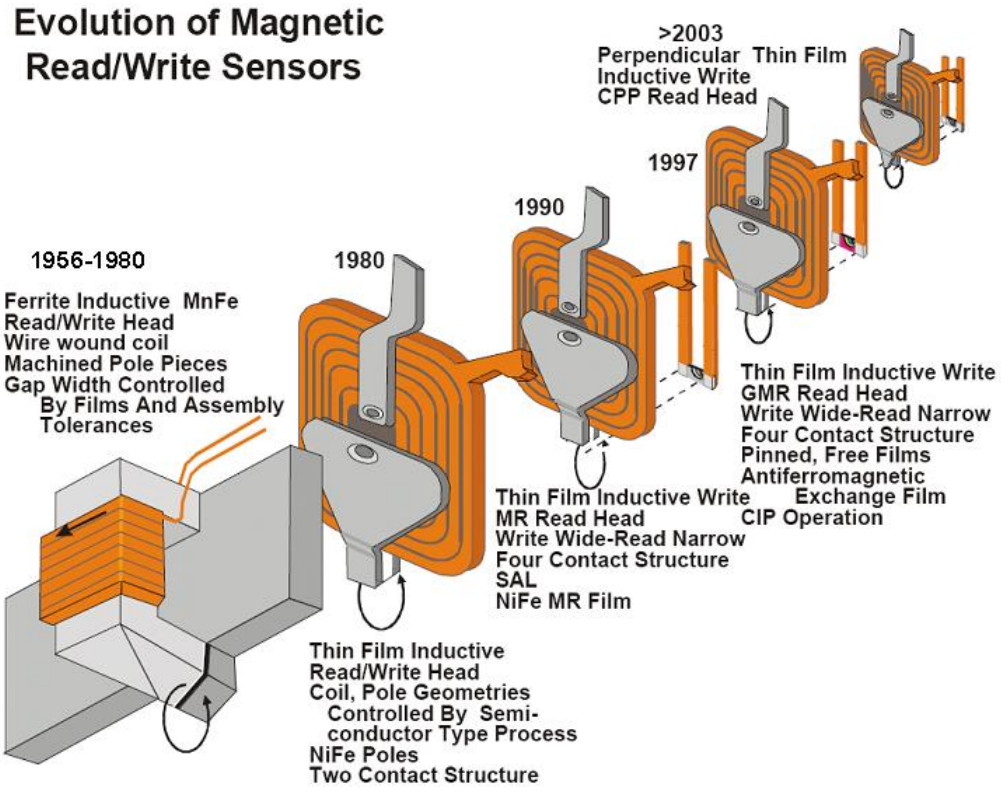

Figure 1.11: Evolution of magnetic read/write heads (source [13])

heads are based on the phenomenon of magnetoresistivity [15]. Upon the discovery of the giant-magnetoresistivity [1], giant-magnetoresistive (GMR) read elements were introduced in 1997. With the current development of perpendicular magnetic recording, tunnel magnetoresistive read elements are being introduced [20, 29, 28].

The writing process and available read-back sensors are described next.

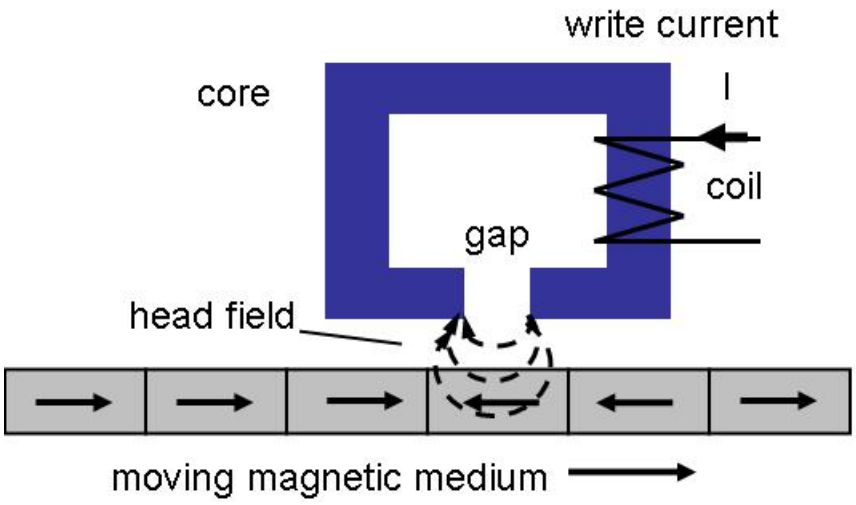

Figure 1.12: Schematic of magnetic write process

1.4.3 Write Process

In digital magnetic recording the information is stored in small domains, the magnetic bits. To write a bit on a magnetic medium an external magnetic field is needed. The magnetic field is created by an inductive write head. Figure 1.12 shows a schematic of the write process for longitudinal recording using an inductive write head. The magnetic field is produced by a current carrying coil, as shown in Figure 1.12. The current through the coil generates a magnetic field at the gap. The fringing field at the pole tips passes through the medium, thereby aligning the magnetization of a bit. Depending on the direction of the current, two distinct magnetization directions can be written on the disk.

1.4.4 Read-back Process

Inductive Read Heads

Inductive read heads were used in early computer hard disk drives. Figure 1.13 shows a schematic of a typical inductive read back element. It consists of a core and an induction coil. The change in the fringing field of the medium causes a

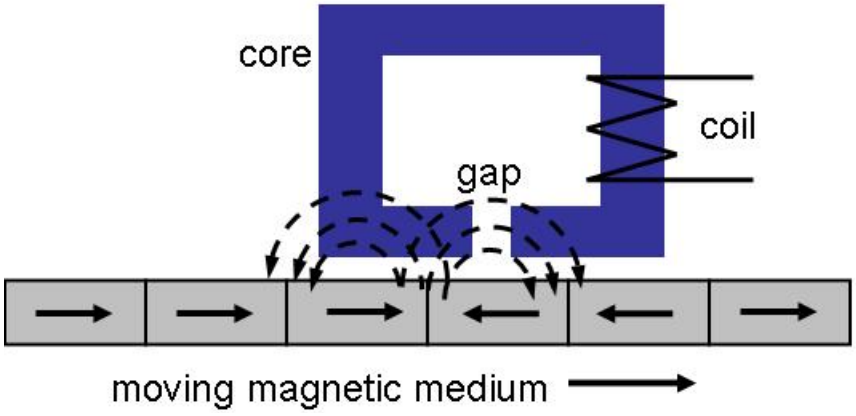

Figure 1.13: Schematic of inductive read back process

voltage change across the coil. The voltage V induced in the coil is based on Faraday's law for induction,

$$V = -N\frac{d\Phi}{dt}, \tag{1.2}$$

where N is the number of turns in the coil and Φ is the magnetic flux. Since the disk is rotating, the term $d\Phi/dt$ can be written as

$$\frac{d\Phi}{dt} = \frac{d\Phi}{dx}\frac{dx}{dt} = v\frac{d\Phi}{dx}, \tag{1.3}$$

where v is the velocity of the moving magnetic medium. Combining equations 1.2 and 1.3 results in

$$V = -Nv\frac{d\Phi}{dx}. \tag{1.4}$$

From equation 1.4, it is apparent that the induced voltage is proportional to the number of turns in the coil N, the velocity v, and the change of flux, $d\Phi/dx$, along the track.

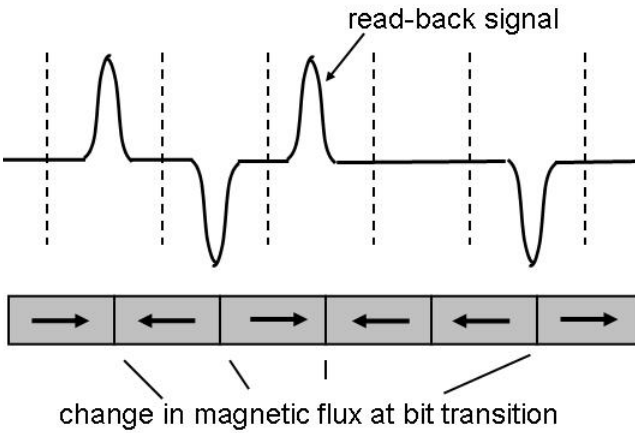

Figure 1.14: Schematic of read-back signal for a given magnetization pattern

Figure 1.14 illustrates the read-back signal as a function of a given magnetization pattern on the magnetic layer. A voltage pulse is observed in the read head for every change in magnetic flux along the track.

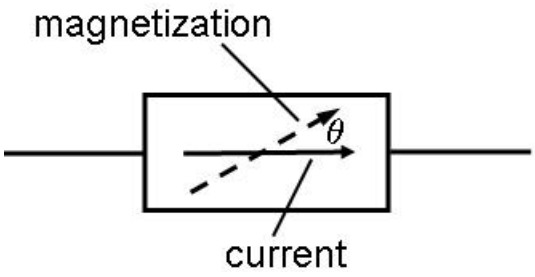

Figure 1.15: Anisotropic magnetoresistance of a ferromagnetic material

Magnetoresistive Read Heads

Magnetoresistive (MR) heads are based on the effect of magnetoresistance [15]. Magnetoresistance is the property of ferromagnetic materials to change their electrical resistance with a change in the external magnetic field applied. In magnetoresistive read heads, the fringe field from the media is used to change the resistance of the read head.

The anisotropic magnetoresistance of a material is characterized by the resistance parallel ($\rho_{\parallel}$) and perpendicular ($\rho_{\perp}$) to the magnetization [4]. If Θ is the angle between the direction of the sense current and the direction of the magnetization of a stripe of ferromagnetic material (Figure 1.15), the resistance can be written as

$$\rho = \rho_{\perp} + (\rho_{\parallel} - \rho_{\perp}) \cos^2 \Theta, \tag{1.5}$$

where ρ is the resistivity. The term $(\rho_{\parallel} - \rho_{\perp})$ represents the anisotropic magne-

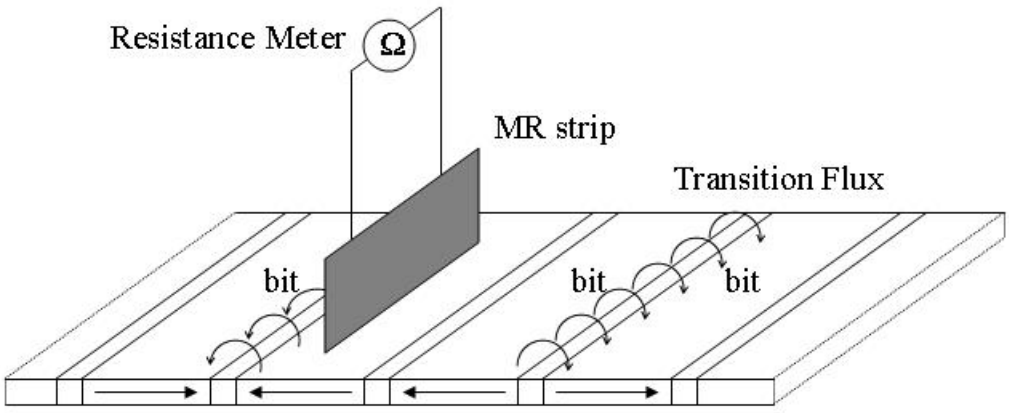

Figure 1.16: Schematic of read-back process using a magnetoresistive head

toresistive effect. Figure 1.16 shows a schematic of the read-back process using a magnetoresistive head. The change in magnetization at the transition of two bits results in a change of resistance of the magnetoresistive element. The change of resistance is used as the read-back signal. Unlike in inductive read heads, the magnitude of the read-back signal does not depend on the speed of the disk [15, 39]. The magnetoresistive element is a thin film structure and can be implemented using photolithographic batch manufacturing processes of modern thin film heads.

Giant Magnetoresistive Read Heads and Tunnel Magnetoresistive Read Heads

Arrays of alternating thin ferromagnetic and nonmagnetic metal layers exhibit large changes in resistance when the direction of magnetization is changed by an ex-

ternal magnetic field. Such multilayered structures are called super-lattices. Since the observed resistance changes are large, the effect is called giant magnetoresistive (GMR) effect [1].

The maximum change in resistivity due to the magnetoresistive effect is on the order of 4% [25]. The change in resistivity based on the GMR effect can be as large as 50% [25], which is a significant gain compared to MR heads and results in a higher signal-to-noise ratio. Due to the higher sensitivity, GMR heads have replaced MR heads in modern computer hard drives.

The tunnel magnetoresistive (TMR) effect occurs when two ferromagnetic layers are separated by a thin insulator (on the order of $1nm$). The resistance of the tunneling current changes with the relative orientation of the two magnetic layers. The tunnel magnetoresistive effect was first discovered by Julliere [20] using iron as the ferromagnet and germanium as the insulator. Tunneling magnetoresistance at room temperature was first reported by Moodera et al. [29, 28].

The read-back process for GMR and TMR heads is similar to the read process used for MR heads (Figure 1.16). The change in resistance measured at each magnetic flux change at bit transitions is used as the read-back signal.

1.4.5 Magnetic Spacing

The distance between the bottom surface of the read-back element and the top surface of the magnetic layer, referred to as magnetic spacing or head-medium spacing (HMS), is a key parameter of the read and write process in magnetic recording. The strength of the magnetic field created by the write element decreases with increasing distance and becomes too weak to record any data. The field from the magnetic domains (bits) in the medium also decreases with increasing distance. If the distance becomes large, a decreased magnetic flux in the read-back sensor occurs during the read-back process which can lead to errors in the read-back signal.

Wallace [46] determined the read-back signal strength S to be

$$S(d) = e^{-2\pi d/\lambda}, \tag{1.6}$$

where S is the signal strength, d is the distance, and λ the wave length. As can be seen from equation 1.6, the signal strength decays exponentially with increasing head-medium spacing. It is of great importance to decrease the head-medium spacing. One of the key parameters for the increase of areal storage density in computer hard disk drives is the reduction of the head-medium spacing.

In order to obtain a well defined read-back signal with high amplitude and small pulse width, it is necessary to change the magnetization between adjacent bits in as short a distance as possible. In the ideal case, a perfectly sharp transition

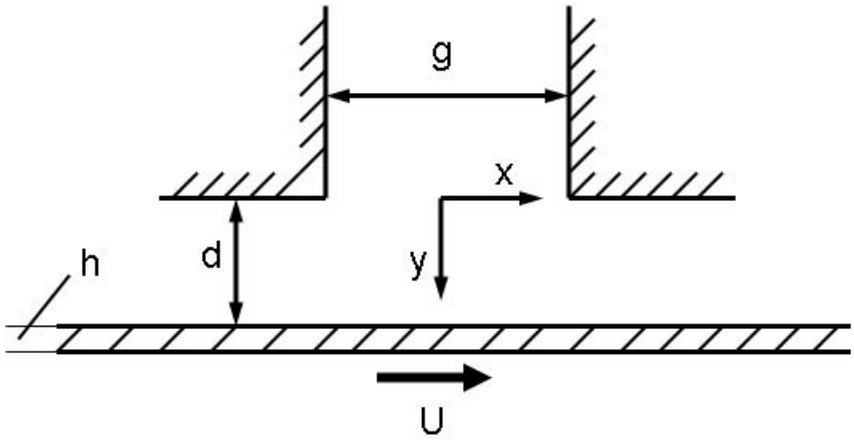

Figure 1.17: Definition of symbols for read-back signal analysis

is generated by a "step-like" magnetization change. Such an ideal step can be expressed as

$$\frac{dM_x}{dx} = 2M_r\delta(x - x_o), \tag{1.7}$$

where M_x is the magnetization in the x-direction (see Figure 1.17), M_r represents the remanent magnetization, and δ is the Dirac delta function defined by

$$\delta(x) = 0 \text{ everywhere except at } x = 0, \tag{1.8}$$

and

$$\int_{-\infty}^{\infty} \delta(x)dx = 1. \tag{1.9}$$

The output voltage of an inductive read head can be calculated using the

reciprocity integral [4, 25, 27]

$$V_x(\bar{x}) = -\mu_0 U N_r w \int_{-\infty}^{\infty} \int_{d}^{d+h} \frac{dM_x(x-\bar{x})}{dx} H_x(x,y) dx dy, \tag{1.10}$$

where μ_0 is the permeability of free space, U is the velocity of the medium, w is the track width, $\bar{x}$ is defined as $\bar{x} = Ut$ (t is time); N_r is the number of turns in the read head; d is the distance between the medium and the head; h is the magnetic film thickness, and H_x is the magnetic field strength from the head in the x-direction.

After substituting equation 1.7 into the reciprocity integral, equation 1.10 can be written as

$$V_x(\bar{x}) = -\mu_0 U N_r w \int_{d}^{d+h} dy' \int_{-\infty}^{\infty} 2M_r \delta(x-\bar{x}) H_x(x,y) dx. \tag{1.11}$$

Evaluating the integral yields

$$V_x(\bar{x}) = -\mu_0 U N_r w \delta(2) M_r H_x(\bar{x}, d + \frac{1}{2}h). \tag{1.12}$$

The voltage response from an ideally sharp magnetic transition is directly proportional to the horizontal component of the head field itself.

The ideally sharp transition is a theoretical case. Many of the features of the read process can be demonstrated assuming a sinusoidal magnetization of the medium

$$M_x(x) = M_0 \sin kx, \tag{1.13}$$

where M_0 is the magnetization amplitude, k is the wave number given by

$$k = \frac{2\pi}{\lambda}, \tag{1.14}$$

and λ is the wavelength of the sinusoidal magnetization. It was shown by Wallace [46], that the output voltage for sine wave recording can be written as

$$V(\bar{x}) = -\mu_0 U N_r w M_0 \frac{H_g}{g} \left[e^{-kd}\right] \left[1 - e^{-kh}\right] \left[\frac{\sin kg/2}{kg/2}\right] \cos k\bar{x}, \tag{1.15}$$

where H_g is the gap field and g is the gap width of the read-back head. The terms in brackets are the so-called loss terms [25, 27]. The first term

$$L_{spacing} = \left[e^{-kd}\right] \tag{1.16}$$

is the spacing loss and shows that the output voltage falls exponentially with the product of wave number k and head-media spacing d [46]. The term

$$L_{thickness} = \left[1 - e^{-kh}\right] \tag{1.17}$$

represents the loss due to the medium thickness. As can be seen from equation 1.17 the use of thin media minimizes the thickness loss. The third term

$$L_{gap} = \left[\frac{\sin kg/2}{kg/2}\right] \tag{1.18}$$

is called the gap loss. The gap loss becomes zero for $\sin kg/2 = 0$. From equation 1.14 it is apparent that this case occurs when the wave length of the magnetization λ is a multiple of the gap width g ($\lambda = ng$ with $n = 1, 2, 3, \cdots$).

1.5 Mechanical Components of a Disk Drive

In this section the major mechanical components of a computer hard disk drive are introduced. Figure 1.18 shows a photograph of a disk drive with the major mechanical components annotated. A typical disk drive consists of one or more hard disks mounted on a hub driven by a spindle motor. A slider is mounted on a suspension. The slider carries the magnetic read/write head. The suspension is attached to an actuator arm which is controlled by a voice coil motor.

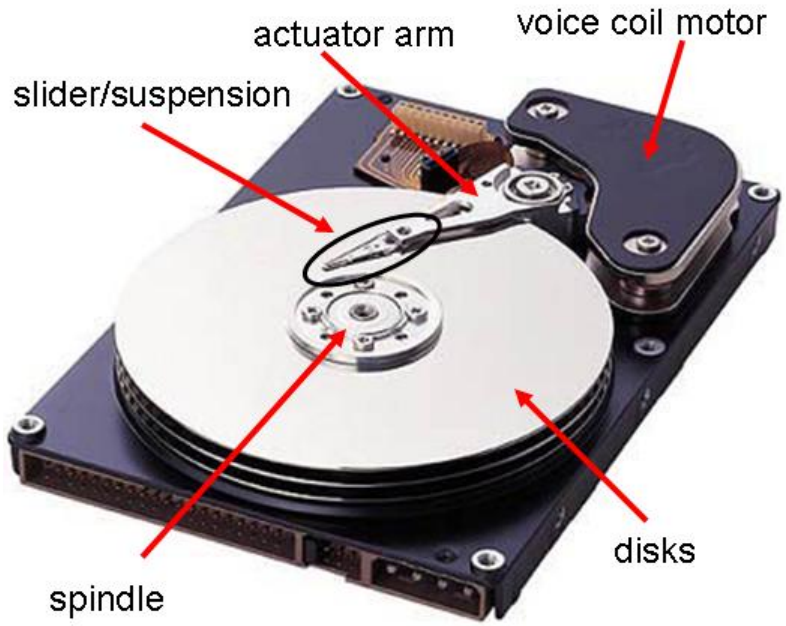

Figure 1.18: Photograph of a modern hard disk drive, with major components annotated (source: [37])

The rotary actuator arm allows radial positioning of the slider over the disk surface (Figure 1.19). The radial positioning of the slider using a rotary actuator

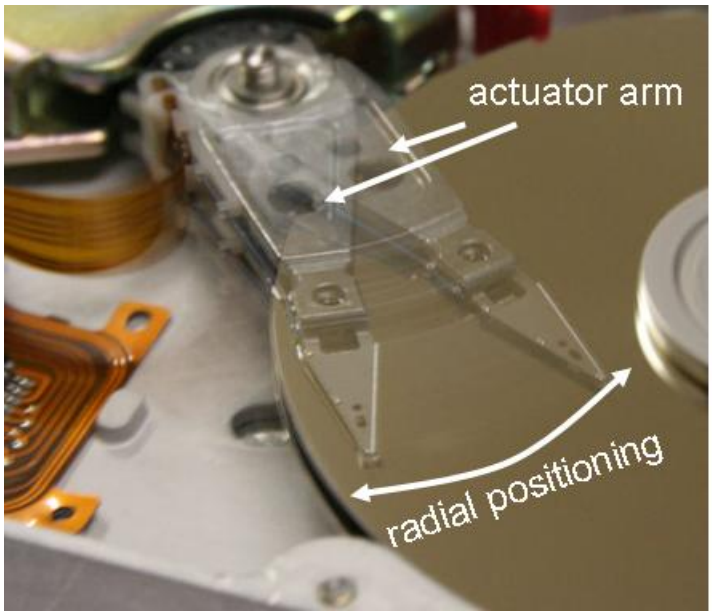

Figure 1.19: Radial positioning of slider over disk surface by voice coil motor driven actuator arm (source: [37])

arm provides one of the most important features of a hard disk drive: fast random access to the stored data.

1.5.1 Air Bearing Sliders

The air bearing slider carries the magnetic read and write element. During operation the slider is supported by an air bearing, which is generated as a result of the viscous flow between the rotating disk and the air bearing surface of the slider. The minimum thickness of the air bearing is referred to as flying height. A constant flying height of the slider for the different working conditions of the hard disk drive is essential for the drive's performance and reliability. The flying height

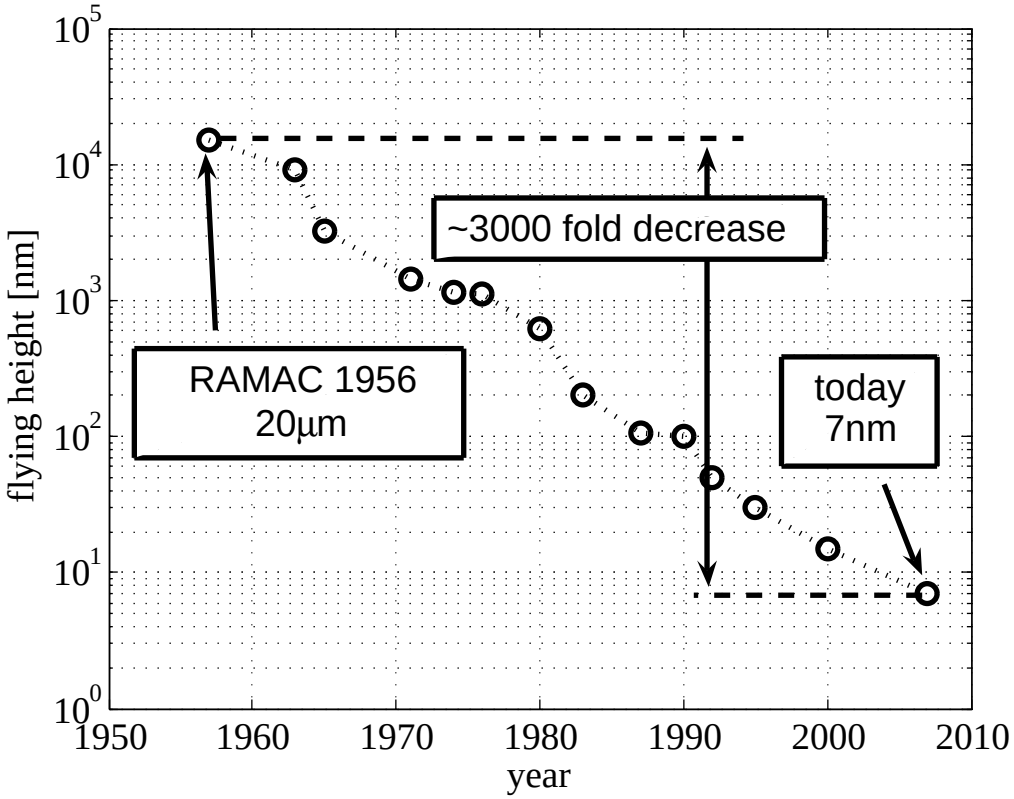

Figure 1.20: Development of flying height versus time

is part of the magnetic spacing described in section 1.4.5 of this thesis. Reducing the flying height results in a decrease of the magnetic spacing. The magnetic spacing influences the reading and writing of magnetic information. Hence, the flying height of the slider is a key parameter in increasing the areal storage density of future computer hard disk drives. Figure 1.20 shows the flying height as a function of time from the first hard disk drives until today. As seen in Figure 1.20, the flying height of sliders used in the first computer hard drive (RAMAC) was on

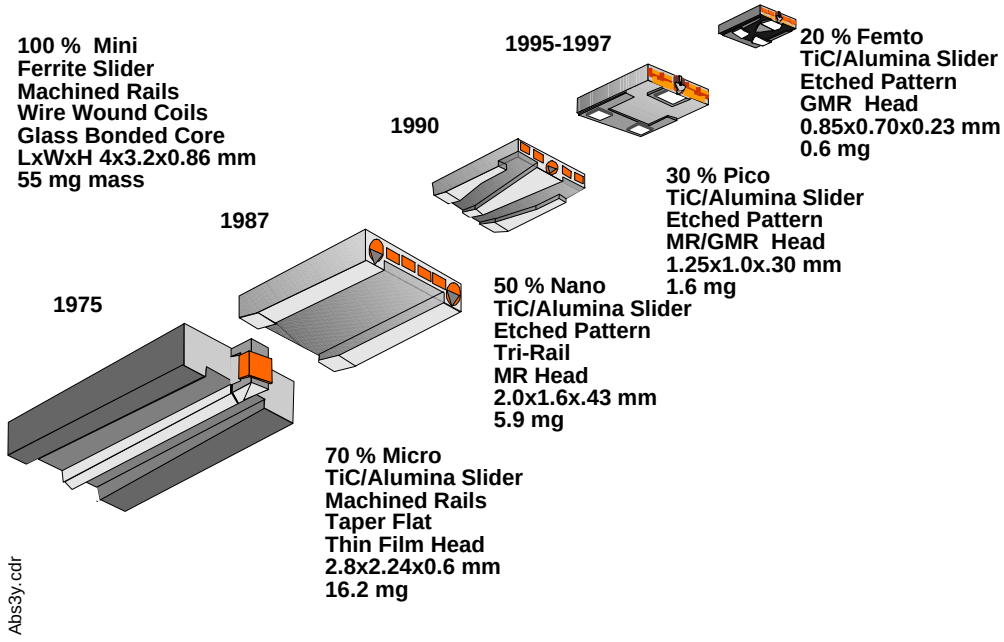

Figure 1.21: Evolution of air bearing slider design (source: [13])

the order of $20\mu m$. The flying height in current hard disk drives is on the order of $7nm$, i.e., the flying height has decreased by roughly 3000 times.

The reduction of the flying height is due to advancements in the air bearing design. Figure 1.21 shows the evolution of self acting air bearing designs starting from 1975 until today. Three main developments in the evolution process of sliders should be noted. First, the size of sliders has decreased with time. Secondly, the design of the air bearing surface has become more complex. Third, the load on the slider has decreased. The size of a slider is sometimes referred to as the form factor. Prior to self acting air bearing sliders, externally pressurized sliders have

been used.

The first slider shown in Figure 1.21 is the so-called three rail slider. This slider design featured three machined ferrite rails over the full length of the slider. The air bearing was formed underneath the two outside rails. The narrow center rail was used to support the read/write element. The width of the center trail was on the order of the track width. Since the track width was much smaller than the width of the side rails, the center rail did not contribute much to the load carrying capacity of the air bearing. This slider is described as a "mini" form factor slider design. The dimensions of the mini slider were $4mm$, $3.2mm$, and $0.86mm$ for the length, the width and the height, respectively. The magnetic head was mounted at the trailing edge center of the slider. As seen in Figure 1.21, a wire-wound coil was used for reading and writing for this slider design.

The next slider design shown in Figure 1.21 is a so-called two rail slider. The two rail slider consisted of two machined rails. The taper at the front of the flat rails pressurized the air along the length direction of the slider towards the trailing edge. This slider is a so-called "micro" form factor slider. Micro form factor sliders are sometimes referred to as 70% sliders, since their dimensions are 70% of the dimensions of mini sliders, i.e., $2.8mm$, $2.24mm$, and $0.6mm$ for the length, the width and the height, respectively. The magnetic read/write element was attached at the trailing edge of one of the rails, typically the outer trail. Placing the magnetic

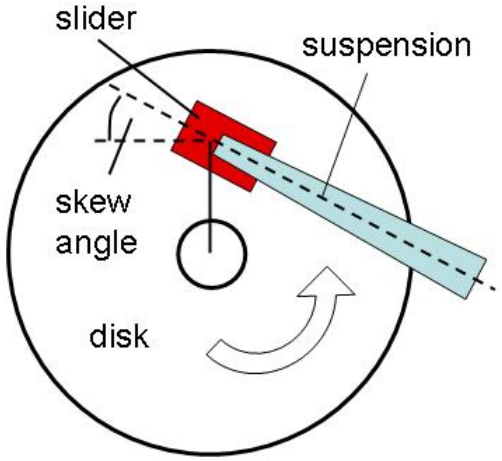

Figure 1.22: Definition of skew angle

read/write element on an outside rail caused problems with flying height stability and roll due to transverse air flow. Transverse air flow occurs in the case of a non-zero skew angle. The definition of the skew angle is shown in Figure 1.22. The two rail slider design was improved by introducing full length tapers or steps along the sides of the rails. The tapers and steps served as converging channels for the transverse flow component and allowed maintaining a more uniform pressure distribution. This modified two rail slider design was called the transverse pressure contour slider.

The next slider design shown in Figure 1.21 is the so-called nano slider design, or 50% slider design. The dimensions of the 50% slider are $2.0mm$, $1.6mm$, and $0.43mm$ for the length, the width and the height, respectively. This slider utilizes a

three rail air bearing design. The tri-rail design allowed the placing of the magnetic read/write head at the center of the trailing edge, thereby minimizing roll effects due to transverse flow. As time progressed, the center rail was reduced to a small center pad located at the trailing edge of the slider. This slider design was called a tri-pad slider.

The last two sliders depicted in Figure 1.21 are the pico and femto form factor sliders. The dimensions of the pico or 30% slider are $1.25mm$, $1.0mm$, and $0.3mm$, for the length, the width, and the height, respectively. The dimensions of the femto or 20% slider are $0.85mm$, $0.7mm$, and $0.23mm$, for the length, the width, and the height of the slider, respectively. The air bearing design of the pico and femto form factor sliders in Figure 1.21 are sub-ambient pressure slider designs, introduced in the early 1990's [9, 47].

Air bearing designs prior to the introduction of sub-ambient pressure sliders were called positive pressure sliders, since all of the air bearings had a pressure distribution larger than ambient over the complete air bearing surface. Positive pressure air bearing designs were sensitive to changes in the disk velocity. An increase in the velocity at the outside of a disk leads to an increased flying height of the slider compared to the inside. To maintain a constant spacing between the slider and the disk independent of the position of the slider over the disk, sub-ambient air bearing designs were developed (Figure 1.23).

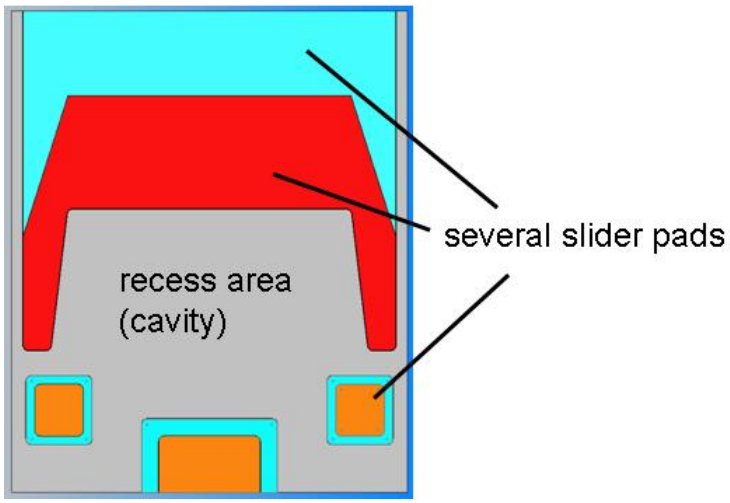

Figure 1.23: Schematic of sub-ambient air bearing slider design

The feature common to all sub-ambient air bearings is the existence of a recessed area, the so-called cavity. The cavity is a reverse step in the bearing were the air can suddenly expand leading to sub-ambient pressure in the cavity. A sub-ambient pressure in the cavity reduces the total load on the air bearing generated by the positive pressure areas. This allows the design of sliders with constant flying height on the inside and outside of a disk. All sub-ambient sliders have surface features or patches that create positive pressure to compensate for the sub-ambient pressure produced by the cavity. Different slider surface patches often have different height levels. In today's hard disk drives, sub-ambient pressure sliders are used exclusively. The air bearing surface in each of them is carefully designed to maintain an ultra-low but constant flying height independent of disk position and

ambient pressure.

Initially machined air bearing surfaces were used. With advances in the manufacturing of semi-conductors, photolithography and etching techniques were introduced in slider manufacturing. In today's computer hard disk drives only pico or femto form factor sliders are used. The material used to create a slider is alumina titanium carbide. The main reasons for the usage of small form factors are the shrinking size of computer hard disk drives and lower manufacturing costs. Wafer and batch processing are used for the manufacturing of today's sliders. If the slider size decreases, more sliders can be produced on a single wafer; thus, production costs decrease.

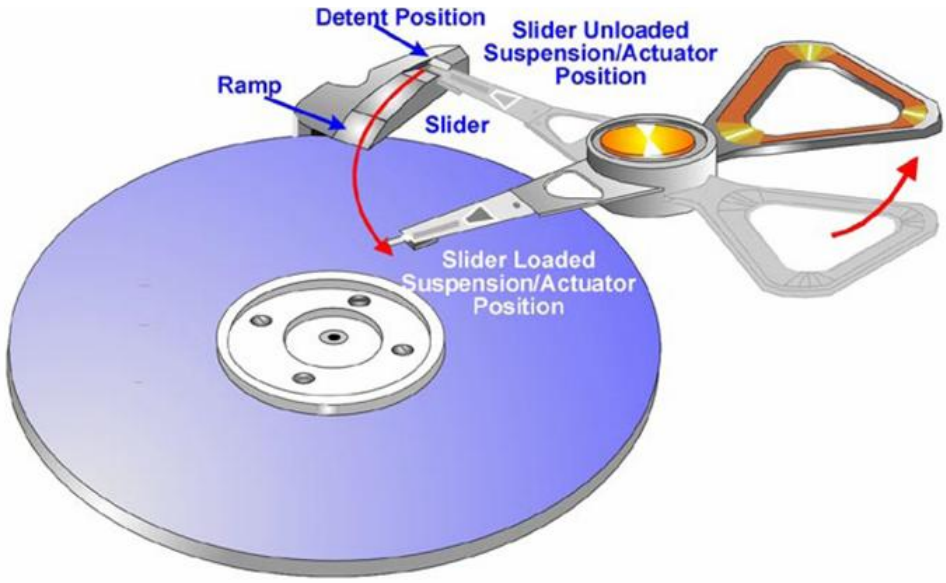

Figure 1.24: Schematic of load/unload mechanism (source: [13, 42])

In prior years, the slider was started and stopped on the inner diameter of a disk. This technology was called "contact-start-stop". When the drive was not in use, the slider was resting in physical contact with the disk. As soon as the drive started, an air bearing was beginning to form and the slider started flying. The use of "contact-start-stop" led to stiction and wear on slider and disk during the start and stop of the drive. Laser texturing was used to decrease the stiction effects [2, 3]. To increase the areal storage density, disks with ultra smooth surfaces were needed. The use of such disks increased the problem of stiction and wear between slider and disk. To eliminate these problems, a so-called load/unload mechanism was introduced [42]. Figure 1.24 illustrates a typical load/unload mechanism. As can be seen from the figure, during the non-operational state of the hard disk drive the slider is "parked" on a ramp. During operation, the slider is moved from the ramp and flies over the disk surface. With load/unload, the problems of stiction and wear have been minimized.

1.5.2 Suspensions

The slider is attached to the suspension via a gimbal as shown in Figure 1.25 and 1.26. The assembly of slider, gimbal and suspension is sometimes referred to as head-gimbal-assembly (HGA) and is attached to the rotary actuator arm.

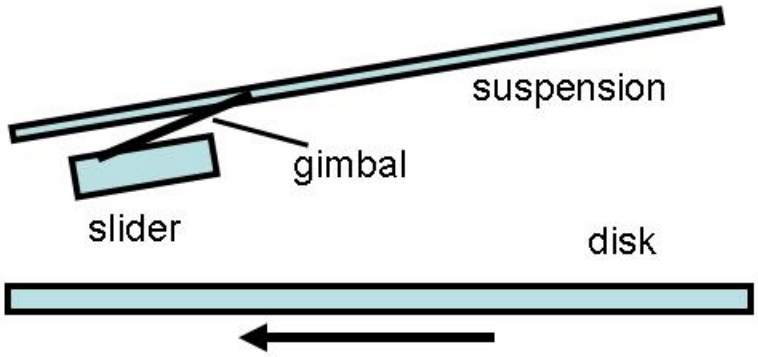

Figure 1.25: Schematic head-gimbal-suspension assembly

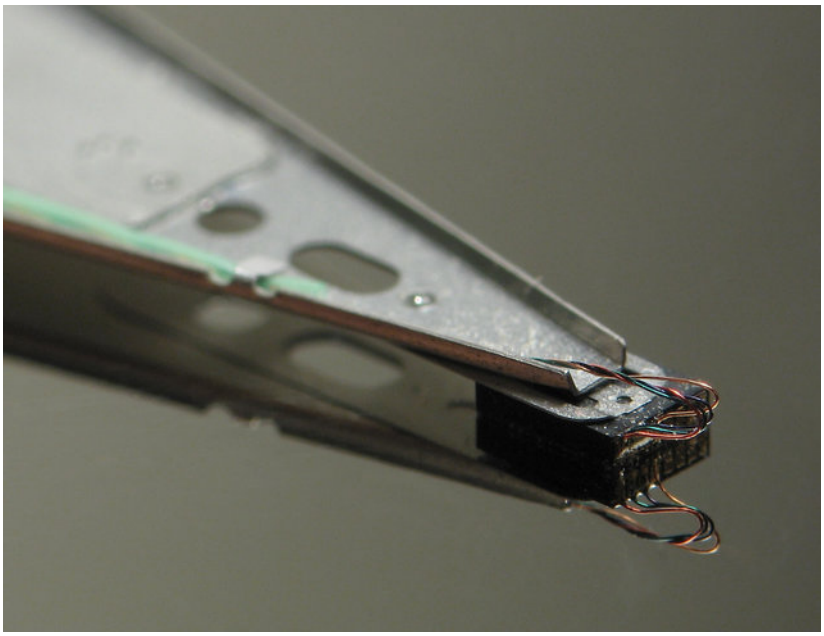

Figure 1.26: Photograph of electrical connections for read/write element (source [16])

The main functions of the suspension are to

a) support the slider with a constant and stable flying height,

b) provide the necessary stiffness in the radial direction to allow precise and fast positioning of the slider in the radial direction,

c) provide electrical connectivity.

A disk in a computer hard disk drive is distorted by disk clamps and clamping imperfections, i.e., a slider does not fly over a flat surface but flies over an undulating surface. The suspension provides a force that is in equilibrium with the air bearing pressure. The amount of force provided by the suspension directly affects the flying height of the slider, the magnetic spacing and the performance of the hard disk drive. Additionally, the force must be applied at a location that ensures that no undesired torque is applied to the slider. Any additional torque on the slider affects its position relative to the disk, thereby influencing the characteristics of the air bearing. Besides providing the pre-load on the slider, the suspension must allow the slider to rotate in the pitch and roll directions so that it can stay close to the disk regardless of undulations of the disk surface. (A mathematical description of the forces generated by the head-gimbal-assembly is given in chapter 4.)

A suspension must be compliant in the vertical, pitch and roll direction of the slider. On the other hand, high stiffness is required for in-plane and torsional vibration modes. A high stiffness is needed so that the actuator can move the slider across the disk surface without causing vibrations in the radial direction. Radial or "in-plane" vibrations can lead to track mis-registration and read/write errors,

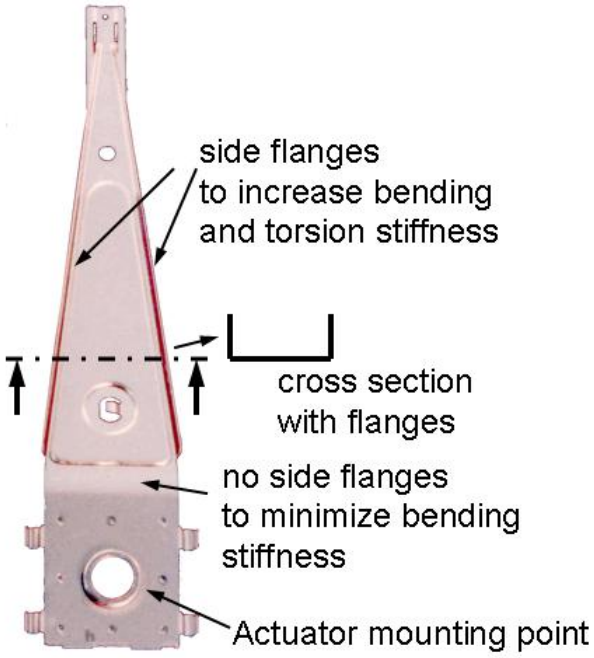

Figure 1.27: Photograph of typical suspension with design features annotated (source [16])

and are therefore highly undesirable. Figure 1.27 shows how the different stiffness requirements for the vertical, pitch and roll direction of the slider are incorporated in a typical suspension design. Flanges along the length of the suspension provide stiffness for the in-plane and rotational vibration modes. Flanges are missing close to the actuator mounting point, thereby providing a low bending stiffness and allowing compliance for the vertical direction of the slider motion.

Since the slider is attached to the suspension, electrical connectivity has to be provided for the read/write element. Figure 1.26 shows a photograph of the electrical connections to the read/write head provided by the suspension. As can be seen

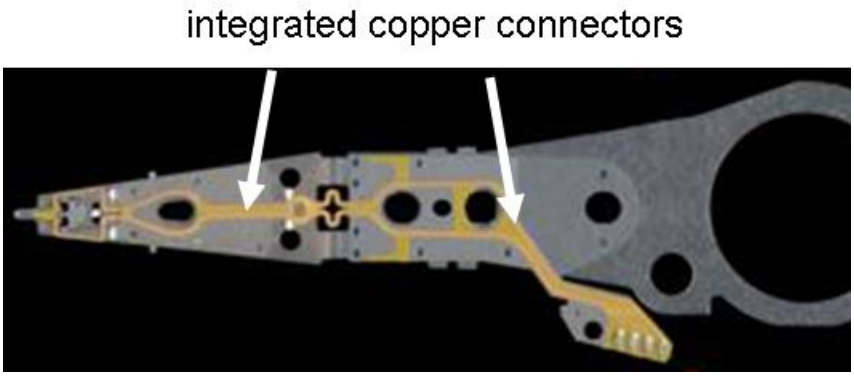

Figure 1.28: Photograph of suspension design with integrated copper conductors (source [16])

from Figure 1.26, the electrical connections are provided by small twisted wires. The wires contribute to the overall stiffness of the head-gimbal-assembly, i.e., the stiffness provided by the electrical connections has to be taken into account during the suspension design process. Providing the electrical connectivity with wires is becoming increasingly more challenging with decreasing slider size and increased track densities. The latest suspension designs have the copper conductors built in to provide connectivity. A suspension design with integrated copper conductors is shown in Figure 1.28.

The increase in areal storage density has affected the design of air bearing sliders as well as that of the suspension design. Figure 1.29 shows the evolution in suspension design as a function of time. The suspension length is plotted as a function of time. Additionally, photographs of typical suspension designs are

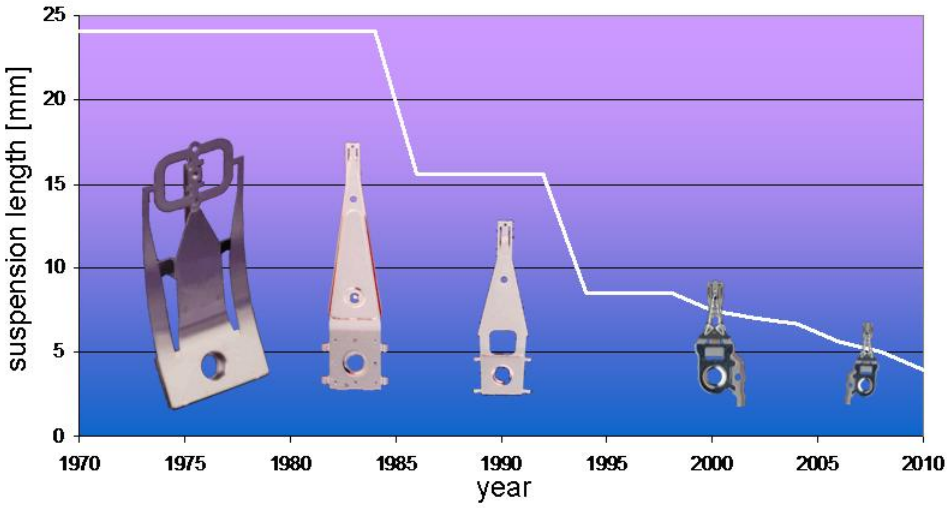

Figure 1.29: Evolution of suspension design (source [16])

given in Figure 1.29. As can be seen, the length of a typical suspension decreased from initially $24mm$ to a length below $5mm$. The length of the suspension was also influenced by the introduction of new form factors for hard disk drives. Today, hard disk drives with a disk diameter of $0.85in$ are available for the use in consumer products such as cell phones or digital music players. In the design process of modern suspensions, numerical simulation tools are used for topography optimization [21, 53] to incorporate the conflicting suspension design goals in an optimal way.

Current suspensions are made from $15 - 20\mu m$ thick sheets of stainless steel. Copper conductors with a thickness of $12\mu m$ are laminated onto the stainless steel suspension. Forming such thin layers of metal is challenging from a manufacturing

point of view. Stamping and photo-chemical etching processes are used in the manufacturing of modern suspensions [16].

1.5.3 Spindle Motor Bearings

The spindle motor in a computer hard disk drive is required for the rotation of the disks. In modern hard disks drives, the disks are spinning with a rotational speed between 5400 and 15000 rotations per minute (rpm). Traditionally, ball bearing spindle motors were used. A ball bearing spindle is shown in Figure 1.30. As can be seen in the figure, the rotating hub is separated from the static part of

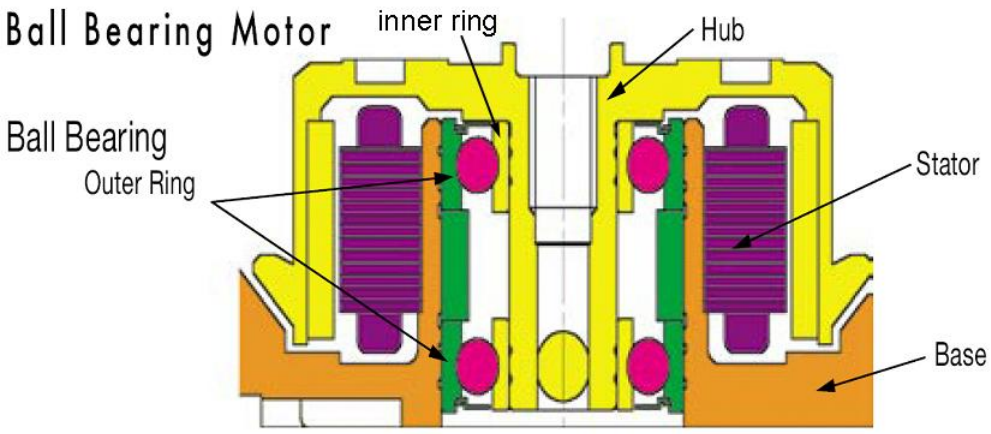

Figure 1.30: Schematic of ball bearing spindle motor (source [6, 13])

the spindle motor by ball bearings. The ball bearings are lubricated with grease or oil to minimize friction and wear.

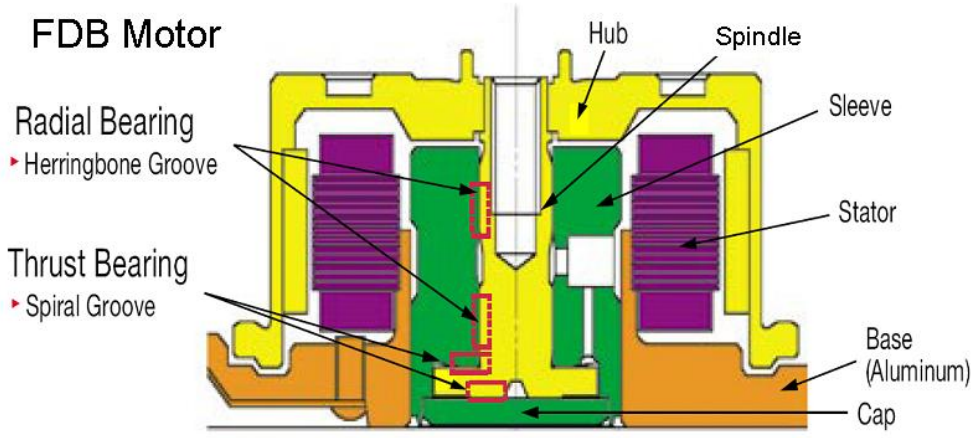

Figure 1.31: Schematic of fluid dynamic bearing (FDB) spindle motor (source [6, 13])

In modern hard disk drives, a fluid dynamic spindle motor is used. The need for reducing vibrations and non-repeatable run-out in order to increase the track density were the main factors for the introduction of fluid dynamic spindle motors. In consumer products, the acoustic performance of a hard disk drive is also an important parameter. By using fluid dynamic bearings the noise level of a hard disk drive can be reduced by up to $20dB$ [6].

A fluid bearing spindle motor is shown in Figure 1.31. As can be seen from the figure, the rotating hub is separated by a radial fluid bearing from the stationary part of the spindle motor. In addition to the radial bearing, a thrust bearing is needed to support the rotating spindle/hub assembly in the axial direction. The hydrodynamic fluid bearing used in hard disk drives feature generally

Herringbone groove bearings for the radial support and spiral groove bearings for the axial support. Hydrodynamic spindle bearings reduce track mis-registration and the acoustic noise level of the hard disk drive. However, they are sensitive to temperature variations [6] and require fluid seals to prevent fluid leakage.

1.5.4 Magnetic Disks

The magnetic disks provide the storage medium in computer hard disk drives. So-called thin film disks are used in modern hard disk drives. These disks have a multilayer structure depending on the magnetic storage technology and disk substrate material used. The layered structure of a disk for perpendicular recording is different from that of a disk designed for longitudinal recording. Glass or aluminum are typically used as substrate materials for magnetic disks. Figure 1.32 shows a schematic of the layered structure of a magnetic disk. A nickel phosphorous un-

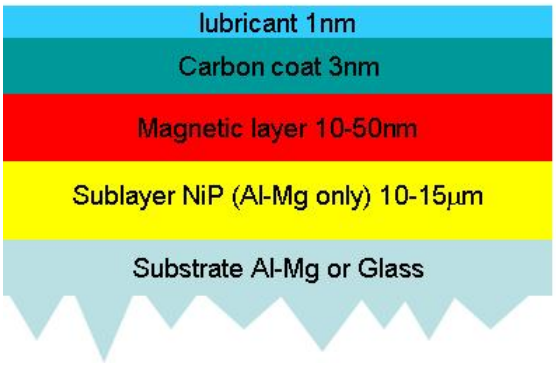

Figure 1.32: Schematic of layered structure of magnetic disk

derlayer is deposited on aluminum disks before the magnetic layer is applied. The nickel phosphorous underlayer is needed for aluminum disks to prevent corrosion of the substrate material. It is not required for glass disks. The magnetic layer consists generally of a $10-25nm$ thick film of cobalt alloy (Co–Cr–Ta, Co–Cr–Pt) [25] and is applied by sputtering or chemical vapor deposition (CVP). The magnetic layer on the disk surface is protected by a thin carbon film on the order of $3nm$ thickness. A lubricant film approximately $1nm$ thick is applied to the top of the disk surface. If perpendicular recording is used, an additional magnetically soft underlayer is deposited prior to the magnetic layer. The carbon overcoat provides wear and corrosion protection of the magnetic material. Both, the carbon overcoat and the lubricant layer, are needed to protect the magnetic layer from wear due to slider/disk contacts.

The disk surfaces in hard disk drives must provide a durable interface for flying of a slider on the disk surface. In addition, the disk surface must be very smooth to minimize contacts between slider and disk.

The interface of the disk and the flying slider, the so-called head/disk interface, is one of the most complex subsystems of a computer hard disk drive. The majority of problems related to increasing the areal storage density are related to effects encountered at the interface of air bearing slider and disk. Several phenomena have to be considered in the design of the head/disk interface. These phenomena include

friction, wear, lubrication, contact between rough surfaces, hydrodynamic lubrication, and adhesion. In the next section of this thesis, some head/disk interface parameters are defined.

1.6 Head/Disk Interface

The interface between the flying slider and the rotating disk in a computer hard disk drive is called the head/disk interface (HDI). The performance and reliability of the head/disk interface is closely related to the performance and reliability of the entire hard disk drive. Conflicting design goals have to be considered during the development of the head/disk interface. The main objective that has to be achieved is the reduction of flying height so that contact, friction and wear on slider and disk are minimized. This part of the thesis introduces parameters for the characterization of the head/disk interface. Some of the problems encountered in the design of ultra low spacing head/disk interfaces are outlined.

The surfaces of disks in computer hard disks drives are considered among the smoothest engineered surfaces available. However, on a nano-scale, disk surfaces are not smooth. Figure 1.33 depicts a typical surface topography profile of a magnetic recording disk for one revolution at a fixed radius. As can be seen from Figure 1.33, a typical disk profile exhibits low and high frequency components. The low frequency component is referred to as the vertical disk run-out or waviness of

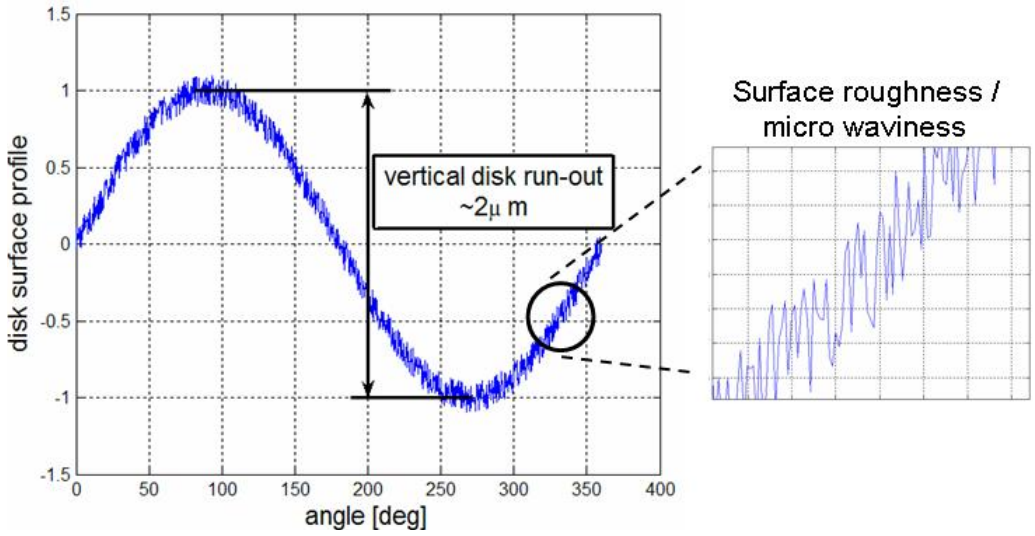

Figure 1.33: Schematic of a typical disk topography profile for one revolution

the disk. A typical disk has a vertical run-out on the order of approximately $2\mu m$. To compensate for the vertical disk run-out, the gimbal and suspension have a low stiffness in the vertical direction, thereby allowing the slider to follow the waviness of the disk.

The high frequency component of the disk topography profile consists of two parts: microwaviness and roughness of the disk. Microwaviness has a lower frequency than the roughness. The frequencies related to microwaviness and roughness are generally to high for the slider to follow and can lead to contact between slider and disk. In chapter 2 and 3 of this thesis, experiments are introduced that investigate the effect of microwaviness and roughness on the flying characteristics

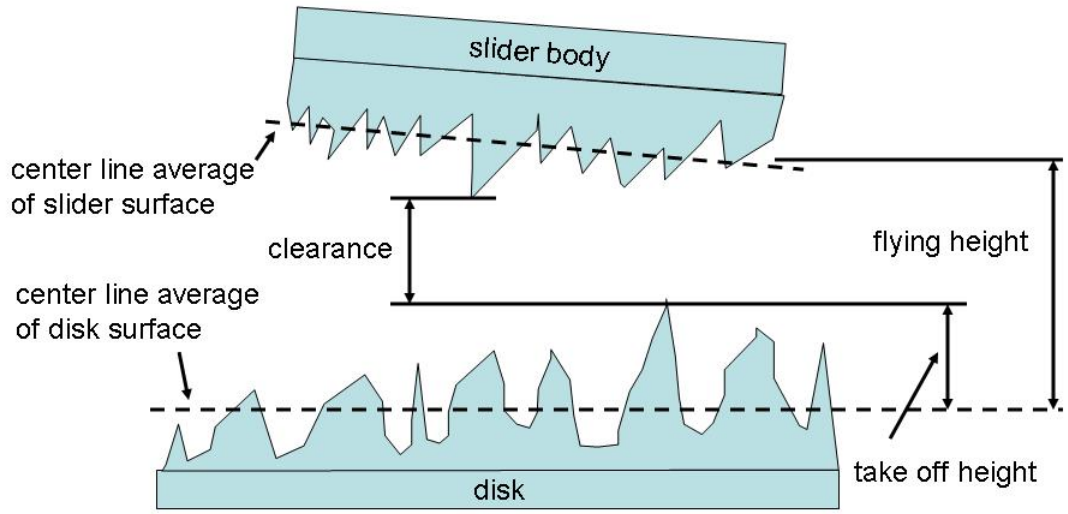

Figure 1.34: Definition of head/disk interface spacing parameters

of sliders. The definition of microwaviness will be given in chapter 2. In this thesis, the roughness of a disk is characterized by the center line average roughness R_{cla} and the root mean square roughness R_{rms}. The definitions of the centerline average roughness and root mean square roughness are given in appendix A.1.

In Figure 1.34, a schematic of the disk and slider surfaces is shown. For clarity, the roughness of the slider and disk are exaggerated. The parameters defined are the take-off height, the clearance, and the flying height. The take-off height is the maximum asperity height on the disk surface measured from the center line average, i.e., from the mean surface of the disk. The clearance is defined as the minimum distance between the slider and the disk. The flying height of a slider is defined as the distance between the center line average of the disk surface and

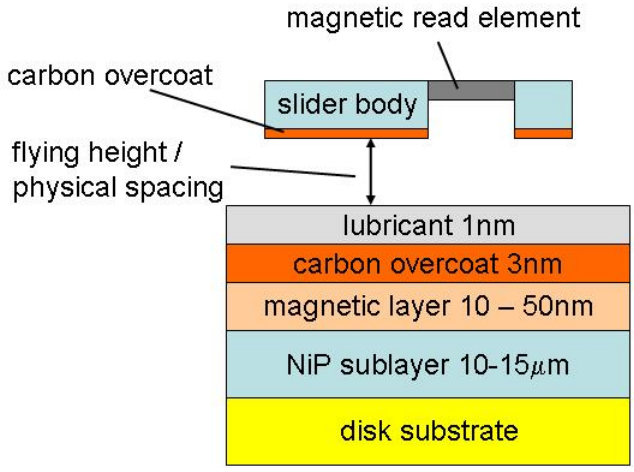

Figure 1.35: Schematic of the multilayered structure of the head/disk interface

the center line average of the slider surface, i.e., the distance between the mean surface of the disk and the mean surface of the slider.

Estimates have shown that a flying height of $2.5nm$ is needed for an areal storage density of $1Tbit/in^2$ [17]. At such a low spacing, the head/disk interface poses a challenging tribological problem. The root mean square (rms) roughness of the disks in current hard drives is on the order of $0.2 - 0.3nm$. The head/disk interface is designed so that the slider flies over the disk without contact between slider and disk. However, due to the dynamics of the head/disk interface asperity contacts do occur during normal operation.

A spacing of $2.5nm$ is approaching the atomic level. It has been shown that for spacings below $5nm$, *van der Waals* forces between slider and disk add a highly

nonlinear force component to the head/disk interface and must be taken into account in the design process [52]. An outline of how van der Waals forces can be included in the head/disk interface design process is given in appendix A.2.

The next chapter of this thesis introduces an experimental setup for local clearance measurements using voltage pulsing. The dependence of clearance on microwaviness and roughness is investigated and the experimental results are presented.

1.7 Organization of the Thesis

Chapter 1 is an introduction to basic principles of magnetic recording and its history. The main components and functions of a computer hard/disk drive are explained and illustrated. The organization of this thesis is presented.

Chapter 2 introduces an experimental setup for localized clearance measurements of the head/disk interface. Several parameters affecting clearance are investigated.

Chapter 3 introduces an experimental setup to create flying height modulation and microwaviness maps using laser Doppler vibrometry (LDV) and acoustic emission (AE) transducers.

Chapter 4 provides an overview of the mathematical background for hydrodynamic lubrication for air bearing simulations of the head/disk interface of computer

hard disk drives. The governing equations are derived and a finite element solution is presented. This chapter is the theoretical background for the simulation results presented in chapter 5.

Chapter 5 presents the simulation results based on the theory of hydrodynamic lubrication. This chapter investigates the effect of discrete tracks on the steady state flying behavior of sub-ambient proximity sliders. A finite element based air bearing simulator is used to study the flying characteristics of sliders over a discrete track disk surface.

Chapter 6 introduces a particle based simulation method: direct simulation Monte Carlo (DSMC). The main steps of a DSMC simulation program are outlined. Limitations and sources of errors in DSMC simulations are explained. This chapter provides the theoretical background for the simulation results presented in chapter 7.

Chapter 7 presents simulation results based on the direct simulation Monte Carlo method (DSMC). DSMC simulations are used to study rarefied gas flow between an inclined plane slider bearing and a nano channel representing one groove of a discrete track recording head/disk interface. The forces acting on the slider are investigated as a function of the slider pitch angle, the disk velocity, the track pitch, the groove width, and the groove depth.

Chapter 8 summarizes this thesis.

Bibliography

[1] Baibich, M., Broto, J., Fert, A., Nguyen Van Dau, F., and Petroff, F. *Giant Magnetoresistance of (001)Fe/(001)Cr Magnetic Superlattices*. Phys. Rev. Letter, 61(21):2472–2475, 1988.

[2] Baumgart, P., Krajnovich, D., Nguyen, T., and Tam, A. *A New Laser Texturing Technique for High Performance Magnetic Disk Drives*. IEEE Trans. Magn., 31(6):2946–2951, 1995.

[3] Baumgart, P., Krajnovich, D., Nguyen, T., and Tam, A. *Safe Landings: Laser Texturing of High Density Magnetic Disks*. Data Storage, pages 21–26, 1996.

[4] Bertram, H. *Theory of Magnetic Recording*. Cambridge, 1994.

[5] Bertram, N. and Williams, M. *SNR and Density Limit Estimates: A Comparison of Longitudinal and Perpendicular Recording*. IEEE Trans. Mag., 36 (1), 2000.

[6] Blount, W. *Fluid Dynamic Bearing Spindle Motors*. Hitachi White Paper, 2005.

[7] Bushan, B. *Tribology and Mechanics of Magnetic Storage Devices*. Springer, 2nd edition, 1996.

[8] Charap, S., Pu-Ling, L., and Yanjun He. *Thermal Stability of Recorded Information at High Density*. IEEE Trans. Mag., 33(1):978–983, 1997.

[9] Dorius et al. *Negative Pressure Slider with Optimized Leading Pocket for Profile Control*. U.S. Patent No. 5,583,722, 1991.

[10] Gao, K. and Bertram, H. *Transition Jitter Estimates in Tilted and Conventional Perpendicular Recording Media at* $1Tbit/in^2$. IEEE Trans. Mag., 39(2):704–709, 2003.

[11] Gao, K., Williams, M., Z., H., Fernandez-de-Castro, J., and Bertram, H. *Thermal Decay and Erasure Process for Perpendicular Recording at* $1Tb/in^2$. IEEE Trans. Mag., 40(4):2449–2451, 2004.

[12] Harker, J. et al. *A Quarter Century of Disk File Innovation*. IBM J. Res. Develop., 25:677–689, 1981.

[13] Hitachi Global Storage Technologies. *www.hitachigst.com*.

[14] Hsia, Y. *An Overview of Heat Assisted Magnetic Recording and Associated Tribology Challenges*. Proc. ASME/STLE Jt. Trib. Conf. Cancun, 2002.

[15] Hunt, R. *A Magnetoresistive Readout Transducer*. IEEE Trans. Mag., 7(1):150–151, 1971.

[16] Hutchinson Technology. *www.htch.com*.

[17] Information Storage Industry Consortium. *www.insic.org*.

[18] International Business Machine Corporation. *www-03.ibm.com*.

[19] Jorgensen, F. *The Complete Handbook of Magnetic Recording*. Tab Books, fourth edition, 1980.

[20] Julliere, M. *Tunneling between Ferromagnetic Films*. Phys. Lett., 54A:225–226, 1975.

[21] Kilian, S., Zander, U., and Talke, F. *Suspension Modeling and Optimization Using Finite Element Analysis*. Trib. Int., 36:317–324, 2003.

[22] Kokierok, C. *The PC Guide*. www.PCGuide.com.

[23] Kryder, M. *Magnetic Recording beyond the Superparamagnetic Limit*. Intermag 2000 Digest of Technical Papers, page 575, 2000.

[24] Kryder, M. *Future Trends in Magnetic Storage Technology*. In *Digest of Technical Papers, Joint NAPMRC 2003*, page 68. 2003.

[25] Lawrence-Comstock, R. *Introduction to Magnetism and Magnetic Recording*. John Wiley & Sons, 1999.

[26] Mallary, M., Torabi, A., and Benakli, M. *One Terrabit per Square Inch Perpendicular Recording Conceptual Design*. IEEE Trans. Mag., 38(4):1719–1724, 2002.

[27] Mee, C. and Daniel, E. *Magnetic Recording Technology*, volume 1. McGraw-Hill, 1987.

[28] Moodera, J. and Mathon, G. *Spin Polarized Tunneling in Ferromagnetic Junctions*. Magn. Mater., 200:248–273, 1999.

[29] Moodera, J. S. et al. *Large Magnetoresistance at Room Temperature in Ferromagnetic Thin Film Tunnel Junctions*. Phys. Rev. Lett., 74:3273–3276, 1995.

[30] Peng, J.-P., Wang, G., Thrivani, S., Chue, J., Nojaba, M., and Thayamballi, P. *Numerical and Experimental Evaluation of Discrete Track Recording Technology*. IEEE Trans. Mag., 42(10):2462–2464, 2006.

[31] Pu-Ling, L. and Charap, S. *High Density Recording Media Design and Identification: Suspect to Thermal Decay*. IEEE Trans. Mag., 31(6):2767–2769, 1995.

[32] Rabinow, J. *The Notched-Disk Memory*. Electrical Engineering, 1952.

[33] Richter, H., Dobin, A., Heinonen, O., Gao, K., v.d. Veerdonk, R., Lynch, R., Xue, J., Weller, D., Asselin, P., Erden, M., and Brockie, R. *Recording on Bit-Patterned Media at Densities of* $1Tb/in^2$ *and Beyond*. IEEE Trans. Mag., 42(10):2255–2260, 2006.

[34] Rottmayer, R., Batra, S., Buechel, D., Challener, W., Hohlfeld, J., Kubota, Y., Li, L., Lu, B., Mihalcea, C., Mountfield, K., Pelhos, K., Peng, C., Rausch, T., Seigler, M., Weller, D., and Yang, X.-M. *Heat-Assisted Magnetic Recording*. IEEE Trans. Mag., 42(10):2417–2421, 2006.

[35] Schirle, N. and Lieu, D. *History and Trends in the Development of Motorized Spindles for Hard Disk Drives*. IEEE Trans. Mag., 32 (3), 1999.

[36] Schoenherr, S. *The History of Magnetic Recording*. history.sandiego.edu/gen/recording/magnetic4.html, published online, 2002.

[37] Seagate Technology. *www.seagate.com*.

[38] Silicon-Valley-Sleuth. *www.siliconvalleysleuth.com*.

[39] Singer, P. *Read/Write Heads: The MR Revolution*. Semiconductor International, page 71, 1997.

[40] Soeno, Y., Moriya, M., Kaizu, A., and Takai, M. *Performance Evaluation of Discrete Track Perpendicular Media for High Recording Density*. IEEE Trans. Mag., 41 (10):3220–3222, 2005.

[41] Soeno, Y., Moriya, M., and other. *Feasibility of Discrete Track Perpendicular Media for High Track Density Recording*. IEEE Trans. Mag., 39 (1):1967–1971, 2003.

[42] Suk, M. *Ramp Load/Unload Technology in Hard Disk Drives*. Hitachi White Paper, 2005.

[43] Tarnopolsky, G. *Hard Disk Drive Capacity at High Magnetic Areal Density*. IEEE Trans. Mag., 40(1):301–306, 2004.

[44] Victora, R., Jianhua, X., and Patwari, M. *Areal Density Limits for Perpendicular Magnetic Recording*. IEEE Trans. Mag., 38(5):1886–1890, 2002.

[45] Wachenschwanz, D., Jiang, W., Roddick, E., et al. *Design of a Manufacturable Discrete Track Recording Medium*. IEEE Trans. Mag., 41 (2):670–675, 2005.

[46] Wallace, R. *The Reproduction of Magnetically Recorded Signals*. Bell Syst. Tech. J., 30, 1951.

[47] Warner et al. *Magnetic Head Air Bearing Slider*. U.S. Patent No. 4,475,135, 1986.

[48] Weissner, S., Tonder, K., and Talke, F. *Surface Roughness Effects in Compressible Lubrication*. In *Proceedings of AUSTRIB 1998, Brisbane*. 1998.

[49] Weller, D. and Moser, A. *Thermal Effect Limits in Ultrahigh-Density Magnetic Recording*. IEEE Trans. Mag., 35(6):4423–4439, 1999.

[50] White, J. *A Magnetic Head Air Bearing Slider Assembly Utilizing Transverse Pressurization Countours*. U.S. Patent No. 4,673,996, 1987.

[51] Wood, R. *The Feasibility of Magnetic Recording at 1 Terabit per Square Inch*. IEEE Trans. Mag., 36 (1), 2000.

[52] Wu, L. and Bogy, D. *Effects of the Intermolecular Forces on the Flying Attitude of Sub-5 NM Flying Height Air Bearing Sliders in Hard Disk Drives*. Trans. ASME, 124:562–567, 2002.

[53] Yu, S. and Liu, B. *Optimal Suspension Design for Femto Sliders*. IEEE Trans. Mag., 39(5):2423–2425, 2003.

[54] Zhang, J., Ji, R. X., J.W., Ng, J., Xu, B., Hu, S., Yuan, H., and Piramanayagam, S. *Lubrication for Heat-Assisted Magnetic Recording Media*. IEEE Trans. Mag., 42(10):2546–2548, 2006.

2

Voltage Pulsing for Localized Clearance Measurement

Mechanical clearance is a critical parameter of the head/disk interface (HDI) for sliders flying in close proximity in hard disk drives. It depends on a variety of HDI parameters, such as the air bearing design, disk roughness, and the disk lubricant. An experimental setup was developed to determine the mechanical clearance locally at any location on the disk. Voltage pulsing is used to add an additional force component to the complex head/disk interface equilibrium. The applied force is attractive in character and therefore reduces the mechanical spacing between the slider and the disk. If the magnitude of the applied voltage is changed, a contact between the slider and the disk can be realized. Simultaneous

measurement of the induced slider displacement using a laser Doppler vibrometer allows quantification of the mechanical clearance. The effect of disk roughness and microwaviness on the mechanical clearance was investigated. In this study experimental techniques called laser Doppler vibrometry and acoustic emission are used. Introductions to laser Doppler vibrometry and acoustic emission techniques are provided in appendix B.1 and B.2, respectively.

2.1 Introduction

In ultra low spacing head/disk interfaces of future hard drives, the flying height is not representative of the physical spacing between slider and disk. Flying height is defined as the distance between the mean values of the surface roughness of the disk and the slider. For a disk with an rms roughness value of $0.3nm$, the peak-to-valley distance is approximately $3nm$. Sliders in future hard drives are predicted to fly at $2.5nm$. Therefore, contact between single asperities of disk and slider is likely to occur. The clearance of a given head/disk interface is defined as the distance between the highest asperities of the disk and the highest asperities of the slider. Thus, clearance describes the available physical spacing much better than flying height. Due to the distribution of asperities on head and disk, the clearance is likely to vary over the disk surface. A localized clearance measurement method is thus desirable.

This chapter introduces a method for such a localized clearance measurement by applying an external voltage pulse to the head/disk interface, resulting in an additional force. The force is electrostatic and therefore attractive. As a result, the clearance decreases. By varying the magnitude of the applied voltage pulse, one can induce contact between slider and disk. Clearance can be estimated by monitoring the slider displacement until contact occurs. Contact can be detected by acoustic emission.

2.2 Experimental Setup

In Figure 2.1, a schematic of the experimental setup is shown. The setup consists of an air bearing spindle, a fixture for mounting the suspension/head assembly, a laser Doppler vibrometer, an acoustic emission sensor and a data acquisition system. The air bearing spindle is computer controlled to allow adjustment of the rotational speed of the disk. The spindle provides an index signal for every new rotation. The suspension fixture is attached to a computer controlled stepper motor assembly that allows the exact positioning of the slider above the disk. The acoustic emission sensor is attached to the suspension fixture.

A laser Doppler vibrometer was used for the slider displacement measurement. Acoustic emission was used to detect contact between slider and disk.

The data acquisition computer was equipped with high speed data acquisition

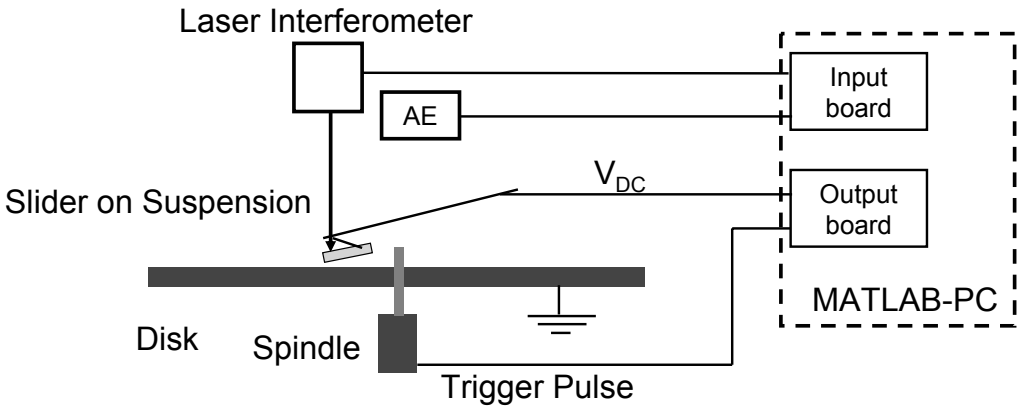

Figure 2.1: Experimental setup for localized clearance measurement using voltage pulsing

cards. The output signal was discretized with 16bit resolution. The input channels of the data acquisition card were used for obtaining the velocity signal from the laser Doppler vibrometer, the acoustic emission signal, and the applied voltage. The laser Doppler vibrometer, acoustic emission, and applied voltage signals were triggered simultaneously using the spindle index signal. $MATLAB^{®}$ and its appropriate toolboxes for instrument control and data acquisition were used for acquiring and processing the data.

To reduce the noise level of the measurement, averaging was performed. The vertical disk run-out was on the order of 1 to $2\mu m$. The clearance change due to voltage pulsing was expected to be on the order of the flying height, i.e., on the order of nanometers. This value is several orders of magnitude smaller than the disk run-out. Linear trends and offsets in the acquired signal were removed during post-processing to compensate for the effect of disk run-out.

2.3 Experimental Results

A. Detection of contact

Figure 2.2, 2.3 and 2.4 show typical experimental results for measurements where contact between slider and disk is absent. Figure 2.2a shows the average displacement signal versus time for different applied voltages, while Figure 2.2b shows the applied voltages versus time. The duration of the pulse was $50\mu s$ corresponding to a lateral distance of approximately $1.6mm$ at a disk rotational speed of $5k$ rotations per minute (rpm).

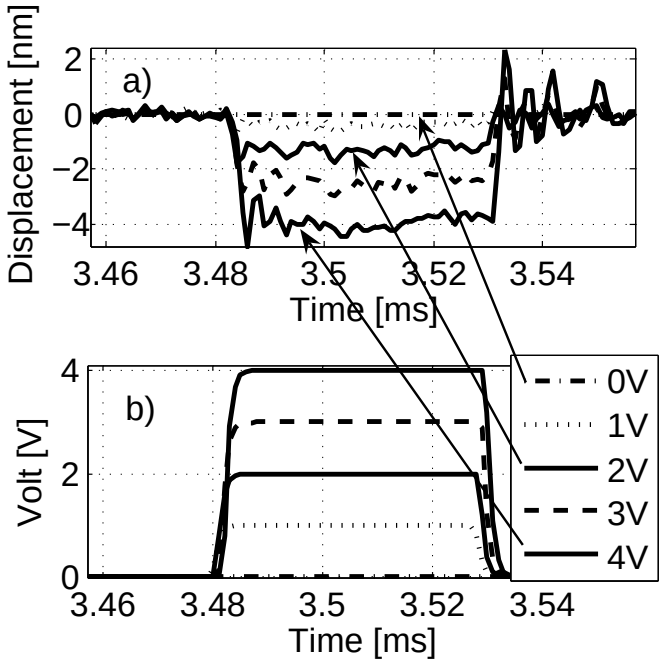

Figure 2.2: Slider displacement (a) and applied voltage (b) versus time; rotational speed: $5krpm$

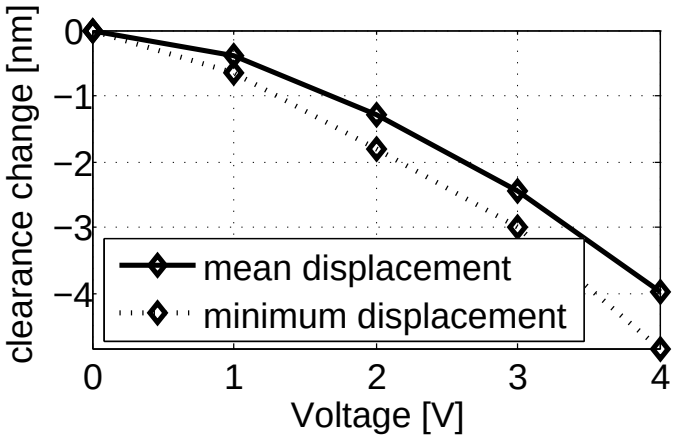

Figure 2.3: Minimum and mean clearance change versus applied voltage; rotational speed: $5krpm$

Figure 2.3 shows the clearance change versus the applied voltage corresponding to the data shown in Figure 2.2. Two curves are displayed. The upper one shows the mean clearance change during the time the voltage was applied. The lower curve shows the minimum displacement value obtained during pulsing.

The electrostatic force between two parallel capacitor plates due to an applied voltage is given by

$$F_{electrostatic} = \frac{\epsilon_0 \epsilon_r V^2 A}{2d^2} \tag{2.1}$$

where ϵ_0, ϵ_r are the dielectric constants of free space and air, respectively; V is the applied voltage; A is the area and d is the separation of the capacitor plates. The slider displacement due to an applied voltage is related to the electrostatic force described in equation 2.1, where d and A are affected by the geometry of the slider and the position of the slider relative to the disk. The force depends on the square

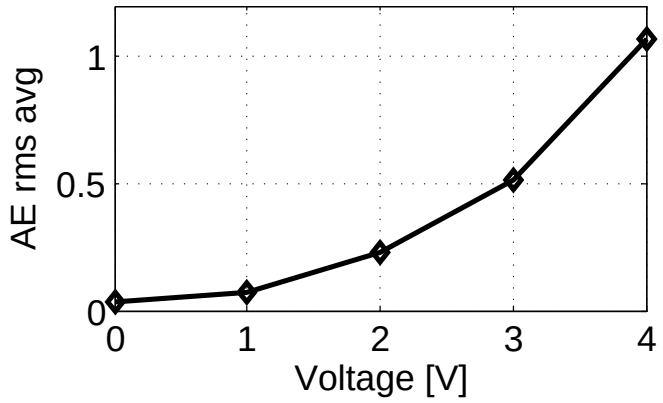

Figure 2.4: Acoustic emission signal (rms) versus applied voltage; rotational speed: $5krpm$

of the applied voltage. This general trend is observed in Figure 2.3.

In Figure 2.4 the root mean square (rms) value of the acoustic emission signal during pulsing is plotted versus the applied voltage. The root mean square value increases with voltage.

The data shown in Figures 2.5, 2.6 and 2.7 are similar to those shown in Figures 2.2, 2.3 and 2.4, except that the disk rotational speed is reduced to $4krpm$. From Figure 2.5a one can observe that the displacement increases initially with voltage. At a voltage of $1.5V$, the displacement becomes constant and does not increase further even if the voltage is raised above $1.5V$. It is apparent that this phenomenon occurs because slider and disk are in contact at a voltage of $1.5V$ and a further increase in voltage does not allow a further reduction in spacing. In Figure 2.5b small dips in the voltage signal can be observed for voltages of $1.5V$ and

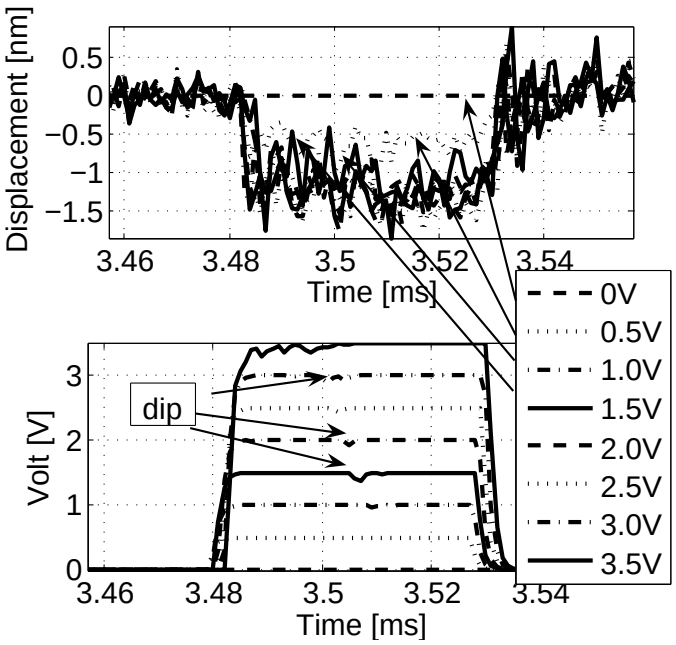

Figure 2.5: Slider displacement (a) and applied voltage (b) versus time; rotational speed: $4krpm$

higher. These dips are due to discharge currents occurring as a result of contact between slider and disk. Figure 2.6 summarizes the data shown in Figure 2.5a. One can again notice that the displacement does not decrease further than the value observed at a voltage of $1.5V$. Clearly, contact is present. Figure 2.7 shows that the rms value of the acoustic emission signal is constant for voltages between $1.5V$ and $3.5V$, confirming the conclusion that contact is present.

For a localized measurement of clearance, the voltage pulse should be short. However, each voltage application excites slider oscillation, (Figure 2.2). To achieve a reliable measurement, the voltage pulse needs to be long enough to allow stabilization of the new flying height. Voltage pulses of $50\mu s$ duration were used for all

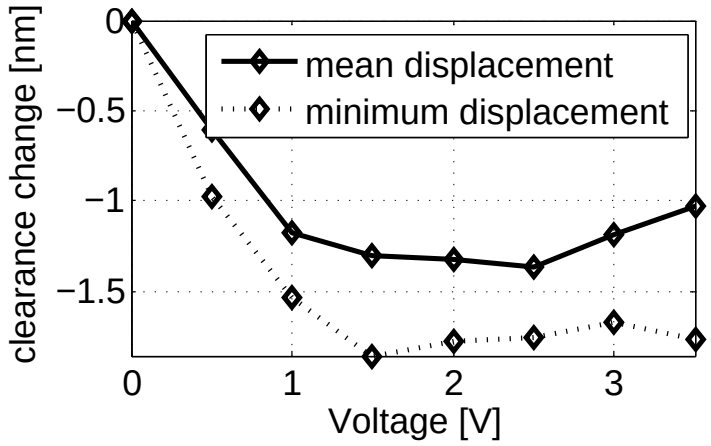

Figure 2.6: Minimum and mean clearance change versus applied voltage; rotational speed: $4krpm$

experiments in this study.

B. Clearance change as a function of disk roughness and microwaviness

The effect of disk roughness and microwaviness on the clearance was investigated. A slider with a symmetric air bearing design and a linear dependence of flying height on disk speed was used. Auxiliary measurements of the slider displacement at inner and outer trailing edge showed that no roll motion of the slider was induced during voltage pulsing. Thus, it is justifiable to assume that for this particular slider, contacts due to voltage pulsing occur in the center region of the trailing edge.

For the evaluation of the effect of roughness, three disks (A, B and C) with

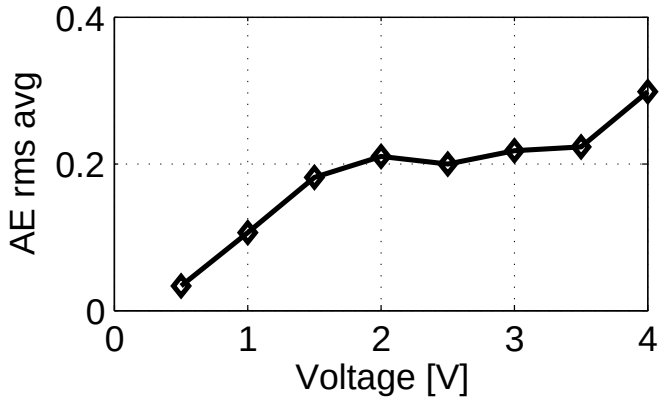

Figure 2.7: Acoustic emission signal (rms) versus applied voltage; rotational speed: $4krpm$

root mean square values of surface roughness of $0.38nm$, $0.52nm$ and $0.75nm$, respectively, were used. All disks were coated with the same carbon overcoat and the same lubricant. The microwaviness of the disks ranged from $0.3 - 0.45nm$. Here, microwaviness is arbitrarily defined as the mean value of the upper one percent of the amplitudes of the band pass filtered disk displacement signal (low pass wavelength λ_{low}=$40\mu m$, high pass wavelength λ_{high}=$1000\mu m$). Figure 2.8 shows the clearance change as a function of the applied voltage for a disk rotational velocity of $7.5krpm$. A well-defined discontinuity can be observed at 3V for all three disks. The discontinuity indicates that contact occurs at this voltage. Surprisingly, the spacing change is nearly the same for disk A with an rms roughness of $0.38nm$ and disk C with an rms roughness of $0.75nm$.

To study the effect of microwaviness, four disks (D, E, F and G) with disk mi-

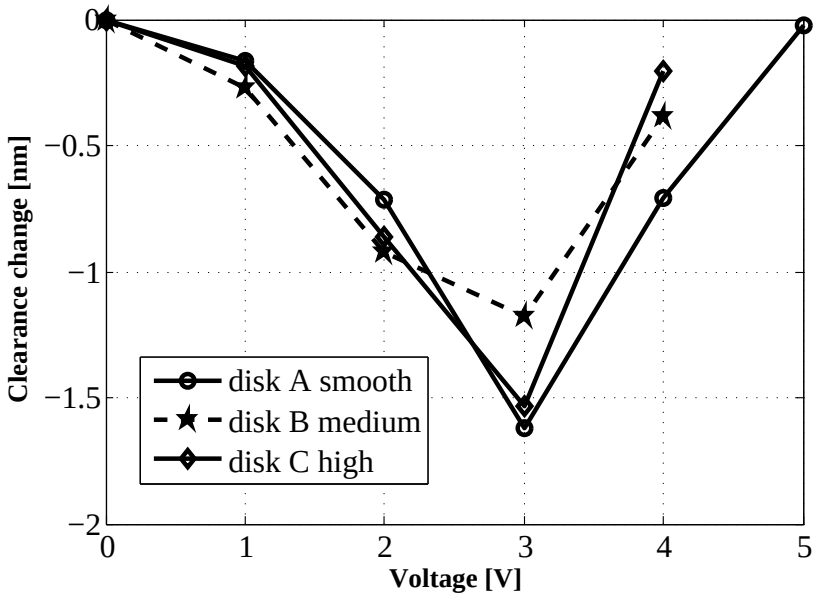

Figure 2.8: Clearance change versus disk roughness, rotational speed: $7.5krpm$

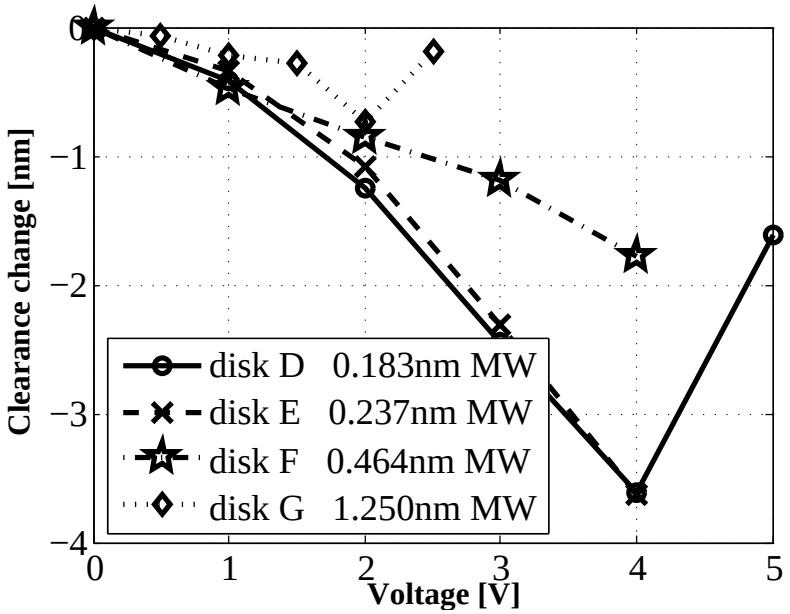

Figure 2.9: Clearance change versus microwaviness (MW), rotational speed: $5krpm$

crowaviness values of $0.183nm$, $0.237nm$, $0.464nm$, and $1.250nm$, respectively, were investigated. All disks were coated with the same carbon overcoat and the same lubricant. The root mean square surface roughness values ranged from $0.35nm$ to $0.55nm$. In Figure 2.9 the clearance change of the head/disk interface is plotted as a function of the applied voltage for the four disks. One observes that the clearance change before contact is largest for disk D, i.e., the disk with the lowest value of microwaviness. On the other hand, disk G, with the highest value of microwaviness, shows the smallest spacing. One can conclude that for the given set of disks a reduction in the amplitude of microwaviness of approximately $1nm$ allows a reduction in the spacing of $3nm$ before contact occurs, i.e., the smaller the disk microwaviness, the larger the permissible clearance change prior to the onset of contact.

2.4 Discussion and Conclusions

Disk surface profiles consist of three frequency regions. These are the low frequency region, often referred to as waviness, the intermediate frequency region, generally called microwaviness, and the high frequency region, generally called roughness. The waviness has the highest amplitude contributions to the disk surface profile, while the disk roughness contributes least to the amplitudes of the disk surface profile. The head/disk interface is designed so that the slider follows

the waviness of the disk profile. The slider cannot follow the microwaviness or disk roughness. Therefore one would expect disk roughness and microwaviness to influence clearance, since disks with high roughness or microwaviness amplitudes are more likely to induce contact due to asperities reaching higher towards the slider.

A dependence of clearance on disk roughness was not found, given the samples used. The microwaviness values of the disks used in the roughness investigation ranged between $0.3nm$ and $0.45nm$. From the results of the microwaviness investigation (Figure 2.9) one finds a clearance of $1.5nm$ for a disk microwaviness of $0.45nm$. To investigate the effect of roughness on clearance one would have to minimize the disk microwaviness for the disk used. Unfortunately, manufacturing of disks with defined microwaviness but varying roughness is very difficult.

The next chapter of this thesis describes an experimental setup used for creating flying height modulation maps of the entire disk surface. This experiment allows investigation of the effect of microwaviness or lubricant thickness variations on slider flying height modulations.

2.5 Acknowledgement

This chapter is a partial reprint of material as it appears in: "***Voltage Pulsing for Localized Clearance Measurements***", by Maik Duwensee, Bernhard

Knigge, Peter Baumgart, and Frank E. Talke, IEEE Transactions on Magnetics, vol.41, no.12, p.4454-6, (2005). The dissertation author was the primary researcher and author and the co-authors listed in this publication directed and supervised the research which forms the basis for this chapter.

Bibliography

[1] Deoras, S. and Talke, F. *Time-Frequency Analysis of Slider Dynamics and the Effect of Lubricant*. ASME J. Trib., 126:559–564, 2004.

[2] Feng, Z., Cha, E., and X., Z. *A Study of Electrical Charge at Head/Disk Interface*. In *Proc. 2004 STLE/ASME Joint Int. Tribology Conference, Long Beach*, pages 1–4. 2004.

[3] Karis, T. *Chemistry of Magnetic Recording Disk Surfaces with Intermittent Asperity Contacts*. IEEE Trans. Magn., 37(2):924, 2001.

[4] Schnur, D., Song, D., Hipwell, R., Boutaghou, Z., and Weinstein, R. *Electrical Breakdown in Electrostatic Fly Control*. In *Proc. 2003 STLE/ASME Joint Int. Tribology Conference, Ponte Vedra Beach*, pages 103–108. 2003.

[5] The MathWorks, Inc. *Matlab: Creating Graphical User Interfaces, User Manual*.

[6] The MathWorks, Inc. *Matlab: Data Acquisition Toolbox 2, User's Guide*.

[7] The MathWorks, Inc. *Matlab: Data Analysis, User Manual*.

[8] The MathWorks, Inc. *Matlab: Graphics, User Manual*.

[9] The MathWorks, Inc. *Matlab: Instrument Control Toolbox 2, User's Guide*.

3

Disk Mapping

The multilayered structure of disks for computer hard disk drives requires several deposition steps during the manufacturing process. Manufacturing tolerances in the processing steps can result in thickness variations of the single layers over the disk surface. Additionally, microwaviness or roughness variations over the disk surface can be expected as a result of manufacturing tolerances. Layer thickness and microwaviness variations affect the flying of the slider. An experimental setup for the evaluation of the effect of layer thickness variations and microwaviness is desirable and is introduced here.

Flying height modulation maps and microwaviness maps are obtained by using laser Doppler vibrometry (LDV) and acoustic emission (AE) transducers which are moved radially over the complete disk surface. The sensitivity of the acoustic

emission measurement was improved by applying a current to the write element. The applied current results in thermal expansion of the slider material in the vicinity of the write element. This effect is called pole tip protrusion. Disk and slider displacement maps are obtained using a radially scratched disk. Acoustic emission maps are presented for a scratched disk and for a non-scratched disk. For the non-scratched disk, acoustic emission maps are obtained with an inactive and active write element.

3.1 Introduction

Microwaviness near the second slider pitch resonance frequency (P2) of approximately $250kHz$ causes flying height modulations. Depending on the rotational speed and the radius of the disk one finds that these wavelengths are typically in the range from $50\mu m$ to $250\mu m$. The P2 frequency of a slider changes with flying height and pole tip protrusion of the read/write element. Zeng and Thornton [10, 11] have studied the influence of microwaviness on slider flying height modulation on a single track using glass and aluminum substrates. In this study their method was extended from a single track to the entire disk. In addition, the effect of thermal pole tip protrusion on slider to disk compliance was investigated. To obtain measurements over the whole disk surface, a stepper motor was used which carries the slider/suspension assembly and the optical head of a laser

Doppler vibrometer (LDV). The stepper motor allows positioning of the slider over the disk surface. The optical head is mounted rigidly relative to the slider.

As the slider disk clearance decreases, the disk roughness, microwaviness and lubricant thickness have to become increasingly more uniform to minimize flying height modulations. Microwaviness variations over the disk surface or within one revolution of the disk can affect the slider flying behavior and may lead to increased lubricant pickup. Therefore, instrumentation is needed that allows the evaluation of slider dynamics over the entire disk.

3.2 Experimental Setup

In Figure 3.1 a schematic of the experimental setup is shown. The setup consists of an air bearing spindle, a fixture for mounting the suspension/head assembly, a laser Doppler vibrometer (LDV), an acoustic emission (AE) sensor and a data acquisition system. The air bearing spindle is computer controlled to allow adjustment of the rotational speed of the disk. The spindle provides an index pulse for each rotation. The suspension is attached to the lower shaft of a computer controlled stepper motor assembly, while the laser head is connected to the upper shaft. The dual shaft stepper motor allows exact positioning of the slider and the laser above the disk surface, while preventing relative motion between the two components. An acoustic emission sensor is attached to the base of the suspen-

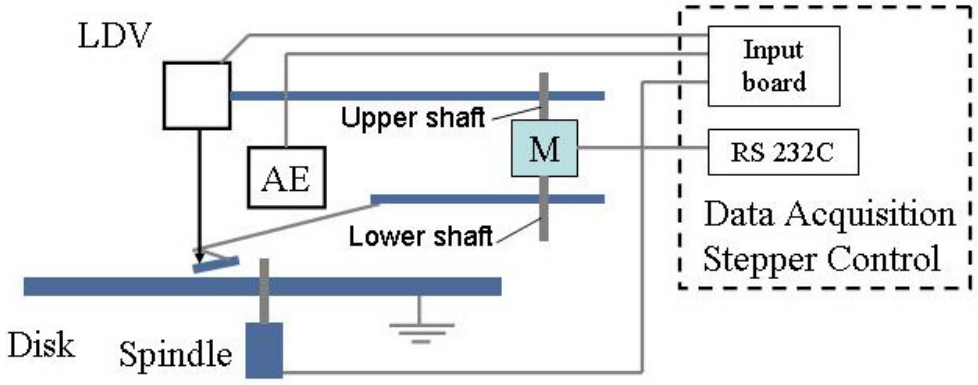

Figure 3.1: Experimental setup

sion. A laser Doppler vibrometer was used to measure slider displacement. The stepper motor was controlled via the serial port of a data acquisition computer. MATLAB® was used for data acquisition and processing and for the control of the stepper motor.

3.3 Experimental Results

Figure 3.2a shows a polar plot of the disk topography using a laser Doppler vibrometer. Two well defined regions of high disk displacement are observed, corresponding to two radial scratches on the disk surface. Figure 3.2b shows a polar plot of the slider displacement. One can observe that large vibration amplitudes of the slider are exited by the two scratches. The displacement of the slider was determined at radial positions for which the disk displacement was measured previously. Thus, the difference in the two displacement signals corresponds to the

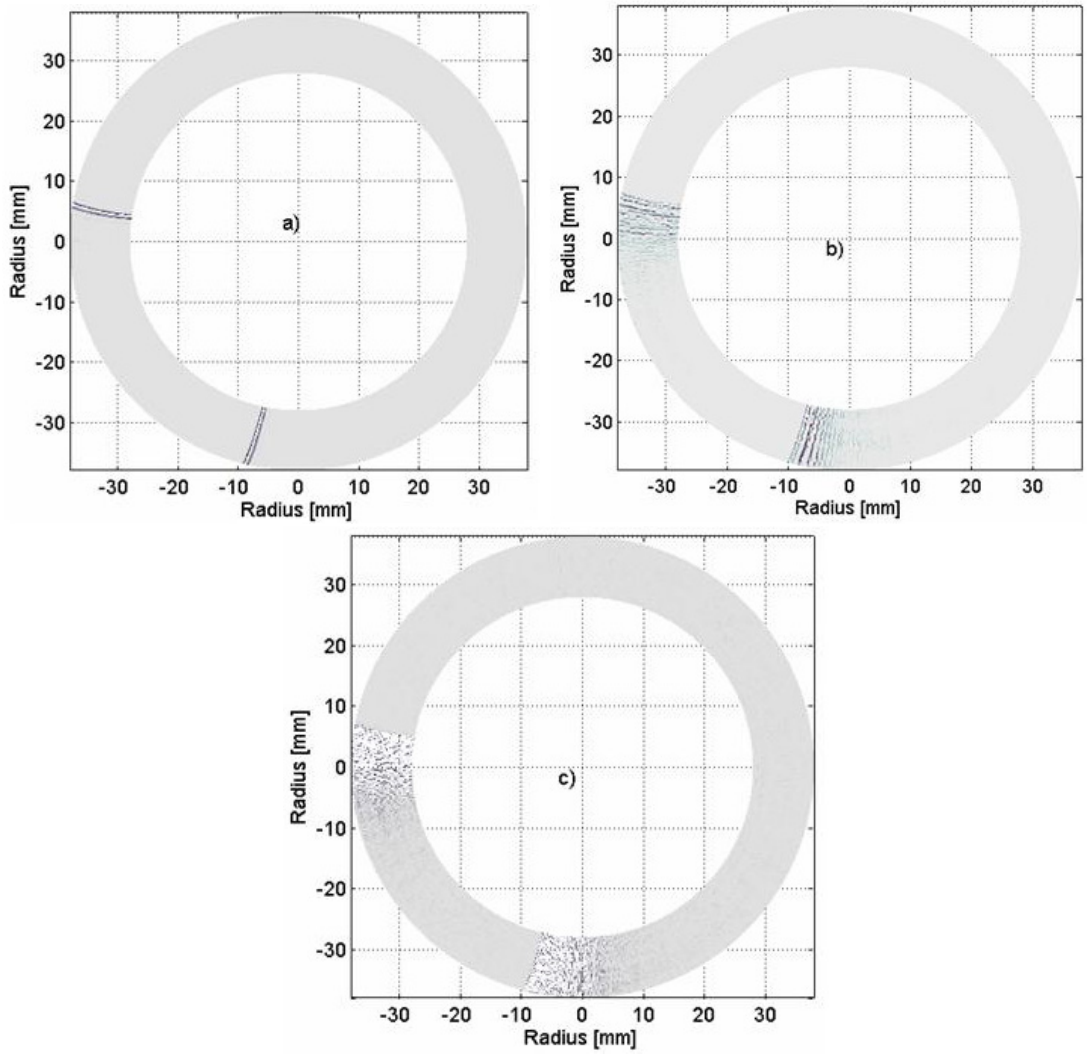

Figure 3.2: Polar plots: a) displacement of disk, b) displacement of slider, c) acoustic emission

flying height modulation of the slider. Figure 3.2c shows a polar plot of the acoustic emission signal of the disk with the slider present. One can observe a strong acoustic emission signal at the position of the scratches.

Figure 3.3a and 3.3b show acoustic emission maps for a head/disk interface with

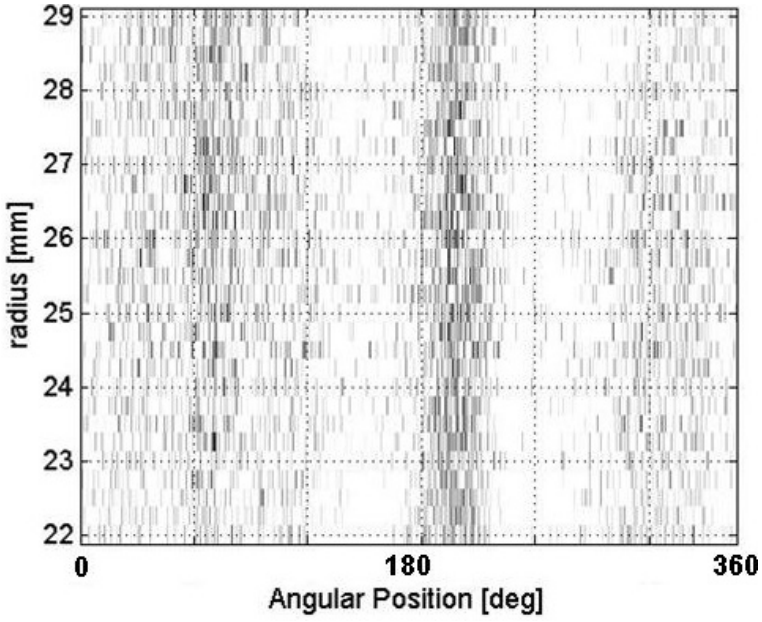

(a)

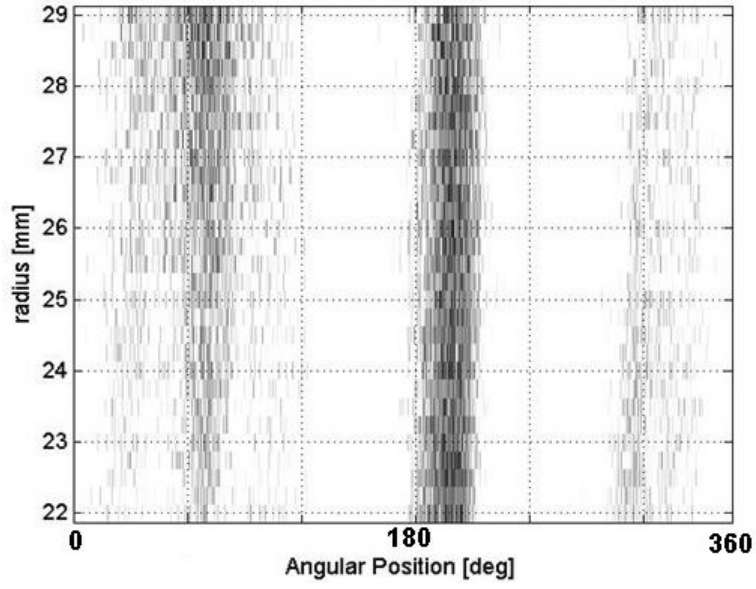

(b)

Figure 3.3: Acoustic emission map without (a) and with (b) write current applied and without thermal pole tip protrusion. The acoustic emission signal is plotted for a single revolution for a number of disk radii versus the angular position on the disk, i.e., from 0° to 360°. A new disk without scratches was used. In Figure 3.3a

a variation in the acoustic emission signal is observed for all radii at an angular position of approximately 80° and 180°. This increase in the acoustic emission signal appears to be related to a variation in roughness, microwaviness, or lubricant thickness of the disk. No write current was applied during the acoustic emission measurement in Figure 3.3a. Figure 3.3b was obtained by using the same slider and disk but with a write current applied during the entire mapping process. Auxiliary measurements have shown that the write current that was used causes a pole tip protrusion of approximately $1nm$, i.e., pole tip protrusion reduces the minimum head/disk spacing. The reduction in minimum spacing results in the increase of the acoustic emission signal at the angular positions 80° and 180°, i.e., increased pole tip protrusion increases the acoustic emission activity at the head/disk interface.

3.4 Summary

A scanning technique was introduced that allows the investigation of roughness, microwaviness and lubricant variation on slider dynamics. The method was tested using a disk with a radial scratch. AE maps were obtained, showing the potential of the method for investigation of roughness, microwaviness or lubricant variation on the disk surface.

3.5 Acknowledgement

This chapter is a partial reprint of material as it appears in: "***A Scanning Method to Study the Influence of Roughness, Microwaviness, and Lubricant Thickness Variation on Slider Dynamics***", by Maik Duwensee, Bernhard Knigge, Peter Baumgart, and Frank E. Talke, World Tribology Congress III. September 12-16, 2005, Washington, D.C. USA. The dissertation author was the primary researcher and author and the co-authors listed in this publication directed and supervised the research which forms the basis for this chapter.

Bibliography

[1] Deoras, S. and Talke, F. *Time-Frequency Analysis of Slider Dynamics and the Effect of Lubricant.* ASME J. Trib., 126:559–564, 2004.

[2] Feng, Z., Cha, E., and X., Z. *A Study of Electrical Charge at Head/Disk Interface.* In *Proc. 2004 STLE/ASME Joint Int. Tribology Conference, Long Beach*, pages 1–4. 2004.

[3] Karis, T. *Chemistry of Magnetic Recording Disk Surfaces with Intermittent Asperity Contacts.* IEEE Trans. Magn., 37(2):924, 2001.

[4] Schnur, D., Song, D., Hipwell, R., Boutaghou, Z., and Weinstein, R. *Electrical Breakdown in Electrostatic Fly Control.* In *Proc. 2003 STLE/ASME Joint Int. Tribology Conference, Ponte Vedra Beach*, pages 103–108. 2003.

[5] The MathWorks, Inc. *Matlab: Creating Graphical User Interfaces, User Manual.*

[6] The MathWorks, Inc. *Matlab: Data Acquisition Toolbox 2, User's Guide.*

[7] The MathWorks, Inc. *Matlab: Data Analysis, User Manual.*

[8] The MathWorks, Inc. *Matlab: Graphics, User Manual.*

[9] The MathWorks, Inc. *Matlab: Instrument Control Toolbox 2, User's Guide.*

[10] Thornton, B., Bogy, D., and Bhatia, C. *The Effects of Disk Morphology on Flying-Height Modulation: Experiment and Simulation.* IEEE Trans. Magn., 38(1):107–111, 2002.

[11] Zeng, Q., Thornton, B., Bogy, D., and Bhatia, C. *Flyability and Flying Height Modulation Measurement of Sliders with Sub-10nm Flying Height.* IEEE Trans. Magn., 37(2):894–899, 2001.

4

Hydrodynamic Lubrication of the Head/Disk Interface

Whenever two surfaces in relative motion have to be kept separated at very close distances, hydrodynamic lubrication is used to reduce friction and wear. Hydrodynamic lubrication has a variety of applications that are part of our daily life. It can be found in car engines to minimize friction in the bearings of crank- and camshaft. The shafts in turbine air plane engines are hydrodynamically lubricated. The slider in computer hard disk drives is carried by an air bearing based on the theory of hydrodynamic lubrication.

In 1886 Sir Osborne Reynolds [29] published a paper entitled "*On the Theory of Lubrication and Its Applications to Mr. Beauchamp Tower's Experiments Includ-*

ing an Experimental Determination of the Viscosity of Olive Oil". In the paper he developed a single differential equation relating pressure, surface velocities, and film thickness [6]. This equation became the governing equation in hydrodynamic lubrication theory. It was named after Sir Reynolds.

This chapter outlines the derivation of the compressible Reynolds equation for application in self acting slider bearings in computer hard disk drives. A finite element solution of the Reynolds equation will be presented. The finite element solution is used for air bearing simulations of discrete track head/disk interfaces presented in chapter 5.

4.1 The Reynolds Equation

For the description of the flow in pivoted slider bearings in computer hard disk drives the compressible Reynolds equation is commonly used. It is derived in this section. First, the Reynolds equation without rarefaction correction terms is derived. In the next section rarefaction effects will be introduced and incorporated in the Reynolds equation.

The derivation of the compressible Reynolds equation in this thesis is based on the following assumptions:

- the fluid is a Newtonian fluid [20]

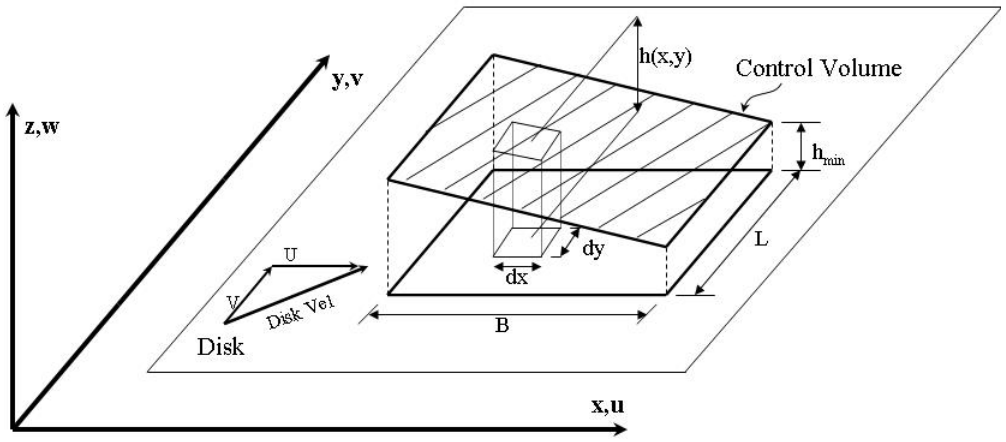

Figure 4.1: Control volume in pivoted slider bearing (after [32])

- the fluid flow is assumed to be laminar
- the flow is viscous with constant viscosity
- the gas is considered to be an ideal gas
- inertia effects can be neglected

An inclined slider bearing is shown in Figure 4.1. Here, B is the length of the slider, L is the slider width, U and V are the velocity components of the disk in the x and y direction, respectively, $h(x, y)$ represents the spacing between slider and disk as a function of x and y, and h_{min} is the minimum spacing. The velocity components of the gas flow in the x, y, and z directions are denoted by u, v, and w, respectively. Additionally, a control volume is depicted in Figure 4.1.

The conservation of mass and momentum in the control volume require that

the net mass influx and the net momentum influx across the surface area A equal the rate of change of density and momentum within the volume V, respectively. The conservation of mass can be written

$$\iint_A \rho u_j \, n_j \, dA + \iiint_V \frac{\partial \rho}{\partial t} \, dV = 0, \tag{4.1}$$

where ρ is the density of the medium and t represents time. The conservation of momentum can be written

$$\iint_A \rho u_i \, u_j \, n_j \, dA + \iiint_V \frac{\partial}{\partial t}(\rho u_i) \, dV = \iint_A \tau_{ij} n_j \, dA, \tag{4.2}$$

where τ_{ij} is the stress tensor. Applying the divergence theorem to equations 4.1 and 4.2 and realizing that the integrand is independent of the control volume, we obtain

$$\frac{\partial}{\partial x_j}(\rho u_j) + \frac{\partial \rho}{\partial t} = 0 \tag{4.3}$$

for the conservation of mass, and

$$\rho u_j \frac{\partial u_i}{\partial x_j} + \rho \frac{\partial u_i}{\partial t} = \frac{\partial \tau_{ij}}{\partial x_j} \tag{4.4}$$

for the conservation of momentum, respectively.

An isotropic, Newtonian constitutive law for the fluid is assumed, i.e., the stress tensor τ_{ij} due to the traction forces can be written as

$$\tau_{ij} = \left(-p - \frac{2}{3}\mu \frac{\partial u_k}{\partial x_k} \right) \delta_{ij} + \mu \left(\frac{\partial u_i}{\partial x_j} + \frac{\partial u_j}{\partial x_i} \right), \tag{4.5}$$

where δ_{ij} is the Kronecker delta.

To determine the relevant terms in equation 4.4 for the lubrication problem on hand, an order-of-magnitude analysis is performed. The order of-magnitude analysis is outlined in appendix C.1 of this thesis. As a result, this analysis reveals the fundamental principle in lubrication theory. This principle states that the pressure forces equal the viscous forces. For the x and y direction one obtains

$$\frac{\partial p}{\partial x} = \frac{\partial}{\partial z}\left(\mu \frac{\partial u}{\partial z}\right), \tag{4.6}$$

and

$$\frac{\partial p}{\partial y} = \frac{\partial}{\partial z}\left(\mu \frac{\partial v}{\partial z}\right), \tag{4.7}$$

respectively. The pressure gradient in the z direction is found to be zero.

$$\frac{\partial p}{\partial z} = 0. \tag{4.8}$$

After integrating 4.6 and 4.7 twice with respect to z and applying no-slip boundary conditions

$$\begin{aligned} z = 0: &\quad u = U \quad v = V \\ z = h: &\quad u = 0 \quad\ \ v = 0, \end{aligned} \tag{4.9}$$

one obtains

$$u = \frac{1}{2\mu}\frac{\partial p}{\partial x}\left(z^2 - zh\right) + U\left(1 - \frac{z}{h}\right), \tag{4.10}$$

$$v = \frac{1}{2\mu}\frac{\partial p}{\partial y}\left(z^2 - zh\right) + V\left(1 - \frac{z}{h}\right). \tag{4.11}$$

To satisfy the continuity of mass for a differential fluid element (Figure 4.1) the

continuity equation for a compressible fluid is invoked, i.e.,

$$\frac{\partial \rho}{\partial t} + \frac{\partial}{\partial x}(\rho u) + \frac{\partial}{\partial y}(\rho v) + \frac{\partial}{\partial z}(\rho w) = 0. \tag{4.12}$$

The fluid is considered to be an ideal gas, i.e.,

$$p = \rho RT = \rho \text{ const.} \tag{4.13}$$

Substituting the velocity profiles 4.10 and 4.11 and equation 4.13 into equation 4.12 and integrating one obtains

$$\frac{\partial}{\partial x}\left(ph^3\frac{\partial p}{\partial x}\right) + \frac{\partial}{\partial y}\left(ph^3\frac{\partial p}{\partial y}\right) = 6\mu\left(U\frac{\partial ph}{\partial x} + V\frac{\partial ph}{\partial y}\right) + 12\mu\frac{\partial ph}{\partial t}. \tag{4.14}$$

The integration process requires the application of the Leibniz rule and is outlined in appendix C.2.

Equation 4.14 is the two dimensional Reynolds equation for compressible gases. On the left hand side are the diffusion terms. These terms are derived from the pressure driven Poiseuille flow. The velocity dependent terms on the right hand side of equation 4.14 are the convective terms derived from the Couette flow. In steady state simulations the time dependent term can be neglected. This term is often referred to as the squeeze term.

It is sometimes advantageous to non-dimensionalize equation 4.14. Introducing the non-dimensional parameters $\tilde{x} = x/B,\ \tilde{y} = y/L,\ \tilde{p} = p/p_a,\ \tilde{u} = u/U,$ and $\tilde{v} = v/V$, where p_a is the atmospheric pressure, the non-dimensional form of the Reynolds

equation can be written as

$$\frac{\partial}{\partial \tilde{x}}\left(\tilde{p}\tilde{h}^3\frac{\partial \tilde{p}}{\partial \tilde{x}}\right)+\frac{\partial}{\partial \tilde{y}}\left(\tilde{p}\tilde{h}^3\frac{\partial \tilde{p}}{\partial \tilde{y}}\right)=\Lambda\frac{\partial \tilde{p}\tilde{h}}{\partial \tilde{x}}+\Lambda\frac{V}{U}\frac{\partial \tilde{p}\tilde{h}}{\partial \tilde{y}}+\sigma\frac{\partial \tilde{p}\tilde{h}}{\partial t}, \tag{4.15}$$

where Λ is the bearing number and σ is the squeeze number. The bearing number

$$\Lambda=\frac{6\mu UB}{p_a h_{min}^2}, \tag{4.16}$$

determines the magnitude of the velocity driven terms in the Reynolds equation 4.15. The squeeze number

$$\sigma=\frac{12\mu\omega B^2}{p_a h_{min}^2}. \tag{4.17}$$

determines the magnitude of the time dependent term in equation 4.15.

The Reynolds equation is a second order partial differential equation relating pressure, spacing, density, surface velocities and fluid viscosity in a bearing. If the spacing function $h(x, y)$ is given, the bearing pressure can be calculated using the Reynolds equation. However, closed form solutions for the Reynolds equation exist only for limiting cases and simple geometries. As outlined in chapter 1, modern slider designs incorporate complex shaped air bearing surfaces to ensure a stable flying at ultra-low spacing. In patterned media technologies the air bearing domain is even more complex, due to the spacing variations as a function of disk pattern. For these complicated air bearing geometries, numerical approximations have to be applied for the solution of the Reynolds equation. In general, finite differences, finite elements, or boundary integral methods are used. In this thesis a finite

element approach is used for air bearing simulations of discrete track head/disk interfaces. The finite element solution for the Reynolds equation used in this thesis is outlined in section 4.3. As was outlined in chapter 1, the minimum spacing between slider and disk in current computer hard disk drives is on the order of $7nm$. For such low spacings the assumption of no-slip boundary conditions breaks down and slip flow correction terms have to be incorporated in the Reynolds equation. The next section outlines different slip flow correction terms and introduces them into the Reynolds equation.

4.2 Slip Flow Correction for Low Spacing

For the derivation of the Reynolds equation (equation 4.14 in the preceding section 4.1) no-slip boundary conditions were applied at the disk and slider surfaces. Maxwell (1867) [28] was the first to observe the so-called velocity slip at the interface of a solid wall and gas. He predicted a slip at the boundary based on investigations on stresses in rarefied gases arising from inequalities of temperature. The no-slip boundary condition applied in the last section is valid only if the gas close to the surface is in thermodynamic equilibrium. Thermodynamic equilibrium requires a very high molecule-surface collision frequency [3, 8, 30]. The assumption of no-slip at the boundary is generally applied for fluid problems where the typical dimension in the flow regime is much larger than the mean free path λ in the flow.

However, when the typical dimension in the flow regime becomes comparable to the mean free path, the no-slip boundary condition is not longer valid and so-called slip flow boundary conditions have to be applied, i.e., rarefaction effects have to be included.

To quantify the degree of rarefaction, the Knudsen number Kn is generally used. The Knudsen number is defined as

$$Kn = \frac{\lambda}{h}, \tag{4.18}$$

where λ is the mean free path and h is the fluid film thickness. In the description of flow phenomena of the head/disk interface of computer hard disk drives, the minimum spacing $h = h_{min}$ is generally used to define the Knudsen number of the flow.

Three types of slip flow corrections have been suggested and used for the simulation of rarefied gas flow of head/disk interfaces. The first approximation was introduced by Burgdorfer [4] in 1959. He suggested to replace the no-slip velocity boundary condition (equation 4.9 in section 4.1) with

$$\begin{aligned} u(0) &= U + \frac{2-\alpha}{\alpha}\lambda_a \left.\frac{\partial u}{\partial y}\right|_{z=0}, \\ u(h) &= -\frac{2-\alpha}{\alpha}\lambda_a \left.\frac{\partial u}{\partial y}\right|_{z=h} \end{aligned} \tag{4.19}$$

at the disk and slider surface, respectively. The parameter λ_a is the mean free path of air at atmospheric pressure. The parameter α in equation 4.19 is called surface

accommodation or reflection coefficient. The surface accommodation coefficient is a measure for the amount of energy transfer between a molecule and a surface. A surface accommodation coefficient of $\alpha = 1$ refers to a so called "fully accommodating" wall [23]. The particles energy is fully thermalized at the surface [3, 8, 30]. The surface accommodation coefficient also represents the amount of particles that reflect diffusively with a surface. For the case $\alpha = 1$ all molecules are reflected diffusively. The first order slip flow correction model is a good model as long as the minimum spacing is not smaller than approximately $100nm$. For lower spacing, Hsia et al. (1983) [22] suggested a second order slip flow model. For the second order slip flow model, the boundary conditions are

$$\begin{aligned} u(0) &= U + \frac{2-\alpha}{\alpha}\left[\lambda_a \frac{\partial u}{\partial y}\bigg|_{z=0} - \frac{\lambda_a^2}{2}\frac{\partial^2 u}{\partial y^2}\bigg|_{z=0}\right], \\ u(h) &= \frac{2-\alpha}{\alpha}\left[-\lambda_a \frac{\partial u}{\partial y}\bigg|_{z=h} - \frac{\lambda_a^2}{2}\frac{\partial^2 u}{\partial^2}\bigg|_{z=h}\right] \end{aligned} \tag{4.20}$$

at the disk surface and slider surface, respectively.

For extremely low spacings in today's hard disk drives the Knudsen number is greater than 1. Flow phenomena for these large Knudsen numbers are best modeled by the Boltzmann equation of kinetic gas theory [3]. Gans [17] was first to derive a lubrication equation based on a linearized Boltzmann equation. Fukui and Kaneko [14, 15] presented a generalized Reynolds equation that could be used for first and second order slip flow corrections as well as for Boltzmann correction.

They presented a modified Reynolds equation

$$\frac{\partial}{\partial x}\left(\overline{Q}(Kn)ph^3\frac{\partial p}{\partial x}\right)+\frac{\partial}{\partial y}\left(\overline{Q}(Kn)ph^3\frac{\partial p}{\partial y}\right)=6\mu\left(U\frac{\partial ph}{\partial x}+V\frac{\partial ph}{\partial y}\right)+12\mu\frac{\partial ph}{\partial t}, \tag{4.21}$$

where $\overline{Q}(Kn)$ is a so-called correction factor. In vector notation equation 4.21 can be written as

$$\nabla\cdot(\overline{Q}ph^3\nabla p)=6\mu\boldsymbol{V}\cdot\nabla(ph)+12\mu\frac{\partial}{\partial t}(ph) \tag{4.22}$$

The correction factor $\overline{Q}$ is a function of the local Knudsen number Kn and assumes different values for the three slip-flow correction models. Fukui and Kaneko proposed to approximate the correction factor $\overline{Q}$ with three different polynomials. The polynomials were chosen based on the value of the inverse Knudsen number [16]. Hwang et al. [26] proposed a single equation for $\overline{Q}$ valid in the Knudsen number range $0.009 < Kn < 900$. This approximation is used for the air bearing simulations presented in chapter 5. Based on Hwang [26] the correction factor $\overline{Q}$ can be written as

$$\overline{Q}_{first}=1+6Kn, \tag{4.23}$$

for first order slip correction,

$$\overline{Q}_{second}=1+6Kn+6Kn^2 \tag{4.24}$$

for second order slip correction, and

$$\overline{Q}_{Boltzmann}=1+0.10842Kn+\frac{9.3593}{Kn^{-1.17468}}. \tag{4.25}$$

for Boltzmann correction, respectively. The local Knudsen number is a function of the local mean free path, which depends on the pressure and can be calculated by

$$Kn = \frac{\lambda}{h} = \frac{\lambda_a p_a}{hp}, \tag{4.26}$$

where p_a is the atmospheric pressure.

The derivation of the Reynolds equation in the preceding section required the gas to be ideal. This assumption was used to replace the density ρ with the pressure p in the derivation process. As the spacing decreases the flow becomes more rarefied and a value for the density ρ cannot be easily defined, leading to conceptual difficulties in the derivation process outlined in the previous section. However, Alexander et al. [1] and Huang et al. [24] compared air bearing simulation results based on equation 4.21 with simulation results based on the direct simulation Monte Carlo (DSMC) method and found excellent agreement. The direct simulation Monte Carlo method is a particle based simulation method used for the simulation of rarefied gas flow. Alexander et al. [1] applied the method to check the validity of the modified Reynolds equation for high Knudsen number flow in "smooth" head/disk interfaces. Their results were based on a two dimensional model. Huang et al. [24] extended the method presented in [1] to three dimensions. The DSMC method is introduced in chapter 6 of this thesis.

4.3 The Finite Element Formulation of the Reynolds Equation

The Reynolds equation 4.14, 4.21, or 4.22 is a second order non-linear partial differential equation. The Reynolds equation allows the calculation of the pressure distribution in the bearing as a function of a given spacing. Even for very simple cases this calculation is difficult to perform. Numerical approaches have to be used. Here, a finite element formulation of the Reynolds equation is presented based on earlier work by Wahl [32] and Duwensee [11]. The so-called "CMRR" air bearing simulator is based upon this formulation.

The basic idea of the finite element approach is to satisfy a given differential equation in a global sense rather than at each point. The investigated domain is divided into a finite number of smaller elements. For these elements the field variables of the differential equation are approximated through so-called shape functions. Polynomials are often chosen for this approach.

A commonly used formulation in finite element analysis is Galerkin's so-called "weighted residual approach". Here, a residual is minimized over the entire domain to satisfy the differential equation in a global sense. This is accomplished by introducing a weight function W. The weighted residual formulation of the Reynolds equation is obtained by first multiplying equation 4.22 with the weight

function W and then integrating the equation. The weighted residual form of the Reynolds equation can be written

$$\iint_{\Omega} \left\{ \nabla \cdot \left(\overline{Q} p h^3 \nabla p \right) - 6\mu \mathbf{V} \cdot \nabla \left(ph \right) - 12\mu \frac{\partial}{\partial t} \left(ph \right) \right\} W d\Omega = 0, \tag{4.27}$$

where W is the weight function and Ω denotes the domain. Equation 4.27 is difficult to handle and additional manipulations are necessary before a numerical solution can be obtained. First, the product rule of differentiation

$$(\nabla \cdot \mathbf{U})\mathbf{W} = \nabla \cdot (\mathbf{W}\mathbf{U}) - \nabla \mathbf{W} \cdot \mathbf{U} \tag{4.28}$$

is applied to the first term of equation 4.27. This yields, after substituting in equation 4.27,

$$\begin{aligned} \iint_{\Omega} \{ & \nabla \cdot \left(\overline{Q} p h^3 \nabla p W \right) - \left(\overline{Q} p h^3 \nabla p \right) \cdot \nabla W \\ & - 6\mu \mathbf{V} \cdot \nabla (ph) W - 12\mu \frac{\partial}{\partial t} \left(ph \right) W \Big\} d\Omega = 0. \end{aligned} \tag{4.29}$$

Applying the divergence theorem

$$\iint_{\Omega} \nabla \cdot \mathbf{U} d\Omega = \oint_{\sigma} \mathbf{U}\mathbf{n} d\sigma \tag{4.30}$$

to the first term of equation 4.29, where $\mathbf{n}$ is the outward normal vector of the surface Ω, one obtains

$$\begin{aligned} \oint_{\sigma} \left(\overline{Q} p h^3 \nabla p W \right) \mathbf{n} d\sigma + \iint_{\Omega} \{ & - \left(\overline{Q} p h^3 \nabla p \right) \nabla W \\ & - 6\mu \mathbf{V} \cdot \nabla (ph) W - 12\mu \frac{\partial}{\partial t} \left(ph \right) W \Big\} d\Omega = 0. \end{aligned} \tag{4.31}$$

The weight functions can be chosen arbitrary. At the boundary the pressure is known and equals ambient pressure. By choosing the weight function to be zero at the boundary, the first integral vanishes and the final weighted residual formulation is obtained as

$$\iint_{\Omega} \left\{ -\left(\overline{Q} p h^3 \nabla p\right) \nabla W - 6\mu \mathbf{V} \cdot \nabla (ph) W - 12\mu \frac{\partial}{\partial t} (ph)\, W \right\} d\Omega = 0. \tag{4.32}$$

For steady state problems the time dependent term in equation 4.32 can be neglected and the problem reduces to

$$\iint_{\Omega} \left\{ -\left(\overline{Q} p h^3 \nabla p\right) \nabla W - 6\mu \mathbf{V} \cdot \nabla (ph) W \right\} d\Omega = 0. \tag{4.33}$$

Equation 4.33 represents the finite element formulation of the steady state Reynolds equation. It contains nonlinear expressions for the pressure p. In order to linearize these terms the pressure is approximated by a Taylor series expansion around p_0. Neglecting higher order terms, the pressure p can be written as

$$p \approx p_0 + dp, \tag{4.34}$$

where p_0 is an initial guess for the pressure. Equation 4.34 requires that the pressure p is close to p_0, i.e., dp is small. To linearize the term $p\nabla p$ in equation 4.33, equation 4.34 is used. The term $p\nabla p$ can be written

$$p\nabla p = (p_0 + dp)\nabla(p_0 + dp) = p_0 \nabla p_0 + p_0 \nabla(dp) + dp \nabla p_0 + dp \nabla(dp). \tag{4.35}$$

Equation 4.35 contains a term $dp\nabla(dp)$. This term is of higher order in dp and

can be neglected. The term $\nabla(ph)$ of equation 4.33 becomes

$$\nabla(ph) = \nabla\left\{(p_0 + dp)h\right\} = p_0\nabla h + h\nabla p_0 + h\nabla(dp) + dp\nabla h. \tag{4.36}$$

After inserting equation 4.34 - 4.36 in the finite element formulation equation 4.33 and reordering one obtains

$$\iint\limits_{\Omega} \left\{\overline{Q}h^3(dp\nabla p_0 + p_0\nabla dp)\cdot\nabla W + 6\mu\mathbf{V}\cdot(h\nabla dp + dp\nabla h)W\right\} d\Omega = \\ -\iint\limits_{\Omega} \left\{\overline{Q}h^3 p_0\nabla p_0\cdot\nabla W + 6\mu\mathbf{V}\cdot(h\nabla p_0 + p_0\nabla h)W\right\} d\Omega. \tag{4.37}$$

If one considers the pressure p_0 as an initial guess or as the result from a previous iteration step, equation 4.37 can be considered as an iteration scheme where $p = p_0 + dp$ yields the pressure for the new iteration. Equation 4.37 is arranged in such a way that the right hand side contains terms only dependent on p_0, which is known from the previous iteration step. The left hand side contains only linear terms of the unknown quantity dp.

Since it is difficult to define a single function for W or p over the entire domain, the domain has to be discretized into smaller elements. Figure 4.2 depicts the discretization process. The integration over the domain is then replaced by the sum over all elements. It is convenient to transform the elements into an isoparametric space, as depicted in Figure 4.3. The element shapes can then be chosen arbitrarily in the physical space. In the isoparametric space the elements have a regular shape. This concept allows a good approximation of the geometry. Furthermore,

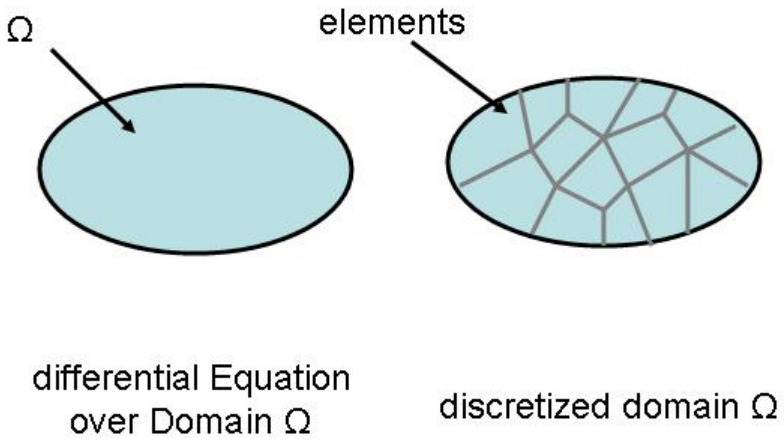

Figure 4.2: Schematic of domain discretization

the regular space in the isoparametric space is convenient for numerical integration of equation 4.37. Different types of elements can be implemented in a finite element program. For each element type an element equation

$$[\boldsymbol{k}]^e\{\boldsymbol{dp}\}^e = \{\boldsymbol{r}\}^e \tag{4.38}$$

can be found. In equation 4.38 "e" denotes that the equation is valid for the element level. The matrix $[\boldsymbol{k}]^e$ in equation 4.38 is the so-called stiffness matrix, $\{\boldsymbol{r}\}^e$ denotes the right right hand side vector, and $\{\boldsymbol{dp}\}^e$ is the vector of the unknown. The elements of the stiffness matrix depend on the finite element formulation used. For the simulator developed in the Center for Magnetic Recording Research (CMRR), bilinear quadrilateral elements are used. In addition, linear triangular elements have been implemented. The elements of the stiffness matrix are described in

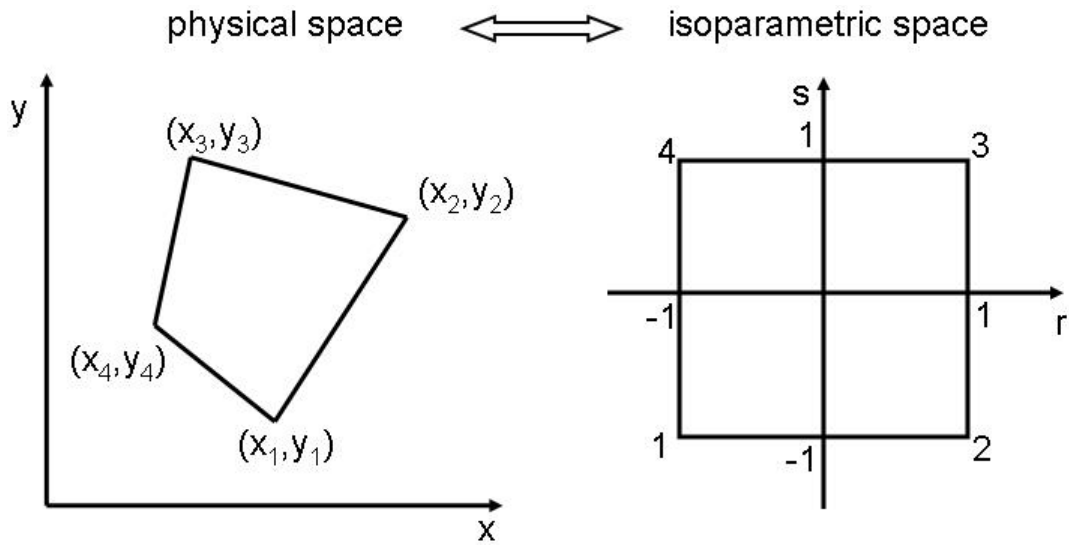

Figure 4.3: Illustration of transformation between physical and isoparametric space

appendix C.3. All element stiffness matrices and right hand side vectors must be incorporated into the global simulation problem. This process is called "assembly" in finite element analysis. After assembly of all elements, the global equation can be written

$$[\mathbf{K}] \cdot \{\mathbf{dp}\} = \{\mathbf{r}\}\,. \tag{4.39}$$

Equation 4.39 has to be solved at each iteration step. Whenever the change in the pressure is less than a pre-determined value, one can assume that the solution is obtained. In equation 4.39 the matrix $\boldsymbol{K}$ has the dimension $n \times n$, where n is the number of finite element nodes of the simulation model. To save computer memory, a sparse matrix scheme and an iterative solver rather than a Gaussian solver were implemented [31].

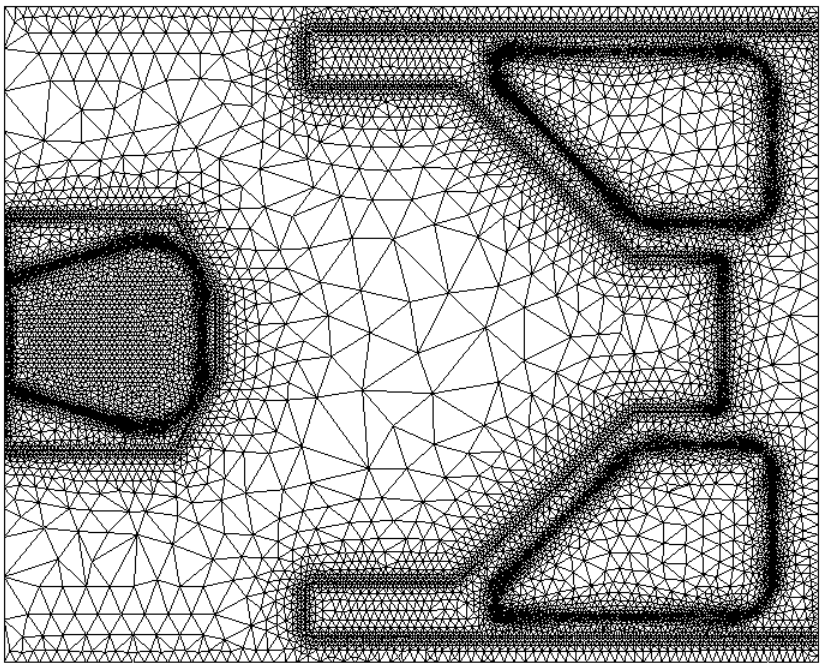

Figure 4.4: Typical finite element mesh for an air bearing surface

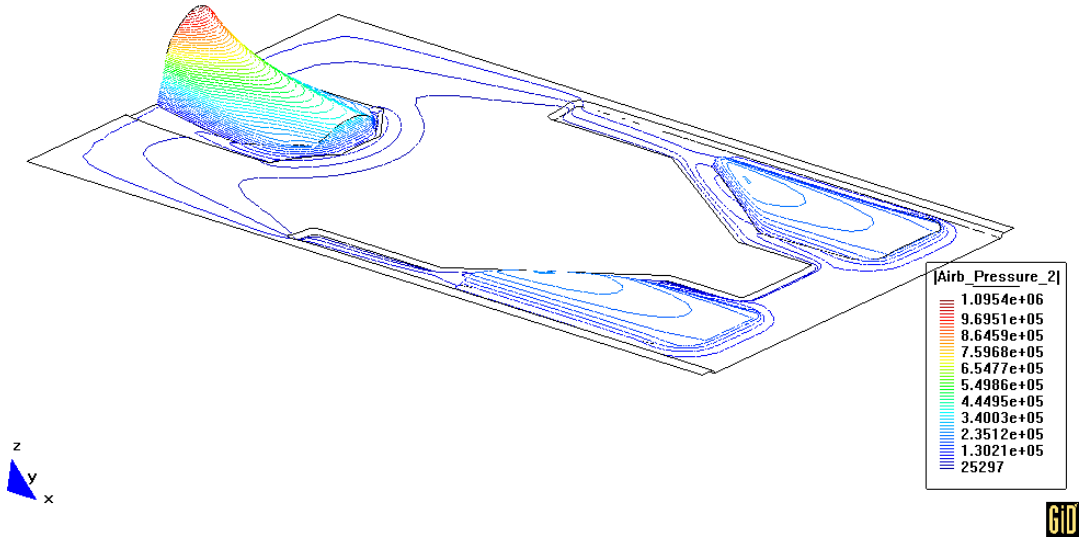

Figure 4.5: Typical air bearing pressure distribution

For the discretization, a finite element mesh generation program is used. The CMRR air bearing simulator uses the *GiD*-program [9, 10] for pre- and post processing. The *GiD*-program is freely customizable [11]. A typical finite element mesh is shown in Figure 4.4. The number of elements in a finite element model depends on the size of the smallest feature in the geometry approximated by the finite element mesh. For a typical head/disk interface simulation the number of elements is on the order of $30,000$ to $80,000$ elements. Air bearing simulations for patterned media head/disk interfaces (chapter 5) require a much finer discretization resulting in models with up to 100 million elements or more [12, 13]. Figure 4.5 shows a typical pressure distribution for a head/disk interface. As can be seen, the maximum pressure occurs at the trailing edge region of the air bearing. In this region the spacing is the smallest. A small spacing results in high air bearing pressure. The pressure distribution in discrete track recording head/disk interfaces is far more complex (chapter 5).

The pressure distribution obtained from a finite element solution of the Reynolds equation depends on the spacing in the bearing. In air bearing simulations of head/disk interfaces the spacing is often an unknown quantity as well. The following section describes a set of equations that affect the spacing between slider and disk in a computer hard disk drive. These equation are referred to as slider equilibrium equations.

4.4 Slider Equilibrium Equations

In the previous sections the Reynolds equation was derived and a finite element solution of the Reynolds equation was presented. It was pointed out that the Reynolds equation allows the calculation of the pressure field of the air bearing as a function of a given spacing between slider and disk. The spacing between slider and disk is generally unknown and depends on several parameters. Some of the parameters are the disk velocity, the radial position of the slider and the dimensions of the air bearing surface.

The slider is attached to a so-called gimbal. The point of attachment is referred to as the pivot point of the slider. The gimbal is formed by a very thin sheet of steel. The gimbal is attached to the suspension. The gimbal constraints three of the six degrees of the slider. Figure 4.6 shows a schematic of a mounted slider. The three remaining degrees of freedom of the slider are the motion in the vertical direction (z-direction), the pitch angle α and the roll angle β. The pitch and roll angles are measured with respect to the pivot point. The design and material properties of the gimbal are chosen in such a way that each degree of freedom of the slider is related to a certain spring stiffness. As shown in Figure 4.6, the stiffness in the vertical direction is referred to as k_z. The values for the stiffness in the pitch and roll directions are k_α and k_β, respectively.

In air bearing simulations of head/disk interfaces of computer hard drives it is

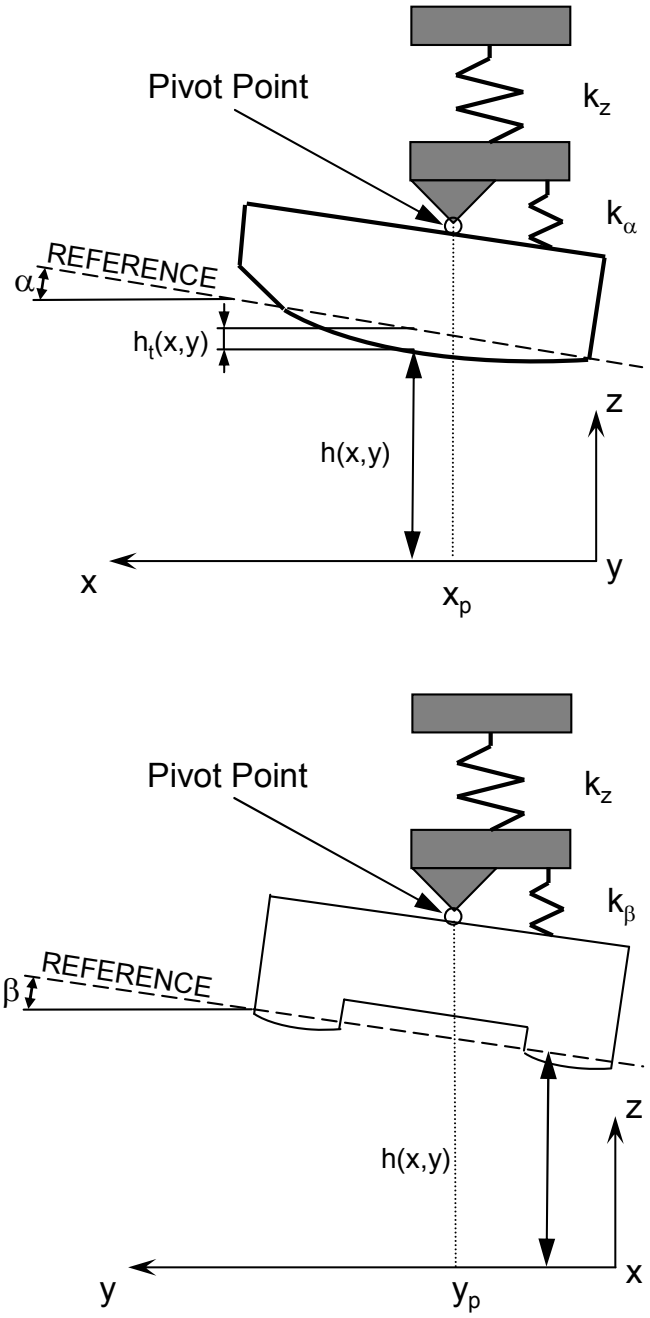

Figure 4.6: Schematic of pivoted slider bearing (after [32])

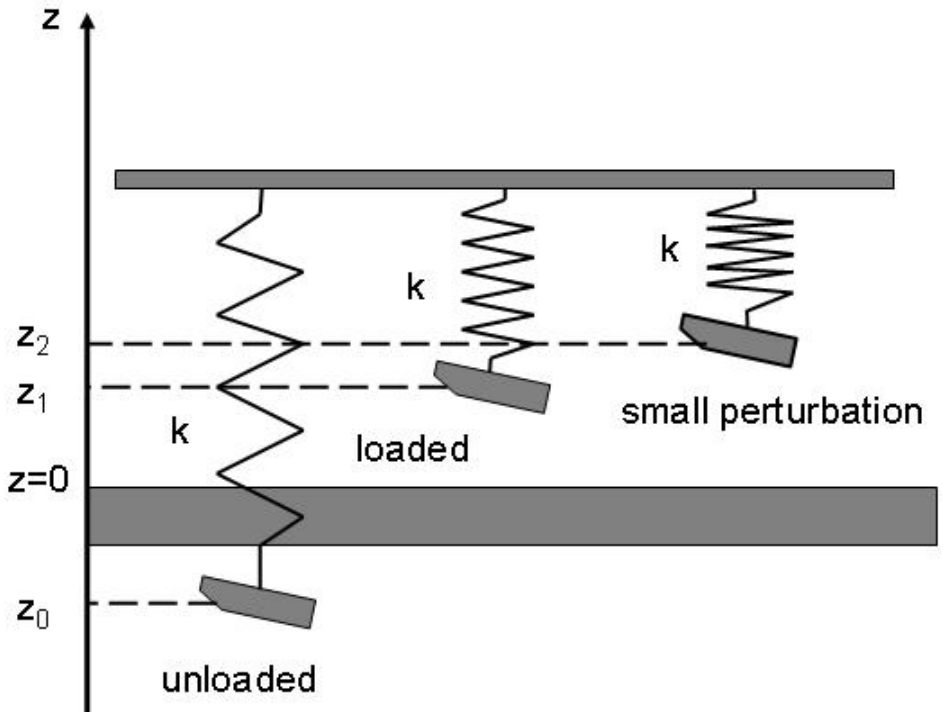

Figure 4.7: Slider equilibrium in vertical direction (after [32])

generally the goal to find the spacing between slider and disk as a function of disk speed, air bearing design or radial position of the slider. The numerical solution of the Reynolds equation presented in section 4.3 provides a pressure distribution of the slider for a given slider position relative to the disk. This position has to be balanced by the forces applied to the slider from the gimbal. Figure 4.7 can be used to explain the slider equilibrium in the $z-$direction. The spring symbolizes the vertical stiffness of the gimbal. The force created by the compression of the spring has to be equal to the force in the z-direction generated by the air bearing. Thus, the integral of the pressure distribution over the air bearing surface is equal

to the spring compression force. Sliders are generally preloaded. Considering position z_1 in Figure 4.7 as the equilibrium for the nominal slider load, the force F_{ext} for small perturbations can be written as

$$F_{ext} = F_{air} - k_z \left(z_2 - z_1\right) = F_{air} - k_z dz. \tag{4.40}$$

F_{air} is obtained by integrating the pressure over the air bearing surface.

$$F_{air} = \iint_A p(x, y)\, dA \tag{4.41}$$

The equilibrium for the pitch and roll degrees of the slider can be derived in a similar way. For these degrees of freedom the moments of the gimbal and the moments produced by the pressure distribution of the air bearing have to be in equilibrium. The equilibrium for the pitch direction can be expressed as

$$\iint_A p(x, y)(x - x_p)\, dA - M_\alpha^{ext} = k_\alpha d\alpha, \tag{4.42}$$

where x_p is the x-coordinate of the pivot point. The equilibrium for the roll direction can be written

$$\iint_A p(x, y)(x - y_p)\, dA - M_\beta^{ext} = k_\beta d\beta, \tag{4.43}$$

where y_p is the y-coordinate of the pivot point. Combining the equilibrium equa-

tions 4.41, 4.42, and 4.43 into matrix form yields

$$\begin{Bmatrix} \iint_A p(x,y)\,dA - F_z^{ext} \\ \iint_A p(x,y)(x-x_p)\,dA - M_\alpha^{ext} \\ \iint_A p(x,y)(x-y_p)\,dA - M_\beta^{ext} \end{Bmatrix} = \begin{bmatrix} k_z & 0 & 0 \\ 0 & k_\alpha & 0 \\ 0 & 0 & k_\beta \end{bmatrix} \begin{Bmatrix} dh \\ d\alpha \\ d\beta \end{Bmatrix}. \tag{4.44}$$

Equation 4.44 represents the balance between air bearing forces and external suspension forces. The equations represented by the matrix equation 4.44 are referred to as the slider equilibrium equations. In steady state air bearing simulations the slider equilibrium equations are solved simultaneously with the Reynolds equation in a way that the forces created by the air bearing balance the forces created by the deflection of the gimbal. The position that the slider attains at equilibrium is called the steady state position. Sometimes this position is referred to as slider attitude.

To satisfy the Reynolds equation and the slider equilibrium equations simultaneously, a simultaneous Newton-Raphson scheme is implemented in the CMRR air bearing simulator. This iterative scheme is often used in nonlinear engineering problems. Its implementation in the CMRR air bearing simulation program is described in appendix C.4.

The next chapter of this thesis presents results of air bearing simulations of discrete track head/disk interfaces. The simulations were performed based on the theory outlined in this chapter.

Bibliography

[1] Alexander, F., Garcia, A., and Alder, B. *Direct Simulation Monte Carlo for Thin-film Bearings*. Phys. Fluids, 6 (12):3854–3860, 1994.

[2] Bhushan, B. *Tribology and the Mechanics of Magnetic Storage Devices*. Springer, second edition, 1996.

[3] Bird, G. *Molecular Gas Dynamics and the Direct Simulation of Gas Flows*. Oxford University Press, 1994.

[4] Burgdorfer, A. *The Influence of the Mean Free Path on the Performance of Hydrodynamic Gas Lubricated Bearings*. ASME J. Basic Eng., 81:94, 1959.

[5] Burgdorfer, A. *The Influence of the Mean Free Path on the Performance of Hydrodynamic Gas Lubricated Bearings*. Trans. ASME Series D, 81:94–100, 1959.

[6] Bushan, B. *Tribology and Mechanics of Magnetic Storage Devices*. Springer, 2nd edition, 1996.

[7] Castelli, V. *Review of Numerical Methods in Gas Bearing Film Analysis*. J. of Lub. Tech., pages 777–790, 1968.

[8] Cercignani, C. *Rarefied Gas Dynamics*. Cambridge University Press, first edition, 2000.

[9] CIMNE. *CIMNE, GiD Reference Manual*, 1999.

[10] CIMNE. *GiD User Manual*, 1999.

[11] Duwensee, M. *Improvements in the Pre- and Postprocessing Software for a Finite Element Based Air Bearing Simulator and Analysis of Intermolecular Forces in the Head/Disk Interface*. Master's thesis, University of California, San Diego, 2004.

[12] Duwensee, M., Suzuki, S., Lin, J., Wachenschwanz, D., and Talke, F. *Air Bearing Simulation of Discrete Track Recording Media.* IEEE Trans. Mag., 42 (10):2489–2491, 2006.

[13] Duwensee, M., Suzuki, S., Lin, J., Wachenschwanz, D., and Talke, F. *Simulation of the Head Disk Interface for Discrete Track Media.* Microsystem Technologies, Published Online, 2006.

[14] Fukui, S. and Kaneko, R. *Analysis of Flying Characteristics of Magnetic Heads with Ultra-Thin Spacings Based on the Boltzmann Equation.* IEEE Trans. Mag., 24 (6):2751–2753, 1988.

[15] Fukui, S. and Kaneko, R. *Analysis of Ultra-Thin Gas Film Lubrication Based on Linearized Boltzmann Equation: First Report-Derivation of a Generalized Lubrication Equation Including Thermal Creep Flow.* ASME J. Trib., 110:253–262, 1988.

[16] Fukui, S. and Kaneko, R. *A Database for Interpolation of Poiseuille Flow Rates of High Knudsen Number Lubrication Problems.* ASME J. Trib., 112:78, 1990.

[17] Gans, R. *Lubrication Theory at Arbitrary Kundsen Numbers.* Trans. ASME J. Trib., 107:431–433, 1985.

[18] George, P. and Borouchaki, H. *Delaunay Triangulation and Meshing Application to Finite Elements.* Hermes, 1998.

[19] Gross, W. *A Gas Film Lubrication Study, Part I, Some Theoretical Analyses of Slider Bearings.* IBM J. Res. Develop., 3:237–255, 1959.

[20] Gross, W. *Fluid Film Lubrication.* John Wiley & Sons, 1980.

[21] Gross, W. A. *Fluid Film Lubrication.* John Wiley and Sons, 1980.

[22] Hsia, Y.-T. and Domoto, G. *An Experimental Investigation of Molecular Rarefaction Effects in Gas Lubricated Bearings at Ultra-Low Clearances.* ASME J. Lubr. Technol., 105:120–130, 1983.

[23] Huang, W. and Bogy, D. *The Effect of the Accommodation Coefficient on Slider Air Bearing Simulation.* ASME J. Trib., 122:427–435, 2000.

[24] Huang, W., Bogy, D., and Garcia, A. *Three-Dimensional Direct Simulation Monte Carlo Method for Slider Air Bearings.* Phys. Fluids, 9 (6):1764–1769, 1997.

[25] Hughes, T. *The Finite Element Method*. Prentice-Hall, INC., 1987.

[26] Hwang, C., Fung, R., R., Y., Weng, C., and Li, W. *A New Modified Reynolds Equation for Ultrathin Film Gas Lubrication*. IEEE Trans. Mag., 32(2):344–347, 1996.

[27] Lau, T. and Lo, S. *Finite Element Mesh Generation Over Analytical Curved Surfaces*. Computer & Structures, 59(2):301–309, 1996.

[28] Maxwell, J. *On Stresses in Rarefied Gases Arising from Inequalities of Temperature*. Philos. Trans. R. Soc. London, 170:231, 1867.

[29] Reynolds, O. *On the Theory of Lubrication and Its Applications to Mr. Beauchamp Tower's Experiments Including an Experimental Determination of the Viscosity of Olive Oil*. Philosoph. Trans. Roy. Soc., Series A 12:157–234, 1886.

[30] Shen, C. *Rarefied Gas Dynamics*. Springer, first edition, 2005.

[31] Stoer, J. and Bulirsch, R. *Introduction to Numerical Analysis*. Springer, 2002.

[32] Wahl, M. *Numerical and Experimental Investigation of the Head/Disk Interface*. Ph.D. thesis, University of California, San Diego, 1994.

[33] Wahl, M., Lee, P., and Talke, F. *An Efficient Finite Element-Based Air Bearing Simulator for Pivoted Slider Bearings using Bi-Conjugate Gradient Algorithms*. STLE Trib. Trans., 39 (1), 1996.

[34] Wu, L. and Bogy, D. B. *Unstructured Triangular Mesh Generating Techniques and a Finite Volume Numerical Scheme for Slider Air Bearing Simulation with Complex Shaped Rails*. IEEE Trans. Mag., 35(5):2421–2423, 1999.

[35] Zienkiewicz, O. C. and Phillips, D. V. *An Automatic Mesh Generation Scheme For Plane And Curved Surfaces By Isoparametric Co-ordinates*. Inter. J. for Numer. Methods in Eng., 3:519–528, 1971.

5

Air Bearing Simulation of Discrete Track Head/Disk Interfaces

This chapter investigates the effect of discrete tracks on the steady state flying behavior of sub-ambient proximity sliders. A finite element solution of the Reynolds equation was used to simulate the flying characteristics of sliders over a grooved disk surface. The finite element solution of the Reynolds equation used in this study was outlined in the previous chapter of this thesis.

Sliders flying over discrete track disks "see" a disk surface that consists of ridges and grooves. The air bearing pressure build-up for sliders flying over discrete track

disks is different from that for sliders flying over plane disks. Low air bearing pressure can be expected for those regions of the slider that are positioned over grooves, while high air bearing pressure exists over ridges. The air bearing characteristics are determined for several pico and femto form factor air bearing sliders flying over discrete track disks. An empirical equation is obtained describing the loss of flying height of a slider flying over discrete track disks compared to flying over smooth disks.

5.1 Introduction

Patterned media technologies are believed to allow an increase in storage density beyond $500 Gbit/in^2$ [1]. Two technologies have been explored in the patterned media area, i.e., bit patterned media (BPM) recording and discrete track recording (DTR). In bit patterned media (BPM) recording, magnetic bits are recorded on individual "island-like" regions. In discrete track recording (DTR), the magnetic information is stored on discrete tracks that are physically separated from each other.

The air bearing domain in patterned media is highly influenced by the existence of surface structures on either disk or head. "Island-like" structures or circumferential grooves on the disk surface change the air bearing pressure distribution of the head/disk interface compared to non-structured head/disk interfaces. A num-

ber of researchers have investigated the effect of local spacing variations of the air bearing as a result of roughness [7] or surface texture on the head [3, 8] and disk [4]. Weissner et al. [7] investigated numerically the effect of sinusoidal transverse and longitudinal surface roughness. Tagawa et al. [3] investigated the effect of longitudinal grooved slider surfaces on the flying behavior of a two rail slider flying over a smooth disk surface. The steady state pressure distribution of a longitudinally grooved air bearing slider flying over a smooth disk is comparable to a discrete track recording head/disk interface with grooves aligned in the circumferential direction on the disk surface and no grooves on the slider. Tagawa and Mori [4, 5] extended the work reported in [3] to patterned media. The dimensions of the surface pattern that they considered were on the order of five to twenty micrometers ($5\mu m$ to $20\mu m$) for the width and length direction and ten to forty nanometers ($10nm$ to $40nm$) for the out of plane direction, respectively. They determined the pressure distribution for two-rail positive pressure sliders and reported an increase in the flying height due to patterning. To simulate the flying behavior of sliders on patterned media, a very fine domain discretization is required, resulting in large simulation models. An alternative to very fine domain discretization was implemented by Buscaglia and Jai [2], who applied homogenization techniques to the Reynolds equation to take fine but periodic surface structures into account. They presented the spacing between slider and disk as the sum of a high frequency

contribution assumed to be known and a low frequency contribution assumed to be unknown. The high frequency part represents the periodic spacing variations due to surface features on the disk or the slider. The unknown part must be obtained during the numerical solution of the Reynolds equation. Homogenization techniques allow a much coarser domain discretization than direct approaches. Unfortunately, the local resolution of the pressure distribution of the air bearing decreases due to the application of homogenization techniques, making the use of homogenization undesirable if details of the pressure distribution due to surface features are of interest.

In this study the effect of discrete track disks on the flying characteristics of sub-ambient pressure sliders is investigated as a function of discrete track media parameters. A finite-element-based air bearing simulator [6] (CMRR simulator) was used to account for the characteristics of the grooved disk surface. The steady state flying behavior of typical proximity recording sliders over discrete track disks is studied and the influence of discrete track media parameters such as groove depth, groove width, and track pitch is investigated with respect to the flying behavior of five types of sub-ambient pressure slider. Groove depths from zero to 40nm and groove widths from $500nm$ to $1000nm$ were evaluated.

5.2 Mathematical Modelling

In this study the presence of discrete tracks is modeled as spacing variation of the slider air bearing. Averaging or homogenization techniques are not applied.

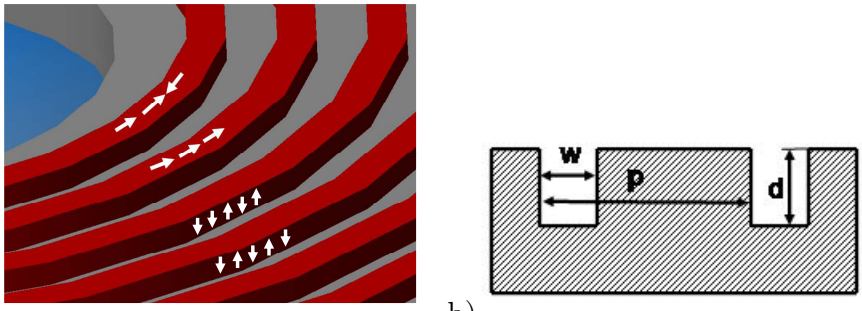

Figure 5.1: Schematic of a) discrete track disk and b) definition of discrete track disk parameters

Figure 5.1a shows a schematic of a typical discrete track disk. Individual bits are stored along the circumferential ridges on the disk surface (white arrows in Figure 5.1a). In Figure 5.1b the parameters defining discrete track media are shown, where w denotes the groove width, p the track pitch, and d the groove depth, respectively.

The simulation results presented in this study are based on a finite element solution of the Reynolds equation presented in chapter 4 of this thesis.

5.3 Simulation Model

One pico and four femto form factor slider designs with different steady state flying characteristics were simulated as a function of discrete track media design parameters.

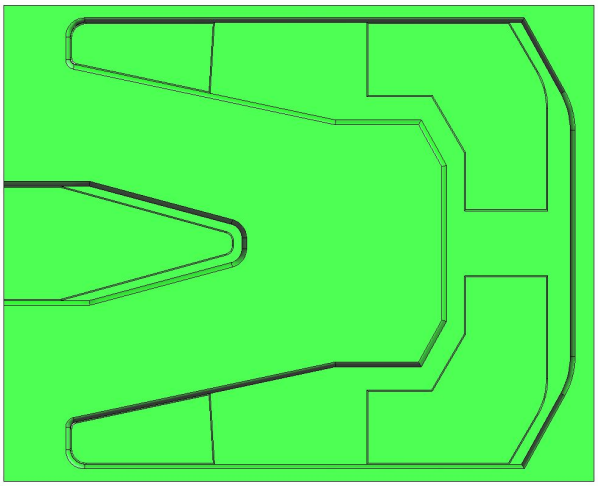

Figure 5.2: Pico form factor slider design (flying height on smooth disk: $4nm$)

Figure 5.2 shows the pico form factor slider used and Figure 5.3 the four femto form factor slider designs. The pico slider design has a nominal flying height of $4nm$ on a flat (non-grooved) disk surface, while the four femto sliders have steady state flying heights of $30nm$, $14nm$, $15nm$, and $19nm$, respectively, on a smooth disk. The four femto sliders are design modifications of the femto slider shown in Figure 5.3a. Starting with design #1 (Figure 5.3a), design #2 (Figure 5.3b) was obtained by decreasing the size of the center pad. Design #3 (Figure 5.3c) was

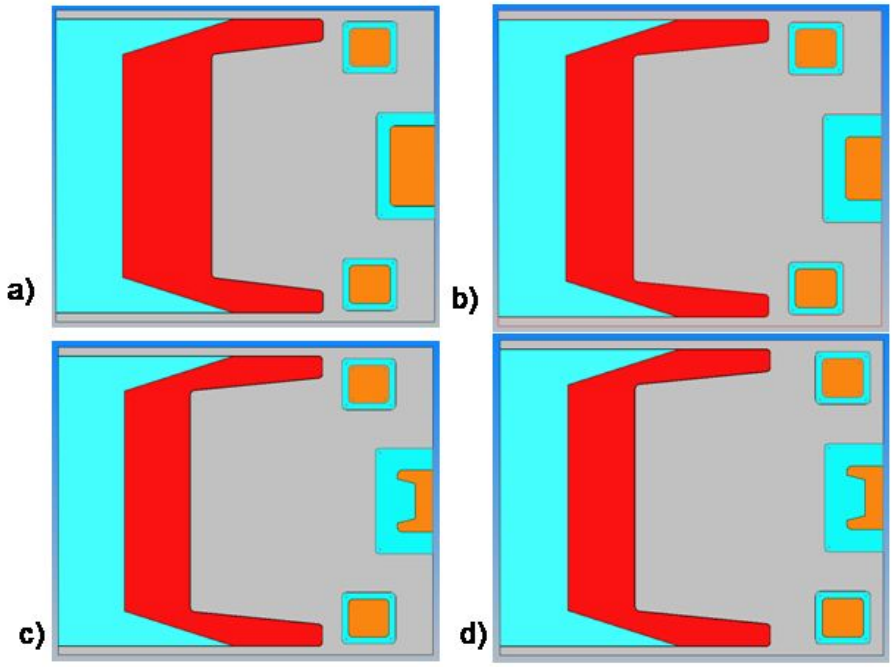

Figure 5.3: Femto form factor slider designs 1 to 4 (a to d, respectively)

derived from design #2 by reducing the length of the inner center pad. In design #4 (Figure 5.3d), the side pads were moved closer to the trailing edge. The steady state pitch angles of the four femto designs for a flat disk surface are $250\mu rad$, $170\mu rad$, $166\mu rad$, and $154\mu rad$, respectively. Different sets of discrete track parameter combinations were simulated. For the pico design, a groove width and track pitch of five micrometers ($5\mu m$) and ten micrometers ($10\mu m$), respectively, was chosen, resulting in a groove width to track pitch ratio of one half ($w/p = 1/2$). The groove depth was varied between zero and eight nanometers ($0 < d < 8nm$) for the pico design. For the femto designs a much smaller groove width of $500nm$ was

chosen. The track pitch for the femto slider simulations was $1000nm$, resulting in a ratio of groove width to track pitch of one half ($w/p = 1/2$). For the four femto designs, groove depths between zero and fifteen nanometers ($0 < d < 15nm$) were investigated.

In addition, the influence of skew angle (ranging from zero to $20deg$) and the effect of large groove depths was investigated for femto form factor design #3 (Figure 5.3c). For the pico slider design, a finite element mesh with an element edge length of $1\mu m$ was created. The mesh density was kept uniform. Due to the small groove width, a much finer discretization was needed for the femto designs. However, uniform mesh density over the complete air bearing surface would result in numerical models with several tens of millions of nodes. Models of that size are too large to be handled with present day computers. To reduce the model size, a non-uniform mesh was used for the simulation of the femto designs. Very small elements were used in the area of the trailing edge and increasingly larger elements elsewhere. In particular, in the trailing edge region of the center pad, an element edge length of $40nm$ was used. The rest of the center pad surface was meshed with elements of $100nm$ in edge length. The same element edge length was used for the two side pad surfaces. The rest of the air bearing surface was meshed with elements $1\mu m$ in edge length. In Table 5.1 details of a number of simulation models are summarized.

Table 5.1: Model size for different designs

	# nodes [10^6]	# elements. [10^6]
PICO	0.7	1.4
FEMTO 1	2.9	5.9
FEMTO 2	1.7	3.6
FEMTO 3	1.3	2.7
FEMTO 4	1.3	2.7

5.4 Simulation Results and Discussion

In Figure 5.4a, the pressure distribution is shown for the complete air bearing surface of the pico slider. An enlarged view of the pressure distribution over the trailing pad is shown in Figure 5.4b for flying on a discrete track disk and in Figure 5.4c for flying on a smooth disk. Comparing Figures 5.4b and 5.4c, one observes that the pressure distribution for the discrete track disk differs substantially from that of the smooth disk. Very narrow ridges of high pressure exist at the trailing edge of the slider due to the narrow land regions on the discrete track disk, while a rounded pressure distribution with much lower maximum pressure is found for the smooth disk.

In Figure 5.5 the pressure distribution for the trailing edge center region is shown for a) a smooth head/disk interface, b) an interface with $15nm$ groove depth, and c) an interface with $75nm$ groove depth, respectively. A coarse track pitch of $10\mu m$ and a groove width of $5\mu m$ were chosen, resulting in a groove width to track pitch ratio of one to two ($w/p = 1/2$). The trend in the pressure distribution of

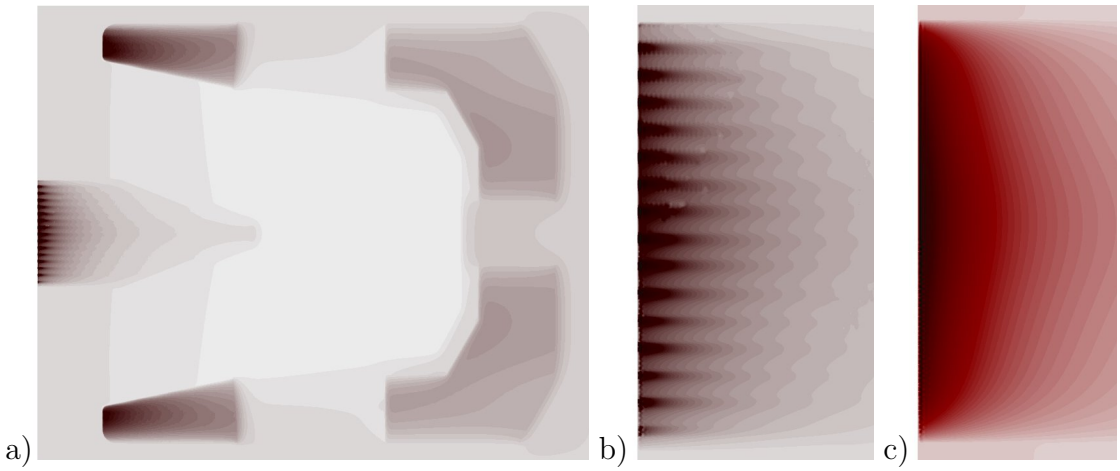

Figure 5.4: Typical pressure distribution of slider flying over discrete track disk a) entire air bearing pressure distribution, b) detail of pressure at center trailing pad for discrete track media c) detail of pressure distribution for smooth disk

the air bearing surface for increasing groove depths can clearly be observed. With increasing groove depth, the pressure distribution over a land region approaches more and more the shape of a delta function, i.e., increasingly higher pressure values over the land regions are observed, accompanied by a decrease in pressure over the groove regions. As the pressure over a land region increases, side flow from the land areas into the grooves increases. Increased side flow results in a reduction of the maximum achievable load carrying capacity of the air bearing. Clearly, side flow and maximum pressure are important parameters that need to be considered in the air bearing design process for discrete track disk interfaces.

In Figure 5.6 the loss of flying height versus groove depth is shown for a skew angle of zero degree. A linear relationship between groove depth and flying height

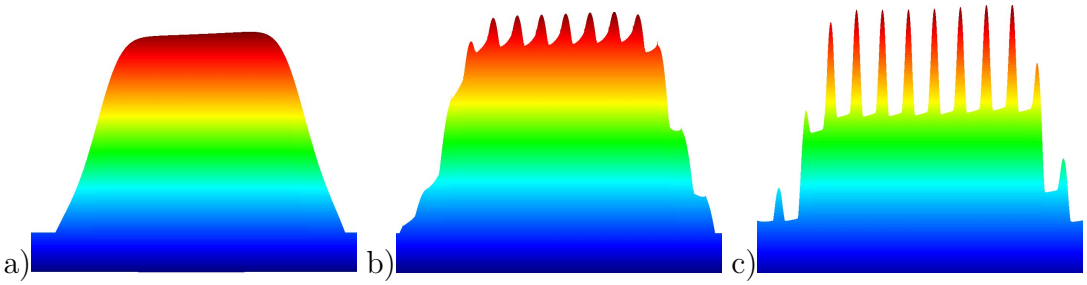

Figure 5.5: Trailing edge center pressure distribution for a) smooth disk, b) 15nm groove depth, c) 75 nm groove depth

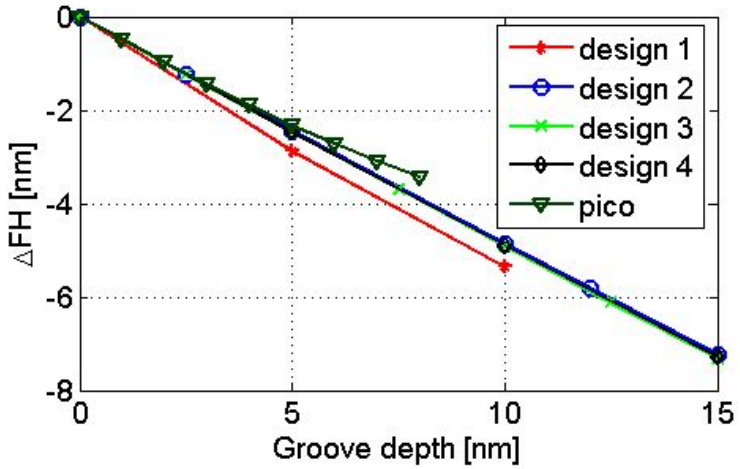

Figure 5.6: Flying height loss versus groove depth (groove width to track pitch ratio 1/2)

loss is observed. The following empirical equation can be used for estimating the loss in flying height ΔFH as a function of groove width, track pitch, and groove depth, i.e.,

$$\Delta FH = d \times \left(\frac{w}{p}\right). \tag{5.1}$$

Equation 5.1 quantifies the loss in flying height for a given slider design on a discrete

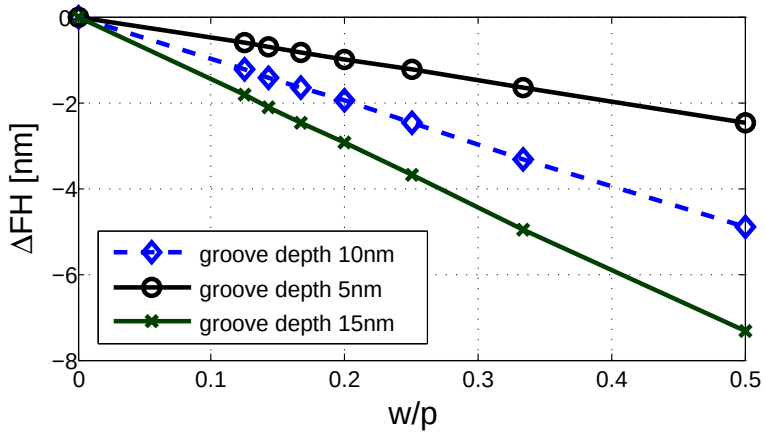

Figure 5.7: Change in flying height versus ratio of groove width to track pitch for femto slider design #3 with groove depth of $5nm$, $10nm$, and $15nm$, respectively

track disk if the flying height is known for a "smooth" head/disk interface. Thus, the steady state flying height of a slider on a discrete track disk can be estimated using equation 5.1 by subtracting ΔFH from the flying height on a smooth disk.

To validate equation 5.1 for general design purposes, the steady state flying height for ratios of groove width to track pitch ranging from zero (no grooves) to one half have been calculated, keeping the groove depth constant. Figure 5.7 shows the flying height change for femto form factor design #3 for groove depths of five, ten and fifteen nanometers ($5nm$, $10nm$, $15nm$), respectively. A linear relationship is observed for the change of flying height versus the ratio of groove width to track pitch, in agreement with equation 5.1.

In Figure 5.8 the trailing edge center spacing of slider femto design #3 is shown

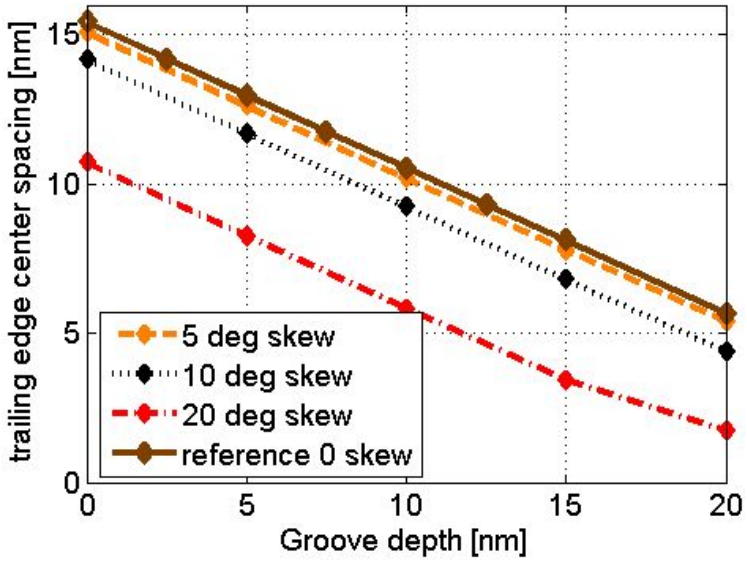

Figure 5.8: Trailing edge center spacing versus groove depth and skew angle

as a function of groove depth for skew angles of zero, five, ten, and twenty degrees $(0, 5, 10, 20$ deg), respectively. The ratio of groove width to track pitch was chosen to be one half ($w/p = 1/2$). A linear decrease in the trailing edge center spacing is observed with increasing groove depth, indicating the validity of equation 5.1 for non zero skew cases.

The dependence of the pitch angle on groove depth is shown in Figure 5.9. For the cases evaluated, one can observe that the change in pitch angle is nearly independent of slider design, groove depth, the ratio of groove width to track pitch, and the skew angle.

As was indicated in Figure 5.5, very high pressure values can be expected

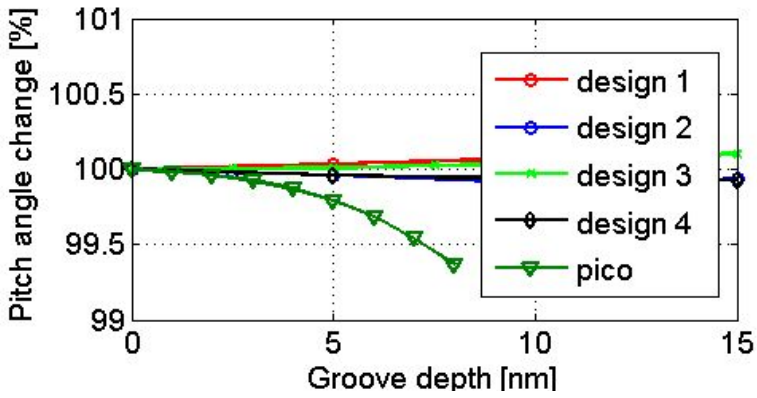

a)

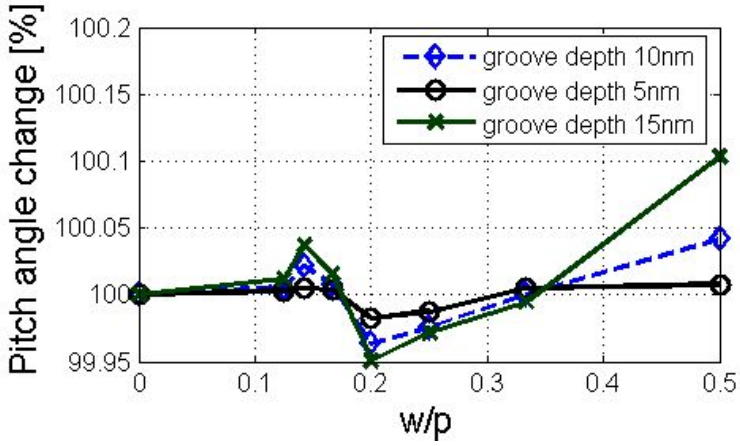

b)

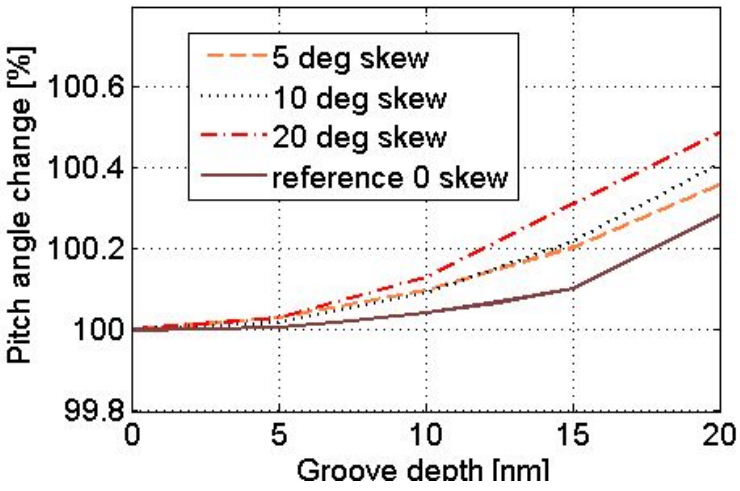

c)

Figure 5.9: Pitch angle change versus a) groove depth b) ratio of groove width to track pitch (femto slider design #3) c) groove depth and skew angle

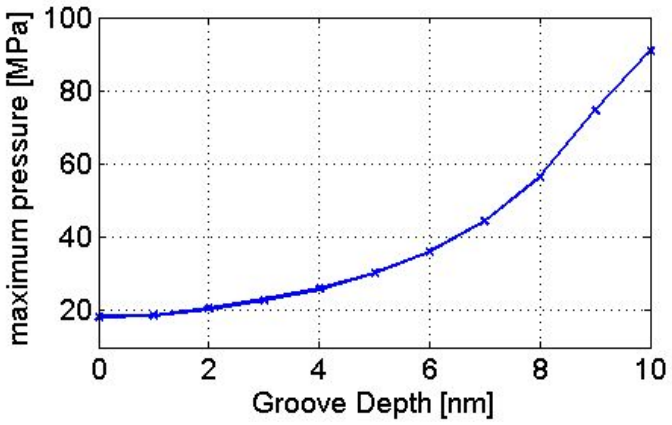

Figure 5.10: Absolute peak pressure change versus groove depth for pico design of Figure 5.2

for discrete track recording head/disk interfaces with very narrow land areas. In Figure 5.10 the peak pressure (maximum pressure occurring in the air bearing) versus groove depth is plotted for the investigated pico slider design. As can be seen, a maximum pressure of $9.1MPa$ ($90atm$) is observed for a groove depth of ten nanometers ($10nm$), while a maximum pressure of $1.8MPa$ ($18atm$) is observed at zero groove depth. Thus, the maximum pressure is increased by a factor of five for the discrete track disk under consideration as compared to a smooth disk. Air bearing pressures of this magnitude are likely to affect the lubricant film thickness and the migration of lubricant into the grooves of discrete tracks.

It is of interest to estimate the maximum groove depth for which equation 5.1 is valid. To investigate the limit of equation 5.1, the flying height change for very large groove depths for slider design #3 was simulated and compared with the flying height of the same slider over a smooth disk. Equation 5.1 predicts that the

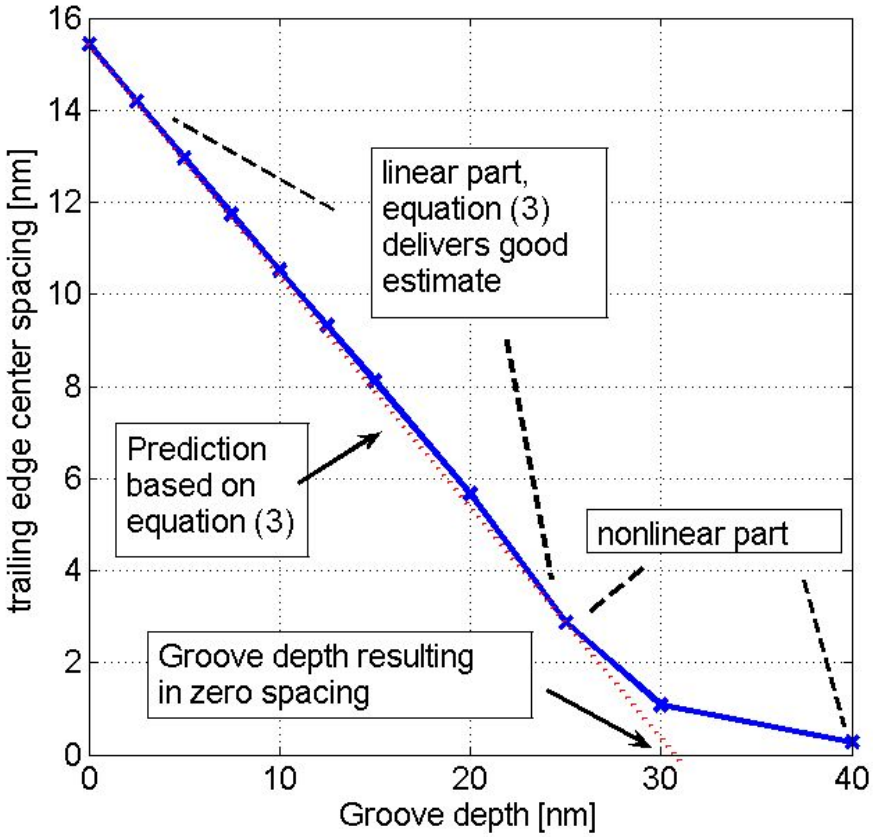

Figure 5.11: Change in flying height versus groove depth (femto form factor slider design #3)

flying height of a slider on a discrete track disk becomes zero if the parameters of the discrete track media are chosen in such a way that the flying height loss (ΔFH) equals the flying height of the slider on a smooth disk. For the femto slider design #3, a flying height of $15nm$ is calculated for flying on a smooth disk. Thus, zero flying height would occur for a groove depth of $30nm$ and a ratio of groove width to track pitch of one half ($w/p = 1/2$). Figure 5.11 shows

the trailing edge center spacing versus groove depth. One can observe that the simulation results begin to deviate from the results predicted by equation 5.1 at a groove depth of approximately $25nm$. As the groove depth increases further, numerical calculations show that the flying height approaches zero. Since this would result in contact and wear of slider and disk, air bearing design #3 should not be used for disks with groove depths larger than 30nm and a ratio of groove width to track pitch of one half ($w/p = 1/2$).

Equation 5.1 provides a useful tool in estimating the flying height reduction of a slider on a grooved disk surface. Using air bearing simulations for a head/disk interface without grooves, one can estimate the effect of discrete tracks by determining the reduction in flying height using equation 5.1 for known discrete track parameters.

5.5 Summary and Conclusions

The influence of discrete tracks on the steady state flying behavior of five different sub-ambient air bearing designs was investigated. It was found that the slider flying height decreases linearly with increasing groove depth and increasing ratio of groove width to track pitch. An empirical equation was found to describe the flying height loss as a function of discrete track parameters used. The range in which the equation delivers sufficient accurate results was estimated using one

slider design as a test case. No dependence of the slider pitch angle on discrete track parameters was found. The maximum pressure in a discrete track media head/disk interface increase with increasing groove depth and increasing ratio of discrete track groove width to discrete track track pitch.

To investigate the influence of the groove dimensions, particle based simulations are needed. The next chapter of this thesis introduces the direct simulation Monte Carlo method. This method is used for the simulation of rarefied gas flow in nano channels as presented in chapter 7 of this thesis.

5.6 Acknowledgement

This chapter is a partial reprint of material as it appears in:

- "***Air Bearing Simulation of Discrete Track Recording Media***", by Maik Duwensee, Shoji Suzuki, Judy Lin, David Wachenschwanz, and Frank E. Talke, IEEE Transactions on Magnetics, vol.42, no.10, p. 2489 - 2491, (2006)

- "***Simulation of the Head/Disk Interface for Discrete Track Media***", by Maik Duwensee, Shoji Suzuki, Judy Lin, David Wachenschwanz, and Frank E. Talke, published online in Microsystem Technologies (2006).

The dissertation author was the primary researcher and author and the co-authors listed in these publications directed and supervised the research which forms the basis for this chapter.

Bibliography

[1] Bertram, N. and Williams, M. *SNR and Density Limit Estimates: A Comparison of Longitudinal and Perpendicular Recording.* IEEE Trans. Mag., 36 (1), 2000.

[2] Buscaglia, G. and Jai, M. *Homogenization of the Generalized Reynolds Equation for Ultra-Thin Gas Films and Its Resolution by FEM.* ASME J. Trib., 126:547–552, 2004.

[3] Tagawa, N. and Bogy, D. *Air Film Dynamics for Micro-Textured Flying Head Slider Bearings in Magnetic Hard Disk Drives.* ASME J. Trib., 124:568–574, 2002.

[4] Tagawa, N., Hayashi, T., and Mori, A. *Effects of Moving Three-Dimensional Nano-Textured Disk Surfaces on Thin Film Gas Lubrication Characteristics for Flying Head Slider Bearings in Magnetic Storage.* ASME J. Trib., 123:151–158, 2001.

[5] Tagawa, N. and Mori, A. *Thin Film Gas Lubrication Characteristics of Flying Head Slider Bearings over Patterned Media in Hard Disk Drives.* Microsystem Technologies, 9:362–368, 2003.

[6] Wahl, M., Lee, P., and Talke, F. *An Efficient Finite Element-Based Air Bearing Simulator for Pivoted Slider Bearings using Bi-Conjugate Gradient Algorithms.* STLE Trib. Trans., 39 (1), 1996.

[7] Weissner, S., Tonder, K., and Talke, F. *Surface Roughness Effects in Compressible Lubrication.* In *Proceedings of AUSTRIB 1998, Brisbane.* 1998.

[8] Zhang, J., Su, L., and Talke, F. *Effect of Surface Texture on the Flying Characteristics of Pico Sliders.* IEEE Trans. Mag., 41 (10):3022–3024, 2005.

6

The Direct Simulation Monte Carlo Method

A basic introduction to the particle based simulation method direct simulation Monte Carlo (DSMC) based on [6] and [10] is given in this chapter. The main steps of a DSMC simulation program are introduced. Limitations and sources of errors are explained.

6.1 Introduction

The flow of a gas or liquid is generally modeled by the Navier-Stokes equations, which provide a mathematical description of the flow. In fluid dynamics, a fluid is generally treated as a continuum even though it is composed of individual

molecules. Fluid properties such as density, pressure, temperature, and velocity are defined at "infinitely" small points in the flow domain. The fluid properties are considered to vary continuously from one point to another. The fact that the fluid is composed of discrete molecules is ignored. The continuum assumptions break down when the average distance traveled by a fluid particle between collisions is equal to or larger than a typical length scale of the flow regime. For those situations, the linear transport terms for mass, diffusion, viscosity, or thermal conductivity are no longer valid and a microscopic description of the flow is needed.

Microscopic flow models are based on the assumption that the fluid consists of particles (atoms or molecules) influencing each other. This type of modeling is often referred to as a physical description of the flow. The Boltzmann equation [6, 7, 23] provides a statistical description of the position and motion of the atoms or molecules. The Boltzmann equation can be used to model the flow of rarefied gases.

The Knudsen number provides a convenient way of quantifying whether or not a flow regime should be described by a macroscopic or microscopic model. The Knudsen number Kn is defined as

$$Kn = \frac{\lambda}{L}, \tag{6.1}$$

where λ is the mean free path and L is the characteristic length of the flow regime.

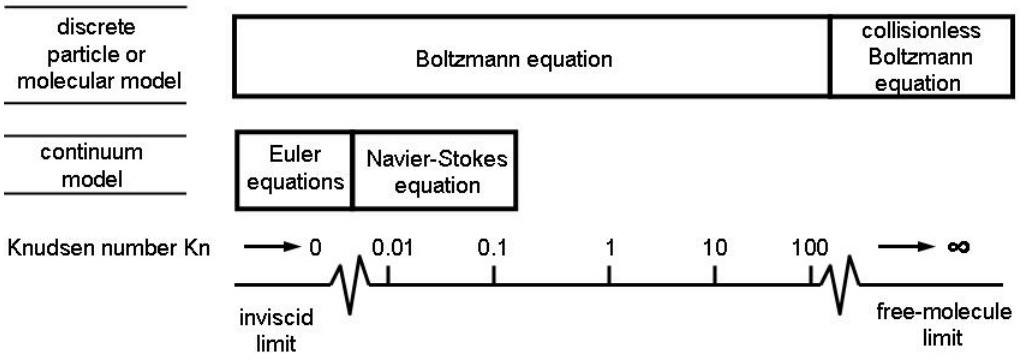

Figure 6.1: Knudsen number limits [6]

The continuum assumption breaks down when the Knudsen number is larger or equal to $Kn \approx 0.1$ [6, 21]. A number of researchers have used an even more stringent classification that considers the fluid as a continuum only for Knudsen numbers equal to or smaller than $Kn \leq 10^{-3}$ [4, 22].

Figure 6.1 [6] illustrates the Knudsen number limits for continuum-assumption-based flow models and particle-based flow models. The upper portion of Figure 6.1 illustrates the range of Knudsen numbers where particle or molecular based flow models are valid [6]. The lower portion shows the range of Knudsen numbers where continuum assumption based flow models are valid. As can be seen, the Navier-Stokes equations are valid up to Knudsen numbers of 0.1, while the Boltzmann equation is valid for Knudsen numbers up to 100. For Knudsen numbers larger than 100 the collisionless Boltzmann equation is valid. For the inviscid limit (Knudsen numbers much smaller than 0.01) the Euler equations can be used to model the

flow. At present, flow simulations based on particle models are restricted to very small systems, since the number of depended variables in the flow regime would otherwise be too large for present day computer systems. The number of particles in a cubic centimeter of gas at standard temperature and pressure is 2.687×10^{19} (Loschmidt's number). Assuming each particle to have six degrees of freedom, i.e., translation in the x, y, and z directions and rotation about the x, y, and z axis, with one velocity for each degree of freedom, the number of unknowns is $6 \times (2.687 \times 10^{19})$. This, clearly, is too large to be handled on present day computers.

A typical example of a flow regime, where the use of the Boltzmann-type equation would be necessary, is the description of a re-entry vehicle in the upper atmosphere. At high altitude the mean free path of air is on the order of several meters. The characteristic length scale of a re-entry vehicle is also on the order of meters, resulting in Knudsen numbers on the order of unity. As pointed out in chapter 1, the minimum spacing in "state of the art" head/disk interfaces is on the order of seven nanometers ($7nm$). The mean free path of air is on the order of 65nm (for air at standard temperature and pressure (STP)). Thus, the resulting Knudsen number is larger than $Kn > 0.1$ and comparable to the Knudsen number encountered for the simulation of upper atmosphere flight problems. Based on this, air bearing simulations of the head/disk interface of computer hard disk drives should be

based on particle models such as the Boltzmann equation. Unfortunately, even for a domain as small as that of the air bearing of the head/disk interface, particle-based-simulations are too time consuming for parametric studies. A reduction in simulation time for the numerical solution of the Boltzmann equation can be obtained using the direct simulation Monte Carlo (DSMC) method [6, 10, 24].

6.2 DSMC Simulation Algorithm

In direct simulation Monte Carlo simulations molecules or atoms are represented by so-called simulation particles. Each simulation particle represents a fixed number (N_{ef}) of actual molecules or atoms, i.e., N_{ef} molecules or atoms are represented by one simulation particle. The velocity components, position coordinates and internal states of the simulation particles are stored in the computer and are modified with time as the particles move through the physical space, collide with other particles, or interact with the boundaries of the physical space. The velocity-space information of the system is contained in the positions and velocities of the simulation particles. During the simulation the conservation of mass, momentum, and energy is enforced.

The DSMC method decouples the particle motion and the interparticle collisions over small time intervals. The particle motion is modeled deterministically, i.e., the position of a simulation particle at the end of a time interval is calculated

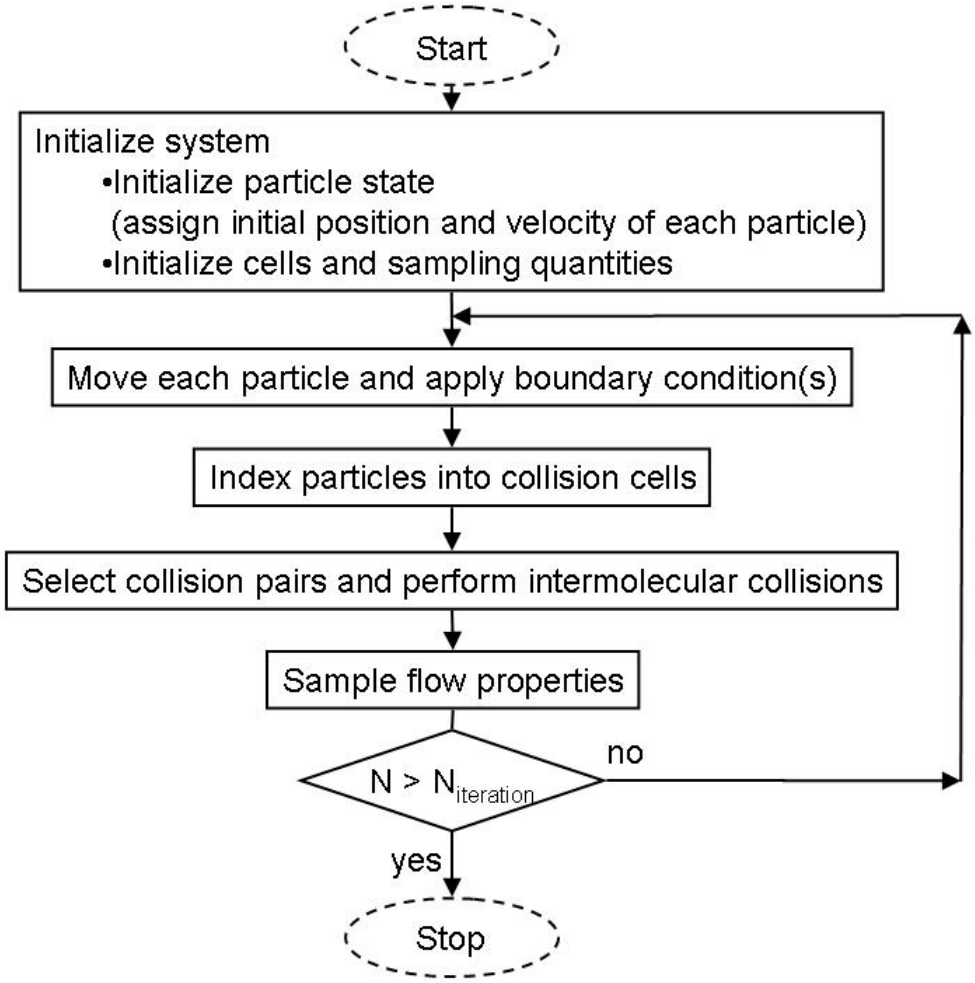

Figure 6.2: Flowchart of direct simulation Monte Carlo algorithm

from its current position, current velocity, and the length of the time interval. The interparticle collisions are modeled probabilistically, i.e., particles are chosen randomly for collision.

Figure 6.2 depicts the flowchart of a typical DSMC simulation program. Each step of the flowchart will be outlined below. As can be seen from Figure 6.2,

the simulation starts with initializing the simulation domain. During this step, the particles are randomly distributed over the simulation domain and a random velocity is assigned to each simulation particle based on Boltzmann statistics. After the initialization is performed, a simulation loop is started.

The first step in the simulation loop is to follow the motion of each particle to its new position according to its assigned velocity. In the case that particles move outside of the domain, they are removed from the simulation, i.e., the positions and velocities of the particles are deleted. In the case that particles collide with domain boundaries, the post-collision positions and velocities of the particles are calculated. This step is often referred to as advection step or streaming phase in a DSMC simulation.

After the velocity and position of each particle has been determined, all particles are grouped in so-called collision cells. In each collision cell, pairs of particles are randomly chosen as "collision pairs". Based on the relative velocity between the two particles of a chosen pair, the pair is accepted or declined for collision. If the pair is accepted for collision, the collision is processed and the post-collision velocities of the colliding particles are calculated. This step is referred to as the collision step. Once all collisions have been processed, flow properties are sampled and stored.

The advection and collision steps are repeated for a number of times ($N_{iteration}$).

In the sections below each step of the simulation algorithm is described in detail. A discussion and derivation of the direct simulation Monte Carlo method can be found in [6]. Additional details of the method are provided in [1, 7, 10, 23].

6.2.1 Initialization

At the start of a DSMC simulation all particles have to be distributed in the physical domain and their velocities have to be assigned. This step is considered the initialization step of a DSMC simulation. During the initialization the simulation particles are distributed randomly over the physical domain with uniform density. The speed v for each particle is obtained from the *Maxwell-Boltzmann* distribution, i.e.,

$$P(v) = 4\pi\sqrt{\left(\frac{m}{2\pi kT}\right)^3}\, v^2 e^{-\frac{\frac{1}{2}mv^2}{kT}} \tag{6.2}$$

where v is the speed of the particle, m is the particle mass, k is the Boltzmann constant ($k = 1.38 \times 10^{-23} J/K$) and T is the temperature. To obtain the speed of a particle from a Maxwell-Boltzmann distribution, the velocity components $u_x,\ u_y,\ u_z$ and $v = \sqrt{u_x^2 + u_v^2 + u_z^2}$ are picked from a Gaussian distribution with zero mean according to

$$\begin{aligned} P(u_x) &= \frac{1}{\sigma\sqrt{2\pi}}\, e^{-\frac{u_x^2}{2\sigma^2}}, \\ P(u_y) &= \frac{1}{\sigma\sqrt{2\pi}}\, e^{-\frac{u_y^2}{2\sigma^2}}, \\ P(u_z) &= \frac{1}{\sigma\sqrt{2\pi}}\, e^{-\frac{u_z^2}{2\sigma^2}}, \end{aligned} \tag{6.3}$$

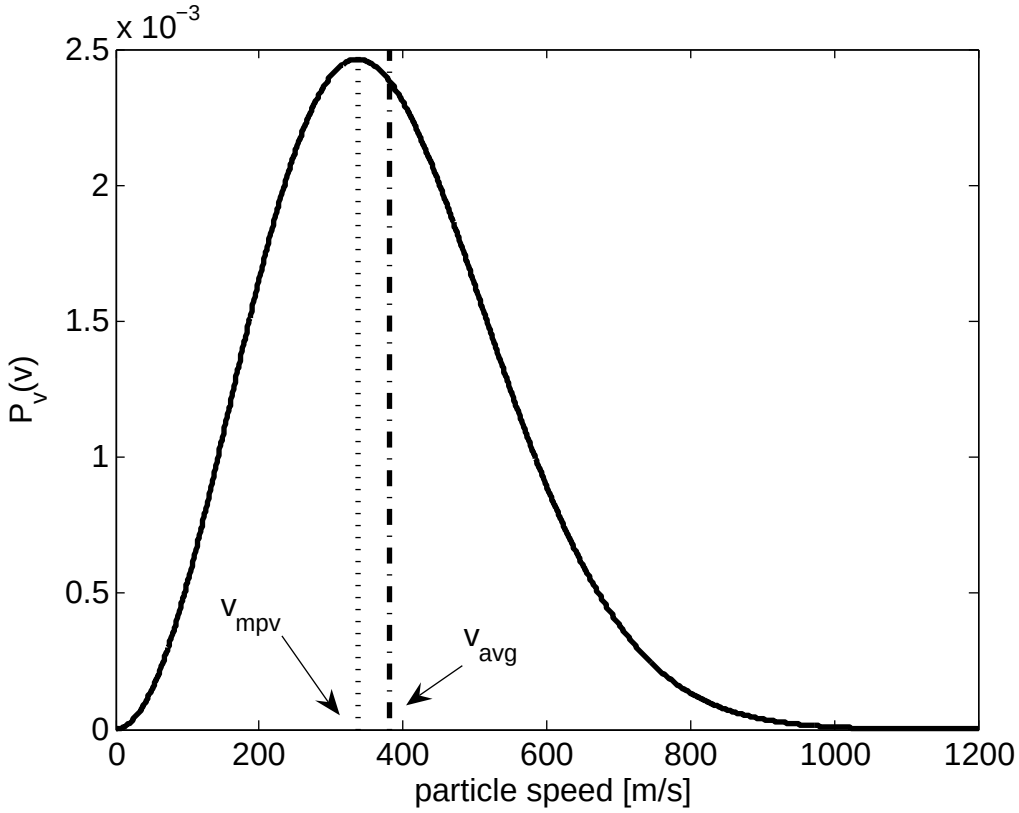

Figure 6.3: Maxwell-Boltzmann distribution of particle speed for Argon at a temperature of $T = 273K$ (reproduced from [10])

where σ is the standard deviation given by

$$\sigma = \sqrt{\frac{kT}{m}}. \tag{6.4}$$

Figure 6.3 shows the Maxwell-Boltzmann distribution of particle speed for Argon at $T = 273K$ (reproduced from [10]). In Figure 6.3, the most probable and average particle speed are also shown. The most probable speed v_{mpv} is the value of the speed of a particle that the particle attains with the highest probability. To calculate the most probable speed v_{mpv}, it is required that the first derivative of

equation 6.2 is zero, i.e.,

$$\frac{d}{dv}P(v)\bigg|_{v=v_{mpv}} = 0. \tag{6.5}$$

This results in

$$v_{mpv} = \sqrt{\frac{2kT}{m}}. \tag{6.6}$$

As can be seen from Figure 6.3, the average speed v_{avg},

$$v_{avg} = \int_0^\infty vP(v)dv = \frac{2\sqrt{2}}{\sqrt{\pi}}\sqrt{\frac{kT}{m}} \tag{6.7}$$

is not equal to the most probable speed v_{mpv}.

At the end of a DSMC initialization step the position vectors of each particle,

$$\boldsymbol{r}_i = \begin{Bmatrix} x_i \\ y_i \\ z_i \end{Bmatrix} \tag{6.8}$$

are assigned. In equation 6.8 $x_i,\ y_i$, and z_i are the coordinates of particle i within the physical simulation space. Additionally, the velocity vector of a particle is defined as

$$\boldsymbol{v}_i = \begin{Bmatrix} u_x \\ u_y \\ u_z \end{Bmatrix}, \tag{6.9}$$

where $u_x,\ u_y,\ u_z$ are the velocity components in the x, y, and z direction of particle i. During the evolution of the system over time the velocity-space information contained in $\boldsymbol{r}_i$ and $\boldsymbol{v}_i$ will be updated and recorded.

6.2.2 Streaming and Boundary Conditions

After initializing the state of the particles, the advection or streaming phase of a direct simulation Monte Carlo simulation is entered. During this phase all particles are assumed to move freely in space without influencing each other. The new particle positions are calculated based on

$$\boldsymbol{r}_i^{new} = \boldsymbol{r}_i^{old} + \boldsymbol{v}_i \Delta t, \tag{6.10}$$

where $\boldsymbol{r}_i^{new}$ is the new position of particle i, $\boldsymbol{r}_i^{old}$ is the position of particle i prior to entering the advection step, $\boldsymbol{v}_i$ is the velocity of particle i, and Δt is the chosen time-step for the simulation.

If a particle leaves the physical domain through a domain boundary, the associated boundary condition is applied, i.e., when a particle collides with a solid wall, the wall collision is processed, or when a particle leaves the domain through an open boundary, the particle position and velocity vectors are deleted. When a particle strikes a wall, the time of the impact Δt_{impact} is determined by calculating the straight line trajectory from the particles initial position $\boldsymbol{r}_i^{old}$ to the point of impact with the surface $\boldsymbol{r}_{impact}$ and computing

$$\Delta t_{impact} = \frac{\left(\boldsymbol{r}_{impact} - \boldsymbol{r}_i^{old}\right) \cdot \boldsymbol{n}}{\boldsymbol{v}_i \cdot \boldsymbol{n}}, \tag{6.11}$$

where $\boldsymbol{n}$ is the unit normal vector on the surface. After striking the wall, the particle is allowed to move freely with a new velocity for the remaining time

$\Delta t_{remain} = \Delta t - \Delta t_{impact}$. The new post-collision velocity of a particle depends on what boundary conditions are applied. Collisions with solid surfaces can be either fully specular, fully diffuse, or a combination of both.

For the case of a fully specularly reflecting wall, the velocity component of the particle normal to the wall of impact is reversed. The two other velocity components remain unchanged.

Fully diffuse wall collisions cause a totally random reorientation of the reflected particle. The post-collision velocity depends on the temperature of the surface $T_{surface}$. The velocity components are reset according to a biased Maxwellian distribution [6, 10]. The velocity component normal to the surface is randomly chosen (sampled) from

$$P_{\perp}(u_{\perp}) = \frac{m}{kT_{surface}}\, u_{\perp}\, e^{-\frac{mu_{\perp}^2}{2kT_{surface}}} \tag{6.12}$$

while the velocity components parallel to the surface are sampled from

$$P_{\parallel}(u_{\parallel}) = \sqrt{\frac{m}{2\pi kT_{surface}}} e^{-\frac{mu_{\parallel}^2}{2kT_{surface}}}. \tag{6.13}$$

To obtain random velocity values from the distributions 6.12 or 6.13 using Gaussian and uniform random number generators the velocity component normal to the surface can be computed from

$$u_{\perp} = \sqrt{-\frac{2kT_{surface}}{m} \ln r_{uniform}}, \tag{6.14}$$

where $r_{uniform}$ is a uniformly distributed random number in the interval (0, 1) and the velocity components parallel to the surface can be calculated according to

$$u_{\parallel} = \sqrt{\frac{kT_{surface}}{m}} r_{Gauss}, \tag{6.15}$$

where r_{Gauss} is a Gaussian distributed random number with zero mean and unit variance [1, 6, 10, 16].

Fully diffuse reflecting surfaces are also known as fully accommodating surfaces [1, 15]. The surface accommodation coefficient α for such a surface is equal to one ($\alpha = 1$). Surfaces that are neither fully diffuse nor fully specular have a surface accommodation factor of $\alpha < 1$. For such a surface, particles are reflected diffusively with a probability of α and specularly with a probability of $1 - \alpha$. For example, if $\alpha = 0.9$, particles are reflected diffusively with a probability of 0.9 and specularly with a probability of 0.1. When a particle strikes such a surface, a random number is taken from a uniform distribution in the interval [0, 1]. If the chosen number is smaller than $1 - \alpha$ the new particle velocity is computed based on fully specular surface reflection. If the number is larger than $1 - \alpha$, a fully diffuse reflection is used.

The model of surface interactions described above was suggested by Maxwell [20]. More complicated models for particle surface interactions have been suggested [6, 7, 8, 18, 19]. These models incorporate a variety of gas-surface effects in the DSMC methodology, such as chemical reactions at the boundaries due to high impact en-

ergies or surface catalysis.

A large number of simulation models use so-called open boundaries. At open boundaries particles can leave or new particles can enter the physical simulation space. The properties of entering molecules depend on macroscopic parameters such as pressure, density, or temperature at the open boundary. The position of an entering molecule, its time of entering, and its entering velocity have to be chosen randomly with the randomness based on the macroscopic properties at the boundary.

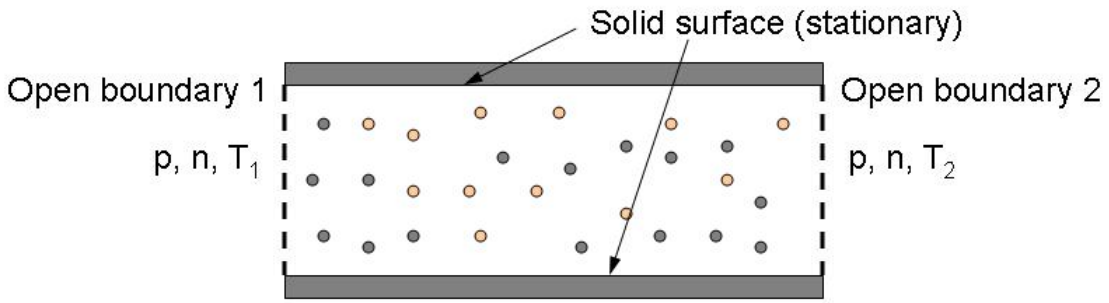

Figure 6.4: Example of simulation problem with two open boundaries

Figure 6.4 shows a schematic of a simple simulation problem to illustrate the application of an open boundary condition. The particle movement between two stationary parallel plates with two open boundaries 1 and 2 is depicted in Figure 6.4. At both open boundaries the pressure p and the number density n have the same values and are kept constant. At the open boundary 1 the gas has a constant temperature T_1. At the open boundary 2 the gas has a constant temper-

ature T_2. For the purpose of this example, it is assumed that the temperature T_1 is greater than temperature T_2 ($T_1 > T_2$). The velocity of particles at boundary 1 is sampled from a Maxwell-Boltzmann distribution based on equation 6.2 with $T = T_1$, i.e.,

$$P(v) = 4\pi\sqrt{\left(\frac{m}{2\pi kT_1}\right)^3}\, v^2 e^{-\frac{\frac{1}{2}mv^2}{kT_1}}. \tag{6.16}$$

The velocity of particles at boundary 2 is also sampled from a Maxwell-Boltzmann distribution based on equation 6.2 with $T = T_2$, i.e.,

$$P(v) = 4\pi\sqrt{\left(\frac{m}{2\pi kT_2}\right)^3}\, v^2 e^{-\frac{\frac{1}{2}mv^2}{kT_2}}. \tag{6.17}$$

Based on equation 6.6 one can conclude that the most probable particle velocity at boundary 1 $v_{mpv}|_1$ is greater than the most probable velocity at boundary 2 $v_{mpv}|_2$ ($v_{mpv}|_1 > v_{mpv}|_2$). A similar statement can be made for the average particle velocity (equation 6.7). Due to the higher velocity of particles at boundary 1, particles from boundary 1 will migrate through the channel and will leave the domain at boundary 2. However, particles can enter the simulation domain at boundary 2 and travel towards boundary 1, because choosing the velocity components randomly can result in a velocity vector pointing towards the inside of the domain for an outside particle.

In each time-step a number of particles enter the simulation space through open boundaries at random positions with a random velocity vector. There are several methods [6, 13, 17] to correctly chose the number, time, and velocity of entering

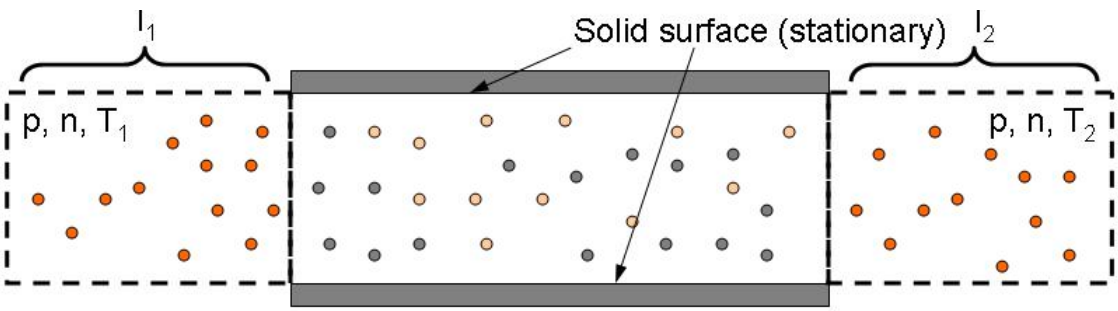

Figure 6.5: Schematic of implementation method for an open boundary condition

particles in each time-step. To provide an implementation example, a method introduced by Garcia et al. [12] will be illustrated. The method is based on an extension of the DSMC simulation to an external region adjacent to the DSMC simulation domain. Figure 6.5 shows a schematic of the implementation method applied to the example of Figure 6.4. As can be seen in Figure 6.5, a region is created at each open boundary adjacent to the DSMC simulation domain. Within each region particles are distributed uniformly and the velocities of the particles are sampled from a Maxwell-Boltzmann distribution based on equation 6.2 and the temperature of the boundary region. The number of particles created depends on the number density n of the external flow region and its physical dimension. The particles are then moved for a time Δt (chosen time-step for the simulation). Particles that cross the boundary and enter the simulation space are retained. The length l_i with $i = 1, 2$ of the adjacent regions is usually chosen to be

$$l_i = 3\ v_{mpv}|_i \Delta t, \tag{6.18}$$

where $v_{mpv}|_i$ is the most probable particle velocity at boundary i. By scaling the length of the external region using the most probable velocity v_{mpv} and the time-step length Δt, it is assured that the correct number of particles enter the simulation space during the evolution of the simulation. This is important for simulations where the boundary conditions change as a function of time.

6.2.3 Collisions

After all particles have been moved and the boundary conditions have been applied during the streaming or advection step of the DSMC algorithm, inter-particle collisions have to be processed. This step in a DSMC simulation is called the collision step. The collision step of the DSMC method is probabilistic. Pairs of particles are chosen at random as collision partners regardless of their position within the simulation space. It is theoretically possible in DSMC simulations that particles from different sides of the simulation space are chosen as collision partners. This procedure is counterintuitive, since intuition tells us to select only particles that are near each other for collisions. Particles that are far from each other should not be allowed to collide with each other. To implement such a condition, the particles are sorted into so-called collision cells and only particles that are located in the same cell are allowed to collide. Figure 6.6 depicts the application of collision cells to the problem introduced in Figure 6.4. More complex

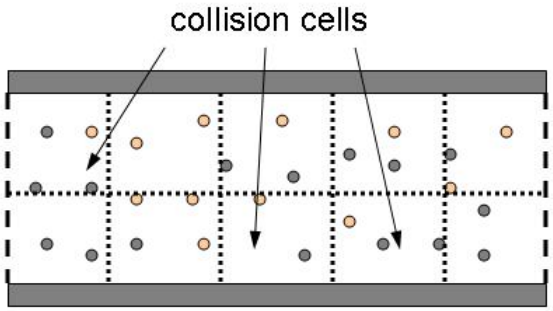

Figure 6.6: Schematic subdividing simulation space into collision cells

ways of choosing potential collision partners are possible. Such algorithms are computationally more expensive. The indexing of the particles into collision cells has been shown to deliver accurate simulation results [3, 6] as long as the physical dimensions of the collision cells are smaller than the mean free path.

Several models for inter-particle collisions have been reported [5, 6, 7, 23]. In this thesis the so-called hard-sphere model is used. The hard-sphere model can be compared to the collisions of two billiard balls.

In each simulation cell a set of representative collisions is processed at each time step. All particles within the cell can be considered as collision partners. In the hard-sphere model, the collision probability of a pair of particles is proportional to their relative speed. This can be expressed by

$$P_{collision}(i,j) = \frac{|\boldsymbol{v}_i - \boldsymbol{v}_j|}{\sum_{m=1}^{N_{cell}} \sum_{n=1}^{m-1} |\boldsymbol{v}_m - \boldsymbol{v}_n|} \tag{6.19}$$

where i and j indicate the two particles, and N_{cell} is the number of particles in the cell. Equation 6.19 is computationally expensive to use, due to the double sum

in the denominator. It is computationally more efficient to use an acceptance-rejection scheme instead. Applying such a scheme, the selection process for a randomly chosen pair of particles i and j can be summarized as follows:

1. A pair of collision candidates i and j is chosen at random.

2. Their relative speed, $v_{rel} = |\boldsymbol{v}_i - \boldsymbol{v}_j|$, is computed.

3. The pair is accepted as collision partners if $v_r > v_r^{max}\ r_{uniform}$, where v_r^{max} is the maximum relative velocity in the cell and $r_{uniform}$ is a uniformly distributed random number from the interval $(0, 1)$.

4. If the pair is accepted, the collision is processed; post-collision velocities of the particles are calculated and stored.

5. After the collision is processed or the pair is rejected, one returns to step (1) until the required number of collisions M_{coll} has been processed.

The number of collisions M_{coll} that needs to be processed [6, 10] for a given cell at a certain time step is

$$M_{coll} = \frac{N_{cell}(N_{cell} - 1)N_{ef}\pi d^2 \langle v_{rel} \rangle \Delta t}{2V_{cell}}, \tag{6.20}$$

where N_{ef} is the number of molecules or atoms represented by one simulation particle, d is the diameter of the particles, V_{cell} is the cell volume, $\langle v_{rel} \rangle$ is the

average relative particle velocity in the cell calculated by

$$\langle v_{rel} \rangle = \frac{1}{(N_{cell}-1)!} \sum_{i,j;\, i<j} |\boldsymbol{v}_i - \boldsymbol{v}_j| \,. \tag{6.21}$$

Performing the computation of equation 6.21 at each time step and for each collision cell is computationally expensive. The ratio of the number of accepted collision pairs M_{coll} to the number of candidate pairs M_{cand} is

$$\frac{M_{coll}}{M_{cand}} = \frac{\langle v_{rel} \rangle}{v_{rel}^{max}}, \tag{6.22}$$

since the probability of accepting a pair of particles as collision partners is proportional to their relative velocity. Combining equation 6.20 and 6.22 yields

$$M_{cand} = \frac{N_{cell}(N_{cell}-1)N_{ef}\pi d^2 v_{rel}^{max}\Delta t}{2V_{cell}}. \tag{6.23}$$

Equation 6.23 determines how many collision candidates should be selected over a time step Δt.

Once a collision pair has been accepted, the post collision velocities of the particles $\boldsymbol{v}_i^{post}$ and $\boldsymbol{v}_j^{post}$ have to be computed. The conservation of linear momentum requires the same "center of mass velocity" prior and after the collision. The velocity of the center of mass prior to the collision $\boldsymbol{v}_{cm}^{prior}$ is defined as

$$\boldsymbol{v}_{cm}^{prior} = \frac{1}{2}(\boldsymbol{v}_i + \boldsymbol{v}_j). \tag{6.24}$$

The center of mass velocity after the collision $\boldsymbol{v}_{cm}^{post}$ is calculated from the post collision velocities as

$$\boldsymbol{v}_{cm}^{post} = \frac{1}{2}(\boldsymbol{v}_i^{post} + \boldsymbol{v}_j^{post}). \tag{6.25}$$

The conservation of linear momentum requires

$$\boldsymbol{v}_{cm}^{prior} = \boldsymbol{v}_{cm}^{post}. \tag{6.26}$$

The relative velocity prior to the collision v_{rel}^{prior} is

$$v_{rel}^{prior} = |\boldsymbol{v}_i - \boldsymbol{v}_j|. \tag{6.27}$$

The relative velocity after the collision v_{rel}^{post} can be calculated from

$$v_{rel}^{post} = |\boldsymbol{v}_i^{post} - \boldsymbol{v}_j^{post}|. \tag{6.28}$$

The conservation of energy requires that the magnitude of the relative velocity of the particles prior to the collision and after the collisions remains unchanged:

$$v_{rel}^{prior} = v_{rel}^{post} \tag{6.29}$$

Equations 6.26 and 6.29 provide four constraint for the six unknows in $\boldsymbol{v}_i^{post}$ and $\boldsymbol{v}_j^{post}$. Two more constraint have to be found. The post collision relative velocity vector can be written as

$$\boldsymbol{v}_{rel}^{post} = v_{rel}\left[(\sin\Theta\cos\Phi)\hat{\boldsymbol{x}} + (\sin\Theta\sin\Phi)\hat{\boldsymbol{y}} + \cos\Theta\hat{\boldsymbol{z}}\right], \tag{6.30}$$

where $\hat{\boldsymbol{x}}$, $\hat{\boldsymbol{y}}$, and $\hat{\boldsymbol{z}}$ are the unit vectors in the x, y, and z direction, respectively. For the hard sphere model the angles Θ and Φ are distributed uniformly over the unit sphere [6, 10]. The angles Θ and Φ are chosen randomly according to

$$\Phi = 2\pi r_{uniform}, \tag{6.31}$$

and

$$\Theta = 2\pi r_{uniform}, \tag{6.32}$$

respectively, where, $r_{uniform}$ is a uniformly distributed random number in the interval $[0, 1)$.

Using equations 6.30, 6.31, and 6.32, the post collision velocities can be computed from

$$\begin{aligned} \boldsymbol{v}_i^{post} &= \boldsymbol{v}_{cm}^{post} + \tfrac{1}{2}\boldsymbol{v}_{rel}^{post} \\ \boldsymbol{v}_j^{post} &= \boldsymbol{v}_{cm}^{post} - \tfrac{1}{2}\boldsymbol{v}_{rel}^{post}. \end{aligned} \tag{6.33}$$

After the current collision pair has been processed, the next pair is chosen. In the case that the required number of collision candidates M_{cand} has been processed, collisions in the next cell will be computed.

6.2.4 Sampling

In DSMC simulations the velocity space information is stored in the position and velocity vector of each particle. Rather than evaluating each particle by itself based on its position and velocity, it is desirable to quantify the flow in terms of hydrodynamic variables such as pressure, temperature, or mass density. The hydrodynamic variables are directly related to the distribution of the particles within the physical simulation space and the velocity of the particles. To calculate hydrodynamic quantities, a so-called sampling step is included in most DSMC simulation programs. During the sampling step the particles are indexed into

sampling cells. For convenience, collision cells are often used as sampling cells. The instantaneous densities of mass ρ, momentum $\boldsymbol{J}$, and kinetic energy K for each cell are given by,

$$\rho = \frac{1}{V_C} \sum_{\boldsymbol{r}_k \epsilon\, C} m \tag{6.34}$$

$$\boldsymbol{J} = \frac{1}{V_C} \sum_{\boldsymbol{r}_k \epsilon\, C} m\boldsymbol{v}_k \tag{6.35}$$

$$K = \frac{1}{V_C} \sum_{\boldsymbol{r}_k \epsilon\, C} \frac{1}{2} m|\boldsymbol{v}_k|^2, \tag{6.36}$$

where the sums are over particles located within cell C, which has volume V_C. The instantaneous values for ρ, $\boldsymbol{J}$, and K are stored for each time-step and their mean values are calculated at the end of the simulation. After the mean values for the mass density $\bar{\rho_C}$, the linear momentum $\bar{\boldsymbol{J}}_C$, and the kinetic energy $\bar{K}_C$ have been calculated for each cell C, the mean fluid velocity $\bar{\boldsymbol{u}}_C$, and the mean temperature $\bar{T}_C$ can be computed as follows:

$$\bar{\boldsymbol{u}}_C = \frac{\bar{\boldsymbol{J}}_C}{\bar{\rho}_C} \tag{6.37}$$

$$\bar{T}_C = \frac{2m}{3k\bar{\rho}_C} \left(\bar{K}_C - \frac{|\bar{\boldsymbol{J}}_C|^2}{2\bar{\rho}_C} \right) \tag{6.38}$$

In Equation (6.38) k is the Boltzmann constant ($k = 1.3806 * 10^{-23}$J/K). The local pressure $\bar{p}_C$ may be calculated from the ideal gas law. It is important that the mean values for the mass density $\bar{\rho_C}$, the linear momentum $\bar{\boldsymbol{J}}_C$, and the kinetic energy $\bar{K}_C$ are used for the computation of hydrodynamic variables to avoid bias in the results [11].

6.3 Limitations of the DSMC method

The inherent constraints of the DSMC simulation method are:

1. The cell size used during the collision routine must be set proportional to the mean free path. The physical cell dimensions have to be a fraction of the mean free path.

2. The number of particles in each collision cell must be large enough to preserve collision statistics.

3. The simulation time-step must be chosen such that a particle needs several time-steps to travel through a collision cell.

In DSMC simulations each simulation particle represents several real molecules or atoms of the physical simulation space, i.e., a system is simulated using fewer molecules than are present in the real system. This increases the computationally efficiency. As in all discretization methods, a fine discretization in space or time can result in numerical errors due to accuracy limits of a digital computer. In DSMC simulations, statistical and numerical errors can occur due to the use of numerical and stochastic approaches for the streaming and collision phase, respectively.

The statistical and numerical errors of the method can be minimized by selecting an appropriate set of simulation parameters. The numerical error depends on the collision cell volume, time-step, and the total number of simulated parameter.

The length of the time-step should be chosen small enough so that a particle traverses only a fraction of the cell length within each time-step. It is recommended that the total number of simulation particles is chosen such that each simulation particle represents less than $20 - 30$ real molecules or atoms [6, 10, 23]. The cell volume and hence the dimensions of the collision cells should be chosen large enough to ensure that the number of particles in each cell is high enough to result in accurate collision statistics. To suppress statistical noise in DSMC simulations, sampling over a large number of time-steps is needed. Unfortunately, sampling over a large number of time-steps increases the run-time of a DSMC simulation; it is needed, however, to minimize the statistical noise error.

The two important computational limitations for DSMC simulations are run-time and storage requirements. Each simulation particle requires the storage of six double precision numbers (position and velocity vector). Additionally, sampling parameters have to be stored and updated for each sampling cell. Since the time step has to be small, the simulations are limited to very small time scales. Monte Carlo simulations can easily exceed computer run-times of several days. While heavy parallelized algorithms and computer architectures can be used, there will always be a limit to the run-time and storage of the velocity-space information of the simulation domain.

Bibliography

[1] Alexander, F. and Garcia, A. *The Direct Simulation Monte Carlo Method*. Computer in Physics, 11 (6):588–593, 1997.

[2] Alexander, F., Garcia, A., and Alder, B. *Direct Simulation Monte Carlo for Thin-film Bearings*. Phys. Fluids, 6 (12):3854–3860, 1994.

[3] Alexander, F., Garcia, A., and Alder, B. *Cell Size Dependence of Transport Coefficients in Stochastic Particle Algorithms*. Phys. Fluids, 10 (6):1540–1542, 1997.

[4] Beshok, A. and Karniadakis, G. *A Model for Flows in Channels, Pipes, and Ducts at Micro and Nano Scales*. Microscale Thermophys. Eng., 3:43–77, 1999.

[5] Bhatnagar, P., Gross, E., and Krook, M. *A Model for Collision Processes in Gases. I. Small Amplitude Processes in Charged and Neutral One-Component Systems*. Phys. Rev., 94 (3):511–525, 1954.

[6] Bird, G. *Molecular Gas Dynamics and the Direct Simulation of Gas Flows*. Oxford University Press, 1994.

[7] Cercignani, C. *Rarefied Gas Dynamics*. Cambridge University Press, first edition, 2000.

[8] Cercignani, C. and Lampis, M. *Kinetic Models for Gas-Surface Interactions*. Transport Theory Stat. Phys., 1:101–114, 1971.

[9] Chen, G. and Boyd, L. *Statistical Error Analysis for the Direct Simulation Monte Carlo Technique*. J. Comp. Phys., 126:434–448, 1994.

[10] Garcia, A. *Numerical Methods for Physics*. Prentice Hall, second edition, 2000.

[11] Garcia, A. *Estimating Hydrodynamic Quantities in the Presence of Microscopic Fluctuations*. Comm. App. Math. and Comp. Sci., 1 (1):53–78, 2006.

[12] Garcia, A., Bell, J., Crutchfield, W., and Alder, B. *Adaptive Mesh and Algorithm Refinement using Direct Simulation Monte Carlo*. J. Comp. Phys., 154 (1):134–155, 1999.

[13] Garcia, A. and Wagner, W. *Generation of the Maxwellian Inflow Distribution*. J. Comp. Phys., 217:693–708, 2006.

[14] Huang, W. and Bogy, D. *An Investigation of a Slider Air Bearing with a Asperity Contact by a Three Dimensional Direct Simulation Monte Carlo Method*. IEEE Trans. Mag., 34 (4):1810–1812, 1998.

[15] Huang, W. and Bogy, D. *The Effect of the Accommodation Coefficient on Slider Air Bearing Simulation*. ASME J. Trib., 122:427–435, 2000.

[16] Huang, W., Bogy, D., and Garcia, A. *Three-Dimensional Direct Simulation Monte Carlo Method for Slider Air Bearings*. Phys. Fluids, 9 (6):1764–1769, 1997.

[17] Lilley, C. and Macrossan, M. *Methods for Implementing the Stream Boundary Condition in DSMC Computations*. Int. J. Numer. Meth. Fluids, 42:1363–1371, 2003.

[18] Lord, R. *Some Extensions to the Cercignani-Lampis Gas Scattering Kernel*. Phys. Fluids A, 3:706–710, 1991.

[19] Lord, R. *Some Further Extension of the Cercignani-Lampis Gas-Surface Interaction Model*. Phys. Fluids, 7:1159–1161, 1995.

[20] Maxwell, J. *On Stresses in Rarefied Gases Arising from Inequalities of Temperature*. Philos. Trans. R. Soc. London, 170:231, 1867.

[21] Oran, E., Oh, C., and Cybyk, B. *Direct Simulation Monte Carlo: Recent Advances and Applications*. Annu. Rev. Fluid Mech., 30:403–441, 1998.

[22] Schaff, S. and Chambre, P. *Flow of Rarefied Gases*. Princeton University Press, 1961.

[23] Shen, C. *Rarefied Gas Dynamics*. Springer, first edition, 2005.

[24] Wagner, W. *A Convergence Proof for Bird's Direct Simulation Monte Carlo Method for the Boltzmann Equation*. J. Stat. Phys., 66:1011, 1992.

7

Simulation of Rarefied Gas Flow in Nano Channels

The direct simulation Monte Carlo method (DSMC) is used to study rarefied gas flow between an inclined plane slider bearing and a nano channel representing one groove in discrete track recording head/disk interfaces. The forces acting on the slider are investigated as a function of slider pitch angle, disk velocity, track pitch, groove width, and groove depth.

7.1 Introduction

To increase the storage density beyond $500 Gbit/in^2$ the development of patterned media technologies is being pursued. In patterned media one can distinguish

between bit patterned media and discrete track media. Both technologies were introduced in chapter 1.

In chapter 5, air bearing simulation results based on the Reynolds equation 4.14 (chapter 4) were presented. The steady state slider flying height and attitude were simulated as a function of groove width, groove depth, and groove pitch. Different sub-ambient slider air bearing designs were used.

In this chapter simulation results for rarefied gas flow in a nano channel based on the direct simulation Monte Carlo (DSMC) method are presented. The DSMC method was introduced by Bird [2] in the early 1970s. Alexander et al. [1] applied the method to check the validity of the modified Reynolds equation for high Knudsen number flow in a "smooth" head/disk interface. Their results were based on a two dimensional model. Huang et al. [6] extended the method presented in [1] to three dimensions. They also investigated asperity contact in head/disk interfaces with the DSMC method [5]. The DSMC method provides a simulation method for the investigation of nano scale effects of the head/disk interface for discrete track and bit patterned media.

7.2 Simulation Model

In this chapter the particle flow between a nano channel and an inclined plain slider comparable to a discrete track recording head/disk interface was simulated

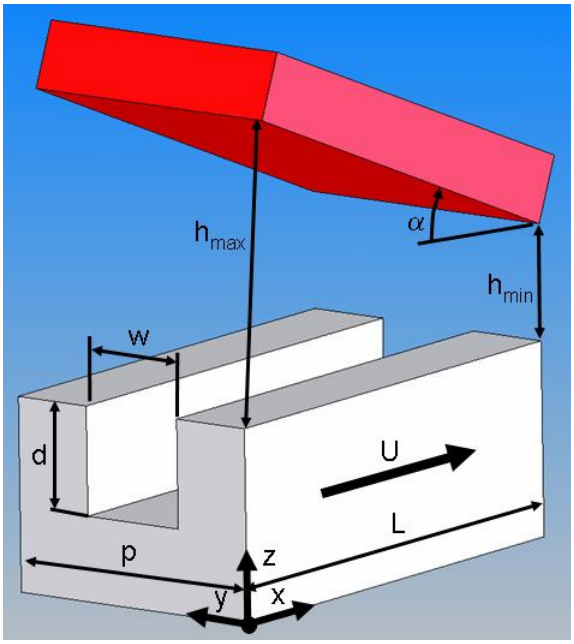

Figure 7.1: Simulation domain

using the DSMC method. Figure 7.1 depicts the simulation domain, where w, p, and d represent the groove width, track pitch and groove depth of a discrete track disk, respectively. The length of the domain is depicted by L. U represents the disk speed. The height at the leading edge is h_{max} and the height at the trailing edge is h_{min}. Both values are measured from the top of the disk surface. The pitch angle is represented by α. Argon with an atomic diameter of 0.366nm (3.66Å) and an atomic mass of 6.63×10^{-26}kg was used. The temperature was set to be $T = 273$K.

Figure 7.2 shows the boundary conditions for the problem. At the leading and

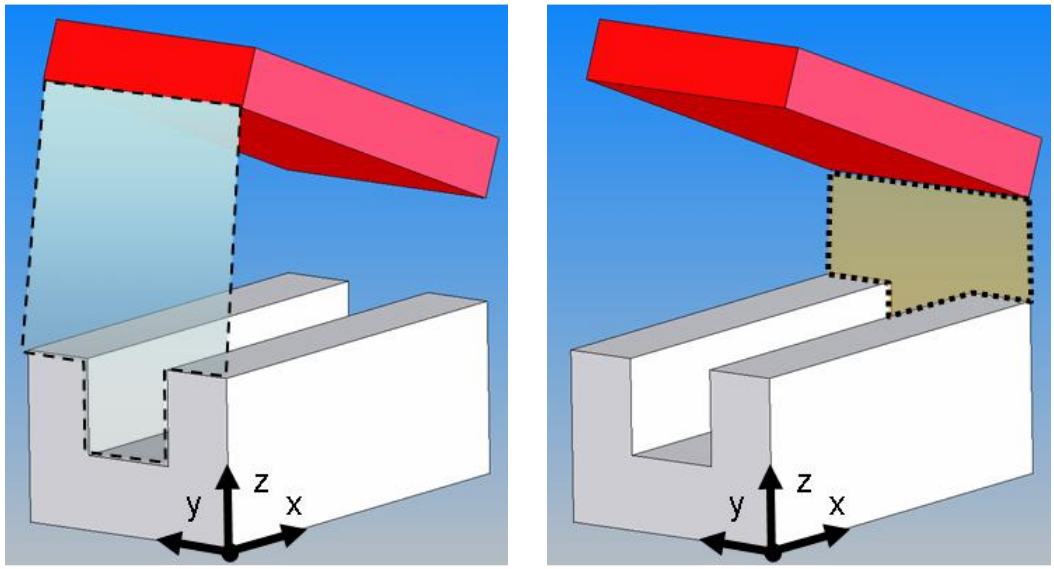

a) b)

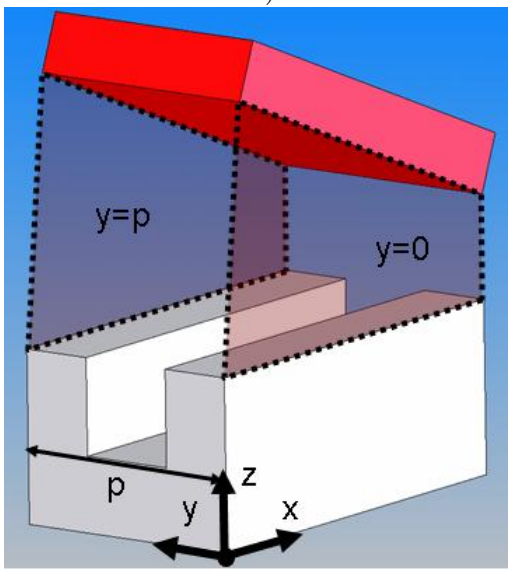

c)

Figure 7.2: Applied boundary condition a) and b) inflow/outflow boundary condition, c) periodic boundary condition

trailing edge (Figure 7.2a, Figure 7.2b) open boundary conditions are used. At the side of the domain, a periodic boundary condition is applied (Figure 7.2c).

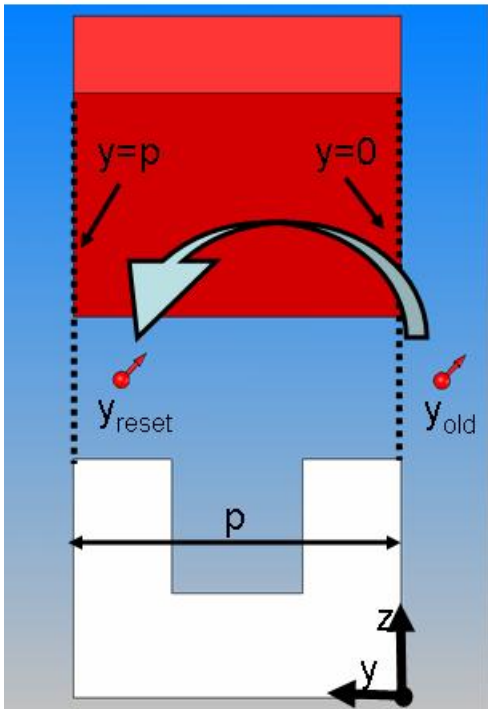

Figure 7.3: Illustration of periodic boundary condition

Particles that leave the domain through either one of the boundaries depicted in Figure 7.2c are placed back into the domain as if they would have entered the domain from the opposite side. Figure 7.3 illustrates how a particle that left the domain is placed back into the domain. By applying periodic boundary conditions, an infinitely large number of nano-channels is simulated. All slider surface and walls of the nano-channel are assumed to be diffusely reflecting walls.

To estimate the force acting on the slider surface, the change of linear momentum of particles colliding with the slider is recorded during the simulation. The

change in particle velocity for particles hitting the slider is stored and averaged over a large number of time steps. The change in the velocity of particles is used to calculate the change in linear momentum. The rate of change of momentum represents the force on the slider surface during collisions.

7.3 DSMC Simulation Results

A number of different slider bearing configurations have been studied. In all simulations the length of the domain was chosen to be five micrometers ($L = 5\mu$m). The mean free path of Argon at atmospheric pressure and temperature of $T = 273$K is approximately 62nm. The minimum spacing was selected to be five nanometers ($h_{min} = 5$nm), resulting in a Knudsen number of approximately twelve ($Kn \approx 12$).

The effect of pitch angle and disk velocity was studied first. The pitch angle was adjusted by changing the inlet height h_{max} (see Figure 7.1). Figure 7.4 shows the air bearing force on the slider as a function of the groove depth d for inlet heights of ten and fifteen nanometers ($h_{max} = 10$, 15nm), respectively, corresponding to a pitch angle of $\alpha = 0.001$rad and $\alpha = 0.002$rad. The pitch angle was chosen to be the same as in [1, 6]. Two different channel geometries were simulated. In the first, a track pitch of $p = 60$nm was used with a groove width of $w = 30$nm. In the second, a track pitch of $p = 80$nm was used with a groove width of $w = 40$nm. One observes

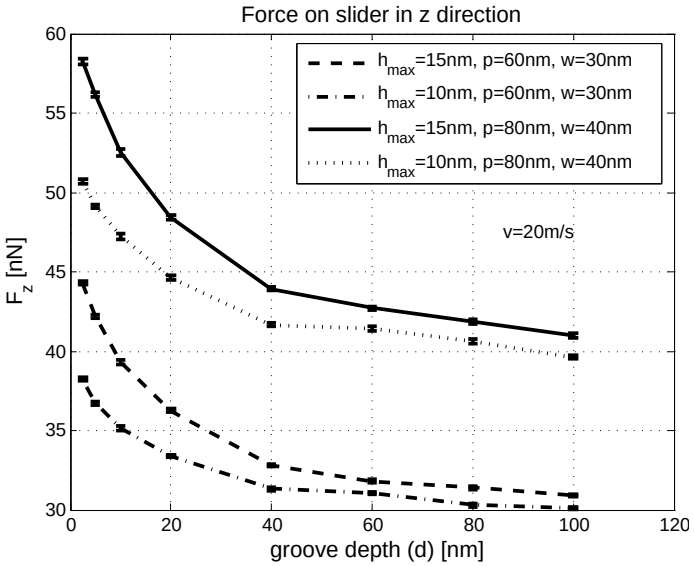

Figure 7.4: Air bearing force acting on slider versus groove depth for different pitch angles

that the force on the slider increases with increasing pitch angle, increasing track pitch, and increasing groove width. These results are intuitive. As the cross section of the domain is increased, more particles impact the slider surface; this results in an increased air bearing force. In Figure 7.5 the air bearing force normalized by the track pitch p is plotted versus the groove depth d. Normalization with the track pitch p allows a direct comparison of the slider force for different domain dimensions. From Figure 7.5 one observes that the force is a function of the pitch angle α and the groove depth d. The four curves from Figure 7.4 have collapsed into two curves, each representing the air bearing force as a function of groove depth for a constant pitch angle.

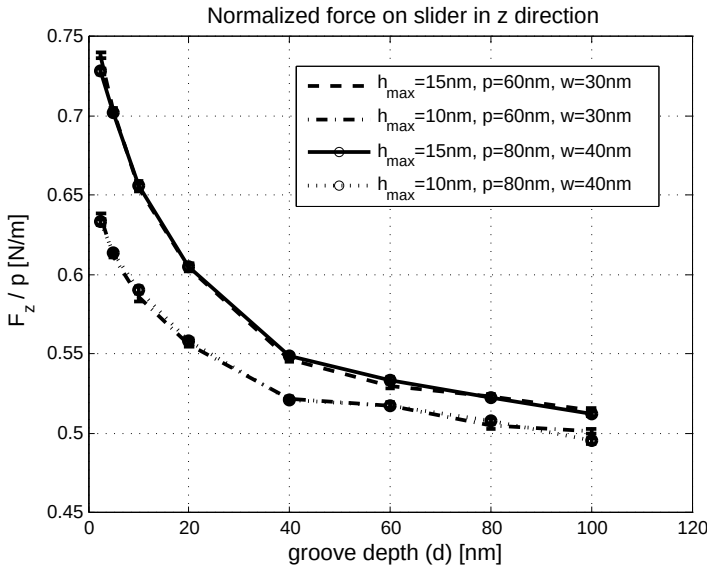

Figure 7.5: Air bearing force acting on slider for different pitch angles normalized with track pitch p

In Figure 7.6 the normalized air bearing force is plotted as a function of the groove depth d for disk velocities of 20m/s and 50m/s, respectively, using the channel geometries as for Figure 7.4 and 7.5. From Figure 7.6 one observes that the normalized air bearing force increases with speed and decreases with increasing groove depth d.

Figure 7.7 and Figure 7.8 show the friction and air bearing force of a typical slider as a function of groove depth and groove width. The track pitch p, inlet height h_{max}, and disk speed U were chosen to be $p = 120$nm, $h_{max} = 10$nm, and $U = 20$m/s, respectively. The groove width w was varied from 10nm to 100nm, while the groove depth d was varied from 2.5nm to 100nm, respectively. Table 7.1

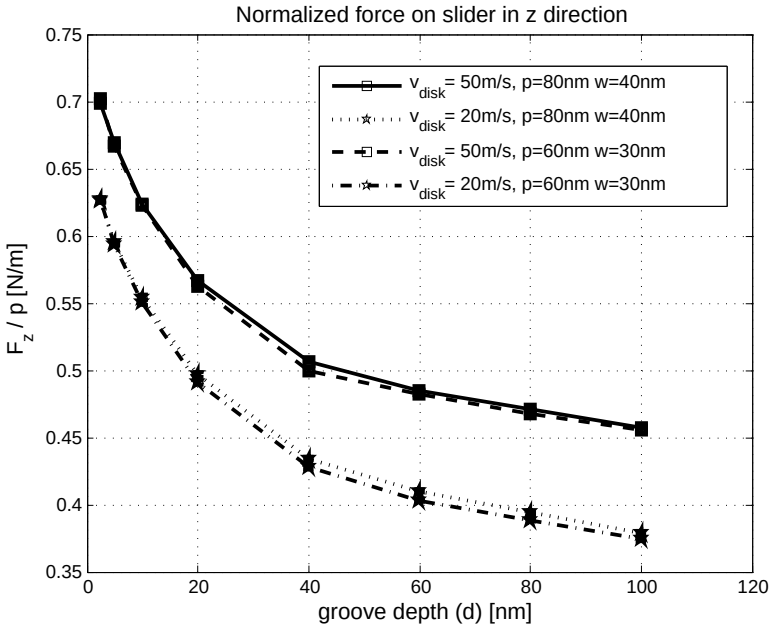

Figure 7.6: Air bearing force acting on slider for different disk velocities normalized with track pitch p

summarizes the parameters used. One observes from Figure 7.7a and Figure 7.7b that both the friction force and the air bearing force decrease with increasing groove depth d at constant groove width w. Furthermore, one can observe that the gradient of the force decreases with increasing groove depth. In particular, both the friction and air bearing force converge to constant values for increasing groove depth keeping the groove width constant.

In Figure 7.8a and b the friction and air bearing force is plotted as a function of the groove width w for different values of the groove depth d. One observes that the forces decrease with increasing groove width w keeping the groove depth d

Table 7.1: Parameters used for investigation groove depth d and width w on air bearing force

width w [nm][1]	ratio w/p [nm]	depth d [nm]
10	1/12	2.5, 5, 10, 20, 40, 60, 80, 100
20	1/6	2.5, 5, 10, 20, 40, 60, 80, 100
40	1/3	2.5, 5, 10, 20, 40, 60, 80, 100
60	1/2	2.5, 5, 10, 20, 40, 60, 80, 100
80	2/3	2.5, 5, 10, 20, 40, 60, 80, 100
100	10/12	2.5, 5, 10, 20, 40, 60, 80, 100

constant. Furthermore, one can observe that both the friction and the air bearing force converge to constant values for constant groove depth and increasing groove width.

The number of grooves that a slider "sees" is a function of the track pitch p and groove width w. To investigate the effect of groove dimensions on friction and air bearing pressure forces, the friction and air bearing force as a function of the groove width were calculated, keeping the ratio of groove width to track pitch w/p constant. Figure 7.9 shows the cases investigated of a ratio of $w/p = 0.5$. The track pitch p was varied from $p = 20$nm to $p = 200$nm. For each track pitch, the groove depth was varied from $d = 2.5$nm to $d = 100$nm. A summary of the parameters used is given in table 7.2.

In Figure 7.10 the ratio of air bearing force over track pitch p is plotted vs. groove depth d for all cases simulated. One observes that all curves show a similar dependence of the force on the groove depth d.

In Figure 7.11 the ratio of air bearing force over track pitch p is plotted vs.

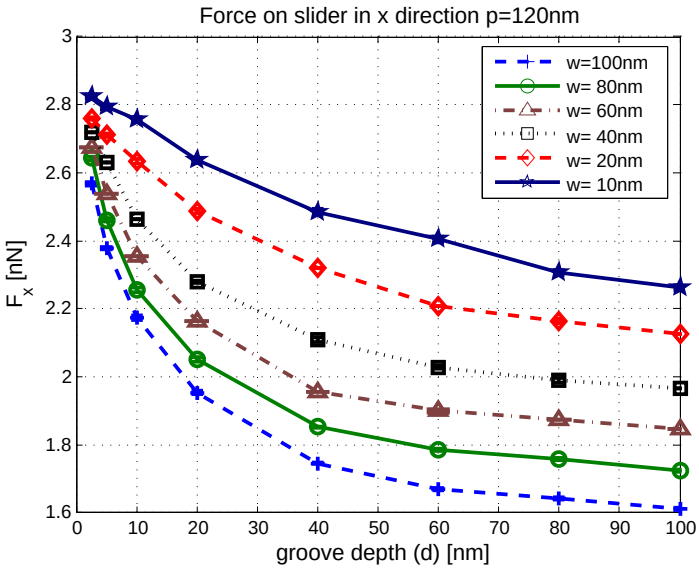

a)

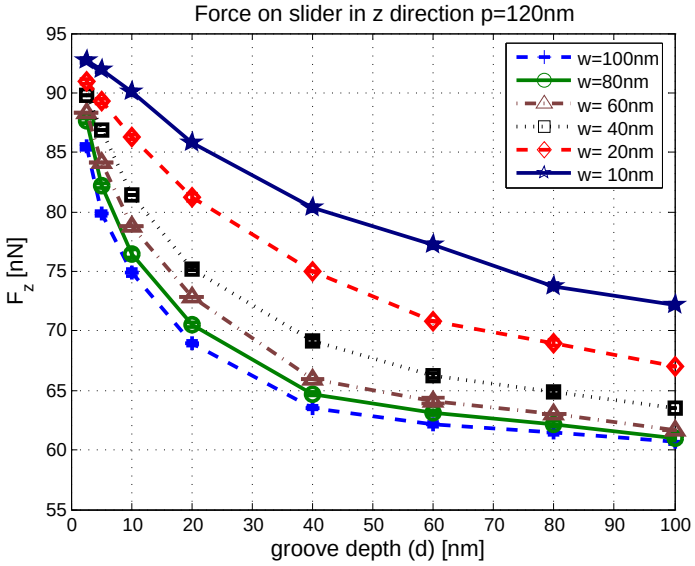

b)

Figure 7.7: Force acting on slider versus groove depth and constant groove width a) friction force, b) air bearing force

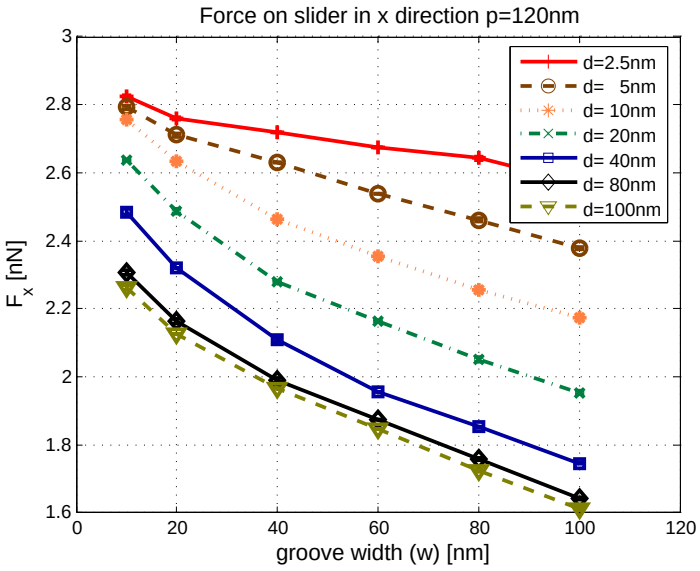

a)

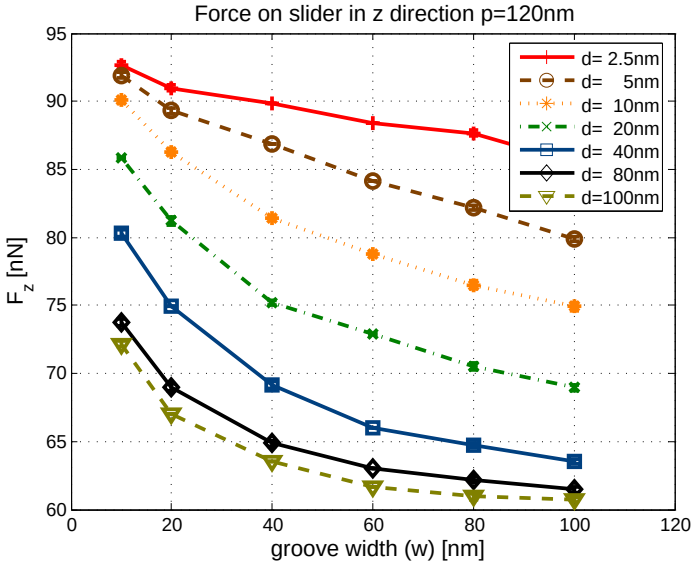

b)

Figure 7.8: Force acting on slider versus groove width and constant groove depth a) friction force, b) air bearing force

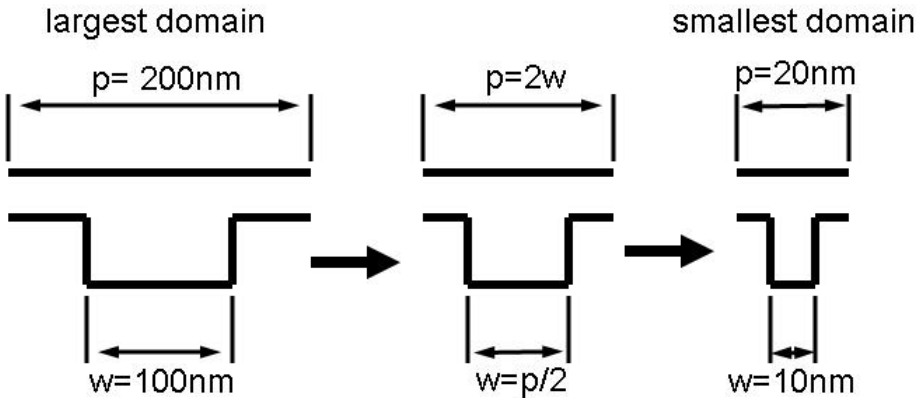

Figure 7.9: Schematic of nano channel with w/p constant

Table 7.2: Parameters used for investigation of vertical domain walls on air bearing force

pitch p [nm]^2	width w [nm]	depth d [nm]
20	10	2.5, 5, 10, 20, 40, 60, 80, 100
40	20	2.5, 5, 10, 20, 40, 60, 80, 100
⋮	⋮	⋮
200	100	2.5, 5, 10, 20, 40, 60, 80, 100

groove width w for all cases simulated. One observes that the force is constant for a given groove depth d and increasing groove width w.

7.4 Discussion

The DSMC simulations conducted in this study have shown that wide and deep grooves result in a reduction of the air bearing force keeping all other parameters constant. In addition, the gradient of the friction and air bearing force decreases

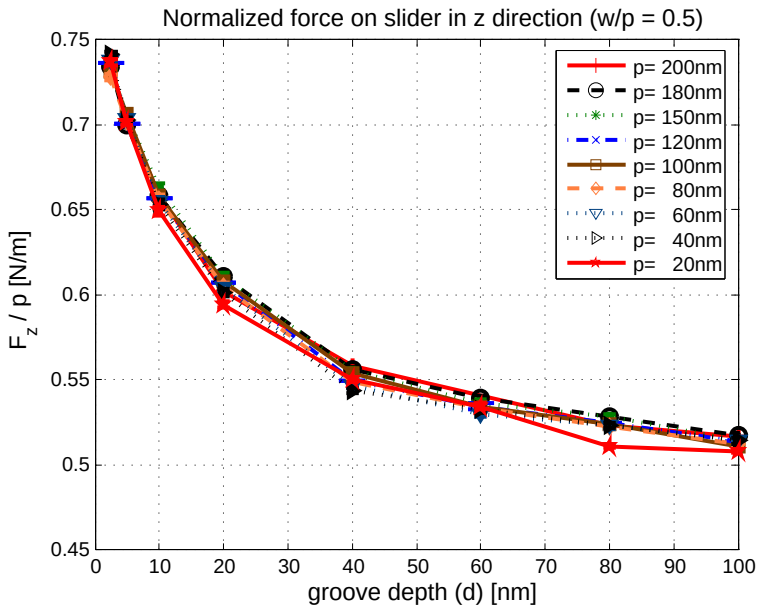

Figure 7.10: Air bearing force/track pitch versus groove depth d ($w/p = 0.5$)

as a function of the groove depth d (Figure 7.7). Both the friction and the air bearing force approach a constant value for deep grooves. This indicates that the friction and air bearing force will be more affected by manufacturing tolerances for designs using shallow grooves rather than deep grooves. Based on this result, deep grooves are recommended for the design of discrete track recording head/disk interfaces. A similar effect was shown for the slider force as a function of groove width w (Figure 7.8). For narrow grooves, a steeper gradient of friction and air bearing force was observed than for wider grooves, i.e., manufacturing tolerances of narrow grooves have a larger effect on the slider characteristics than manufacturing

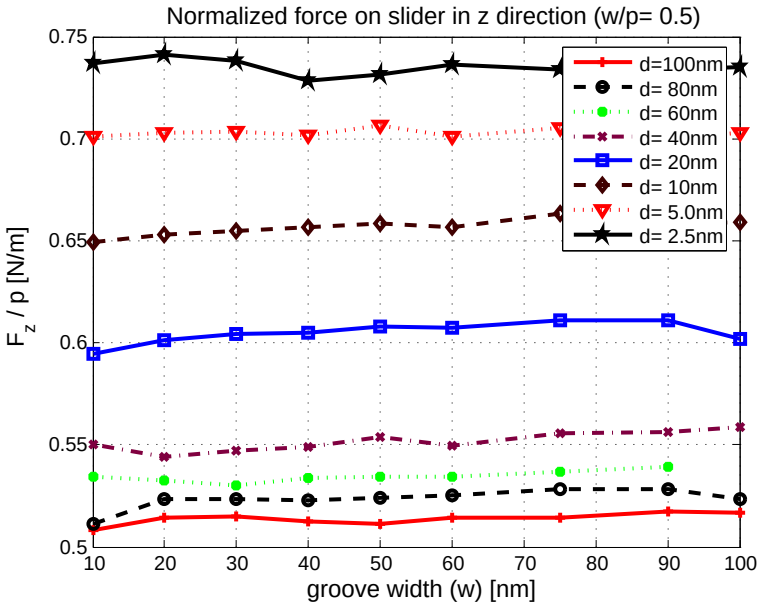

Figure 7.11: Air bearing force/track pitch versus groove width w ($w/p = 0.5$)

tolerances of wide grooves. Clearly, deep and wide grooves should be used in discrete track head/disk interfaces to minimize air bearing force variations as a function of disk manufacturing tolerances. Wide grooves will result in very narrow land areas, resulting in high air bearing pressure peaks as was shown in [3, 4]. High pressure peaks will affect the lubricant distribution on the land areas and possibly cause lubricant depletion.

In Figure 7.10 the effect of groove dimensions on the air bearing force is plotted for typical discrete track recording head/disk interface systems. One observes a

similar dependence of the normalized air bearing force (air bearing force/track pitch) on groove depth for all groove dimensions. This result indicates that the effect of groove dimensions on the overall air bearing force is small. The results presented in Figure 7.11 confirm this result. Here, it is shown that the normalized air bearing force (air bearing force/track pitch) depends on the groove depth only, but not on the groove width. The results also suggest that groove width or groove depth does not affect the normalized air bearing force. Thus, small grooves will have the same effect on the overall air bearing force as wide grooves.

7.5 Acknowledgement

This chapter is a partial reprint of material as it appears in: "***Direct Simulation Monte Carlo Method for the Simulation of Rarefied Gas Flow in Discrete Track Head/Disk Interfaces***", by Maik Duwensee, Shoji Suzuki, Judy Lin, David Wachenschwanz, and Frank E. Talke, submitted for publication to ASME Journal of Tribology (2007). The dissertation author was the primary researcher and author and the co-authors listed in this publication directed and supervised the research which forms the basis for this chapter.

Bibliography

[1] Alexander, F., Garcia, A., and Alder, B. *Direct Simulation Monte Carlo for Thin-film Bearings*. Phys. Fluids, 6 (12):3854–3860, 1994.

[2] Bird, G. *Molecular Gas Dynamics and the Direct Simulation of Gas Flows*. Oxford University Press, 1994.

[3] Duwensee, M., Suzuki, S., Lin, J., Wachenschwanz, D., and Talke, F. *Air Bearing Simulation of Discrete Track Recording Media*. IEEE Trans. Mag., 42 (10):2489–2491, 2006.

[4] Duwensee, M., Suzuki, S., Lin, J., Wachenschwanz, D., and Talke, F. *Simulation of the Head Disk Interface for Discrete Track Media*. Microsystem Technologies, Published Online, 2006.

[5] Huang, W. and Bogy, D. *An Investigation of a Slider Air Bearing with a Asperity Contact by a Three Dimensional Direct Simulation Monte Carlo Method*. IEEE Trans. Mag., 34 (4):1810–1812, 1998.

[6] Huang, W., Bogy, D., and Garcia, A. *Three-Dimensional Direct Simulation Monte Carlo Method for Slider Air Bearings*. Phys. Fluids, 9 (6):1764–1769, 1997.

[7] Liu, N. and Ng, E.-K. *The Posture Effects of a Slider Air Bearing on its Performance with the Direct Simulation Monte Carlo Method*. J. Micromech. Microeng., 11:463–473, 2001.

[8] Wang, H. and Liu, T. *Air-Flow Velocity Effects on Air Bearing with Grooved Disk Surface in Near-Field Optical Disk Drives*. Phys. Fluids, 18, 2006.

8

Summary and Conclusions

The year 2006 marked the fiftieth anniversary of the invention of the computer hard disk drive. Within those fifty years, the areal storage density of computer hard disk drives increased by a factor of seventy five million from initially two thousand bits per square inch to currently one hundred and fifty gigabits per square inch. At the same time the spacing between the recording slider and the rotating disk was reduced by a factor of approximately three thousand from initially twenty thousand nanometers to currently seven nanometers.

To measure the clearance between slider and disk, a voltage pulsing experiment was developed. Clearance is defined as the spacing between the highest asperities on the disk and slider surface. Voltage pulses between recording slider and rotating disk were used to add an electrostatic force component to the head/disk interface.

The force component is attractive in character and reduces the spacing between slider and disk. Laser Doppler vibrometry and acoustic emission were used to monitor the spacing change and detect contact events between slider and disk. The effect of disk profile microwaviness and roughness on the clearance was investigated.

Disk surface profiles consist of three frequency regions. These are the low frequency region, often referred to as waviness, the intermediate frequency region, generally called microwaviness, and the high frequency region, generally called roughness. The waviness has the highest amplitude contributions to the disk surface profile, while the disk roughness contributes least to the amplitudes of the disk surface profile. The head/disk interface is designed so that the slider follows the waviness of the disk profile. The slider cannot follow the microwaviness or disk roughness. Therefore, one would expect disk roughness and microwaviness to influence clearance, since disks with high roughness or microwaviness amplitudes are more likely to induce contact due to asperities reaching higher towards the slider.

A dependence of clearance on disk roughness was not found, given the samples used. However, the experimental results indicate that disk microwaviness influences clearance. For the samples used, a reduction in the amplitude of microwaviness of one nanometer yields a clearance increase of three nanometers. It can be concluded that the smaller the microwaviness, the larger the permissible

clearance change prior to the onset of contact. Furthermore, the development of disk manufacturing processes with independent roughness and microwaviness is recommended to control the clearance in the head/disk interface.

With reduced slider disk clearance, the magnetic recording disk should be homogeneous in terms of roughness, microwaviness and lubricant distribution. Microwaviness variations or variations in the thickness of the lubricant layer on the disk surface can result in slider flying height modulations. To visualize slider flying height modulations over the entire disk surface a method was introduced which monitors slider acoustic emission and slider bounce as the slider sweeps over the disk. Flying height modulation maps and microwaviness maps can also be measured using this technique. A change in the write protrusion due to thermal heating changes the slider to disk compliance and increases the sensitivity of the method.

The super-paramagnetic effect and signal-to-noise ratio related problems are of most concern for a further increase in areal storage density of future computer hard disk drives. Heat assisted magnetic recording and patterned media recording are likely to be used for the increase in areal storage density of future hard disk drives. Surface pattern on magnetic recording disks increase the complexity of the rarefied gas flow in the head/disk interface. A finite element based steady state air bearing simulation program was modified and applied to study discrete track head/disk interfaces. Air bearing simulations of discrete track head/disk interfaces

have been performed to investigate the steady state flying characteristics of sub-ambient pressure sliders flying over discrete track recording disks.

It was found that the slider flying height decreases linearly with increasing groove depth and increasing ratio of groove width to track pitch. An empirical equation was found to describe the flying height loss as a function of discrete track parameters used. The range in which the equation gives accurate results was estimated using a particular slider design as a test case. The slider pitch angle was found to be insensitive on discrete track parameters. The maximum pressure in a discrete track media head/disk interface increases with increasing groove depth and increasing ratio of discrete track groove width to discrete track pitch.

To investigate the effect of manufacturing tolerances and absolute groove dimension on the air bearing force, the particle based direct simulation Monte Carlo method was used for the simulation of rarefied gas flow in a nano channel. The nano channel corresponds to the physical situation encountered in a discrete track recording head/disk interface.

The direct simulation Monte Carlo simulations conducted in this study have shown that wide and deep grooves result in a reduction of the air bearing force keeping all other parameters constant. Both the friction and air bearing force approach a constant value for deep and wide grooves. In addition, a steep gradient of the friction and air bearing force was found for shallow and narrow grooves.

This indicates that the friction and air bearing force will be more affected by manufacturing tolerances in the case of shallow and narrow grooves than in the case of deep and wide grooves. Based on this result, deep and wide grooves are recommended for the design of discrete track recording head/disk interfaces to minimize air bearing force variations as a function of disk manufacturing tolerances. However, wide grooves will result in very narrow land areas, resulting in high and localized air bearing pressure peaks.

Finally, the effect of absolute groove dimensions on the air bearing force was investigated using the direct simulation Monte Carlo method. The air bearing force was found to be independent of the groove dimensions for the simulation parameters used. These results suggest that the absolute groove width and depth do not affect the air bearing force. Thus, small grooves will have the same effect on the air bearing force than large grooves.

A

Supplemental Information for Chapter 1

A.1 Surface Roughness Characterization

In this thesis, roughness is characterized by the centerline average roughness R_{cla} and the root mean square roughness R_{rms}.

Figure A.1 shows a surface height profile $z = f(x)$. The centerline average roughness, R_{cla}, of the profile in Figure A.1 is defined as

$$R_{cla} = \frac{1}{L}\int_0^L |z(x)|dx, \tag{A.1}$$

where $z(x)$ is the surface height measured relative to the mean of the surface. L is the length of the profile sample. The root mean square roughness, R_{rms}, of the

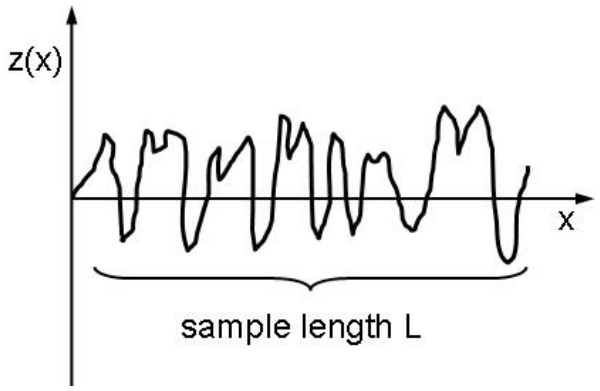

Figure A.1: Height profile of surface with sample length L

profile is defined as

$$R_{rms} = \sqrt{\frac{1}{L}\int_0^L z^2(x)dx}. \tag{A.2}$$

A.2 Van der Waals Forces of the Head/Disk Interface

It has been shown that for spacings below $5nm$ *van der Waals* forces between slider and disk add a highly nonlinear component to the head/disk interface and have to be taken into account [14].

To describe *van der Waals* interactions between two molecules the *Lennard-Jones* potential

$$w_{LennardJones} = -\frac{C}{r^6} + \frac{D}{r^{12}} \tag{A.3}$$

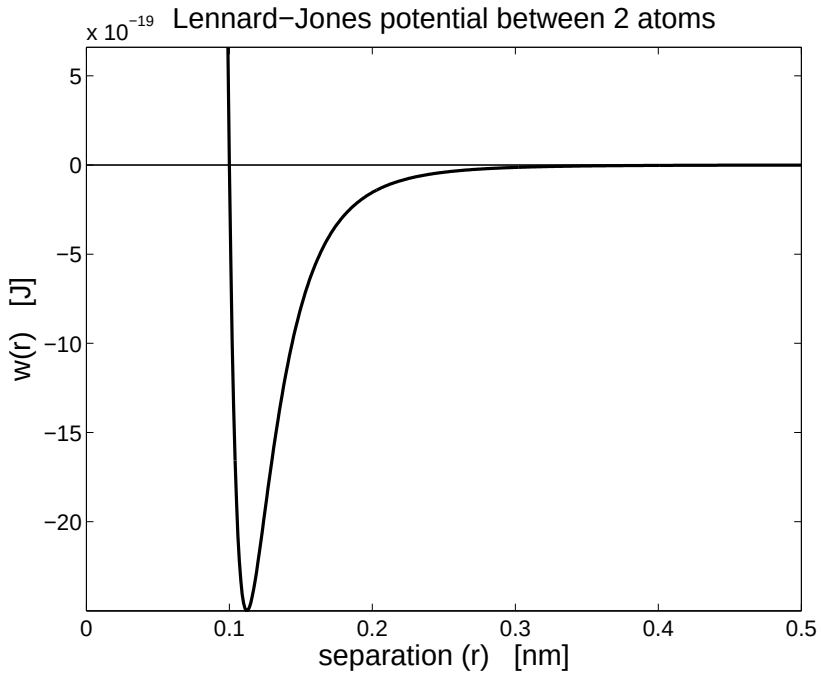

Figure A.2: Lennard-Jones potential

is commonly used. C and D in equation A.3 are constants given by $C = 10^{-77} Jm^6$ and $D = 10^{-134} Jm^{12}$ and r is the separation between the two molecules. Figure A.2 shows schematically the potential as a function of the separation. As can be seen from Figure A.2, the potential has a well defined minimum. For separations smaller than the minimum the repulsive term D/r^{12} in equation A.3 becomes dominant. At large distances the term C/r^6 dominates in equation A.3.

The interaction force $F_{LennardJones}$ between two molecules can be calculated by taking the negative first derivative of equation A.3 with respect to the separation.

Performing this operation leads to

$$F_{LennardJones} = 6\frac{C}{r^7} - 12\frac{D}{r^{13}}. \tag{A.4}$$

To compute the *van der Waals* interaction potential between two macroscopic bodies, equation A.3 has to be integrated over all molecules of the two bodies. This approach was first published by Hamaker in 1937 [6]. He calculated that the interaction between two spherical bodies can be written as

$$W = -\frac{A}{6D}\frac{R_1 R_2}{R_1 + R_2}, \tag{A.5}$$

where D is the separation between the two particles and R_1, R_2 are the radii of the two spheres under consideration. The constant A is called the *Hamaker* constant. The value of A depends on the materials under investigation and the medium that separates them. The Hamaker constant can be calculated by

$$A = \pi^2 C \rho_1 \rho_2, \tag{A.6}$$

where C is the interaction constant from the Lennard Jones potential in equation A.3 and ρ_1 and ρ_2 are the number densities of the spheres 1 and 2, respectively.

To estimate the *van der Waals* interactions for the head/disk interface the Lennard-Jones potential (equation A.3) has to be integrated over all particles of the slider and the disk. This integration has to be performed numerically due to the complex shape and geometry of the air bearing slider [9]. Furthermore, the Hamaker constant for the materials used in the head/disk interface has to be

known. Figure 1.35 (chapter 1) shows a schematic of the head/disk interface. As can be seen from the figure, the interface consists of multiple layers of different materials. The determination of the Hamaker constant for multi-layer interfaces using bulk properties of the interface materials has been presented by Israelachvili [8]. However, some properties of materials used in the head/disk interface are unknown and an experimental technique for the determination of the Hamaker constant is desirable. Such a technique is described next.

A.3 Experimental Determination of the Hamaker Constant

Figure 1.35 (chapter 1) shows the schematic of the head/disk interface, indicating that a number of thin films are present on both the slider and the disk. The calculation of the Hamaker constant for multilayered interfaces using material bulk properties has been proposed by Israelachvili [8]. The bulk properties needed are refractive indices or dielectric constants. Unfortunately, those values are not known for materials used for the head/disk interface. Therefore, an experimental determination of the Hamaker constant is necessary.

Using atomic force microscopy (AFM) with a spherical tip as shown in Figure A.3, one can determine the Hamaker constant for any material interface. The

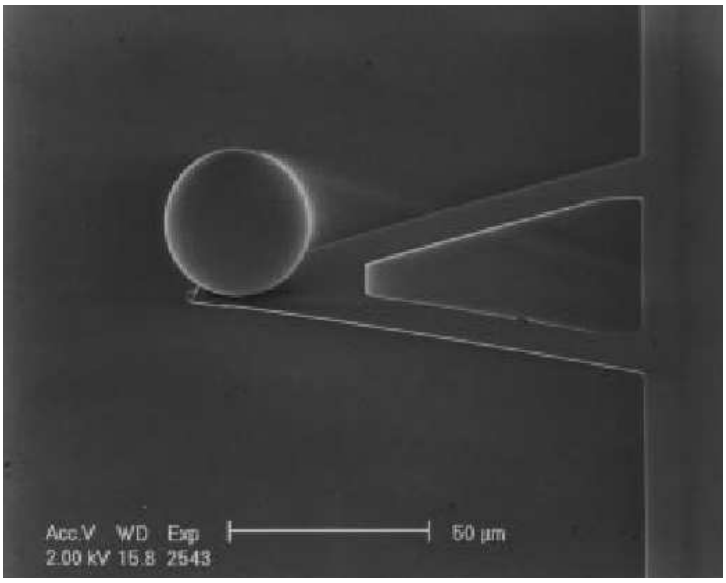

Figure A.3: Customized atomic force microscopy tip

determination is performed by comparison of a theoretical solution and experimental data for the interaction in the interface. The theoretical model can be obtained by integrating equation A.3 for the case of a spherical particle and a plane half space. The integration yields

$$F_{vdW} = -\frac{AR}{6D^2}, \tag{A.7}$$

where A is the Hamaker constant, R is the radius of the sphere and D is the distance between the sphere and the plane (Figure A.5). Comparison of the theoretical solution A.7 with experimental data (from force/distance measurements obtained using atomic force microscopy) allows the determination of the Hamaker constant A by fitting the experimental results to the theoretical solution [1, 2].

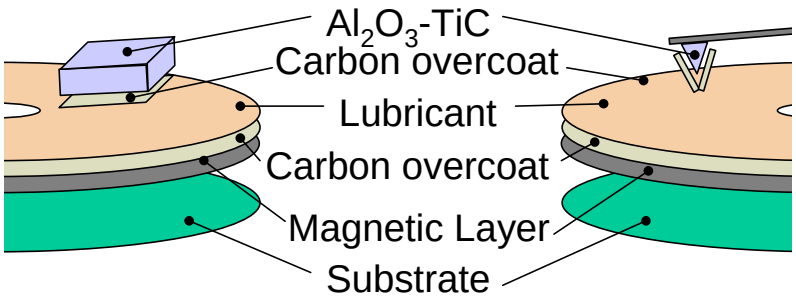

Figure A.4: Multilayered head/disk interface structure

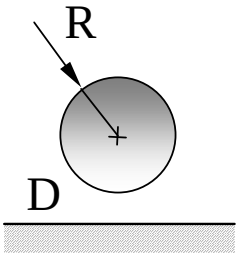

Figure A.5: Definition of spherical particle interacting with plane surface

To determine the Hamaker constant A for a typical head/disk interface, it is necessary to simulate the multilayered structure of the head/disk interface in the atomic force microscopy interface. This can be done by using a disk from a computer hard disk drive as the sample and choosing alumina titanium carbide ($Al_2O_3 - TiC$) as the atomic force microscopy tip material. Additionally, a carbon layer has to be applied to the atomic force microscopy tip. A schematic of simulating the head/disk interface in the atomic force microscopy experiment is shown in Figure A.4.

B

Supplemental Information for Chapter 2 and 3

B.1 Laser Doppler Vibrometry

For the experiments described in chapter 2 and 3 laser Doppler vibrometry (LDV) equipment was used for the investigation of the out of plane motion of slider and disk. Laser Doppler vibrometry has been used to measure the slider dynamics of head/disk interfaces for more than twenty years [3, 5]. Bogy and Talke (1985) [3] reported the use of laser Doppler vibrometry for the modal analysis of the slider air bearing, the rotating disk, and the suspension arm.

Laser Doppler vibrometry uses laser light to measure the velocity of an mov-

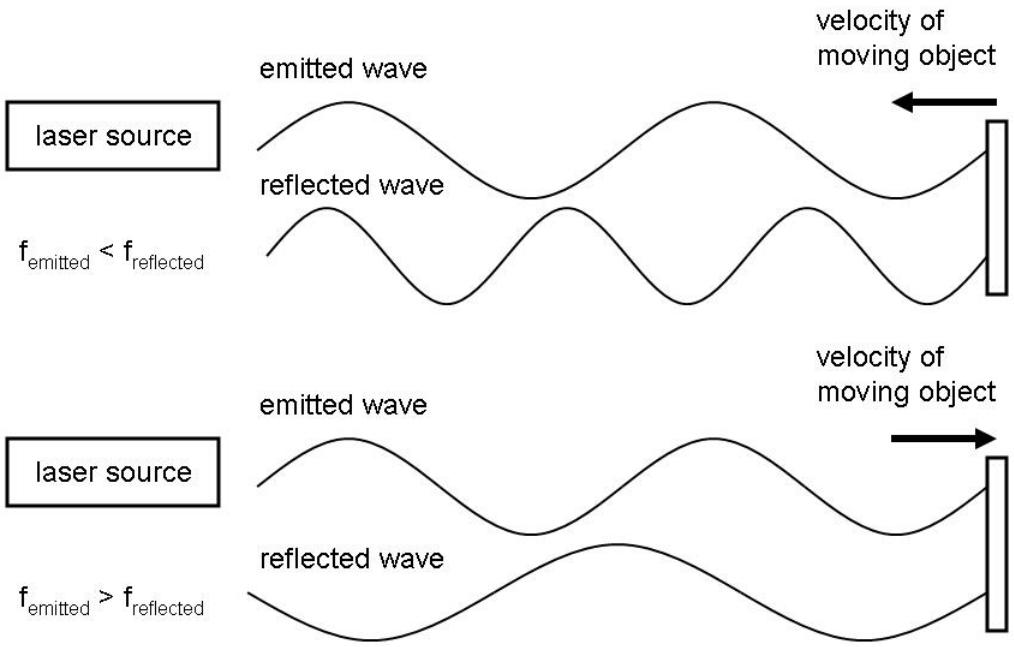

Figure B.1: Schematic of Doppler effect

ing object. In a laser Doppler vibrometer the Doppler effect and principles of interferometry are used.

The Doppler effect is named after Christian Doppler who first reported the effect in *Über das farbige Licht der Doppelsterne und einiger anderer Gestirne des Himmels - Versuch einer das Bradleysche Theorem als integrirenden Theil in sich schliessenden allgemeineren Theorie* (On the coloured light of the binary refracted stars and other celestial bodies - Attempt of a more general theory including Bradley's theorem as an integral part) [4]. The Doppler effect as used in laser Doppler vibrometry measures the change in frequency of laser light after

reflection from the surface of an object moving relative to the laser source. Figure B.1 shows a schematic of the frequency change of laser light after reflection from a moving surface. Two cases are depicted in the figure. In the first case the object is moving towards the laser light source, in the second case the object is moving away from the laser light source. As can be seen from Figure B.1, the frequency of laser light reflected from an object moving towards the laser source is higher than the frequency for the case of reflection of an object moving away from the laser source. The measured frequency shift f_{shift} can be written as

$$f_{shift} = 2\frac{v}{\lambda}, \tag{B.1}$$

where v is the relative velocity of the laser source and the moving object, and λ is the wavelength of the laser [11].

To measure the frequency shift at a fixed wavelength of the emitted laser, optical interferometry is used [11]. Defining $I_{emitted}$ and $I_{reflected}$ as the intensity of the light emitted from the laser source and the intensity of the reflected light, respectively, the total intensity I_{total} can be written as

$$I_{total} = (I_{emitted} + I_{reflected}) + \underbrace{2\sqrt{I_{emitted}I_{reflected}}\cos\left(2\pi\frac{(r_{emitted} - r_{reflected})}{\lambda}\right)}_{\text{interference term}}, \tag{B.2}$$

where $r_{emitted}$ is the path length of the emitted light and $r_{reflected}$ is the path length of the reflected light. The second term in equation B.2 is called the interference

term and relates to the differences in the path length of the emitted and reflected beam. If this difference is an integer multiple of the laser wavelength λ, constructive interference occurs. If the two beams have a path length difference of one half the wavelength, destructive interference occurs.

B.2 Acoustic Emission

For the experiments described in chapter 2 and 3 acoustic emission (AE) transducers have been used for the detection of contact between slider and disk. Acoustic emission waves are stress waves in materials emitted from the rapid release of strain energy in materials. Acoustic emission has been successfully applied to a wide variety of engineering applications. Some applications are the non-destructive testing during manufacturing processes, monitoring of pressure vessels, or fatigue and corrosion studies of aircraft and aerospace structures [10].

Figure B.2 illustrates a typical acoustic emission setup. As seen in the figure, a acoustic emission stress wave travels from its source to the acoustic emission sensor (transducer) after a rapid release of strain energy. The rapid release of strain energy is a function of the applied external load. The transducer is generally made from a piezo-electric crystal. The acoustic emission stress wave causes a voltage in the crystal. The voltage is measured.

In this thesis acoustic emission is used as a means to detect contact between

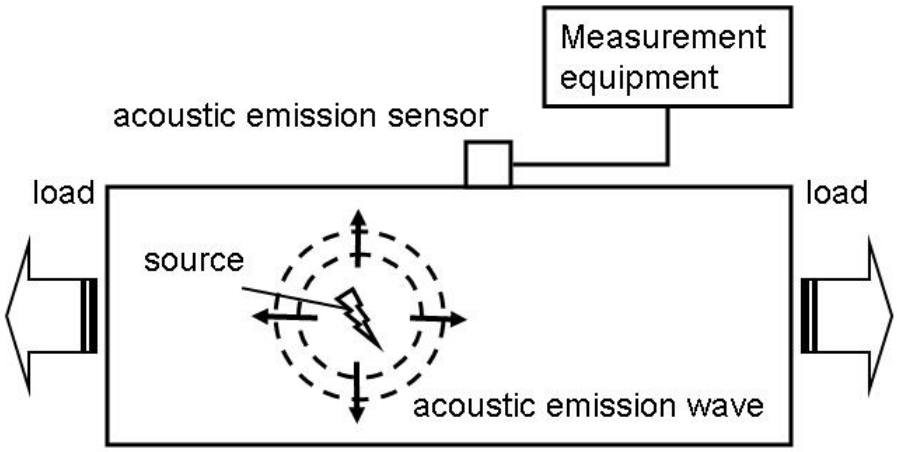

Figure B.2: Schematic of acoustic emission measurement

slider and disk of the head/disk interface. When the slider contacts the disk, acoustic emission stress waves are released within the slider, gimbal or suspension. The stress waves are detected by an acoustic emission sensor attached near the suspension.

C

Supplemental Calculations for Chapter 4

C.1 Order of Magnitude Analysis

To determine the relevant terms of equation 4.4 in section 4.1, an order-of-magnitude analysis is needed. The order-of-magnitude analysis is outlined in this appendix. First the continuity and the momentum equations (equations 4.4 and 4.12) will be nondimensionalized. Here only the steady state case of an infinitely wide bearing is considered. The coordinates x_i (or x, y, z) and velocities u_i (u, v, w) are normalized by the characteristic dimensions B and h_{min} of the slider

bearing (Figure 4.1), i.e.,

$$\tilde{x} = \frac{x}{B}, \quad \tilde{y} = \frac{y}{L} \tag{C.1}$$

$$\tilde{z} = \frac{z}{h_{min}}, \tag{C.2}$$

The mass density is normalized by the ambient density,

$$\tilde{\rho} = \frac{\rho}{\rho_a}. \tag{C.3}$$

The normalization of the pressure can be written as

$$\tilde{p} = \frac{p}{\bar{p}}, \tag{C.4}$$

where $\bar{p}$ is unknown and has to be determined. The velocities u and v are normalized by the disk velocity components U and V (Figure 4.1),

$$\tilde{u} = \frac{u}{U}, \; \tilde{v} = \frac{v}{V}. \tag{C.5}$$

The velocity component w is normalized by the linear velocity component in the z direction W

$$\tilde{w} = \frac{w}{W}, \tag{C.6}$$

where W is unknown, but can be determined by inserting equations C.1, C.2, C.3, C.4, C.5, and C.6 into the nondimensionalized steady state continuity equation.

$$\frac{U\rho_a}{B}\frac{\partial}{\partial\tilde{x}}(\tilde{\rho}\tilde{u}) + \frac{W\rho_a}{h_{min}}\frac{\partial}{\partial\tilde{z}}(\tilde{\rho}\tilde{w}) = 0. \tag{C.7}$$

Both terms in equation C.7 have to be of the same order; hence, the velocity scale W can be written as

$$W = \frac{h_{min}}{B} U. \tag{C.8}$$

To determine the correct pressure scale $\bar{p}$ equations C.1, C.3, C.5 and C.8 are substituted into the x-momentum equation 4.4:

$$\frac{\rho_a U B}{\mu}\left(\frac{h_{min}}{B}\right)^2\left[\frac{\partial}{\partial\tilde{x}}\left(\tilde{\rho}\,\tilde{u}^2\right)+\frac{\partial}{\partial\tilde{z}}\left(\tilde{\rho}\,\tilde{u}\tilde{w}\right)\right]= \tag{C.9}$$
$$-\frac{\bar{p}\,h_{min}^2}{\mu\,UB}\frac{\partial\tilde{p}}{\partial\tilde{x}}+\left(\frac{h_{min}}{B}\right)^2\left(\frac{4}{3}\frac{\partial^2\tilde{w}}{\partial\tilde{x}\partial\tilde{z}}+\frac{1}{3}\frac{\partial^2\tilde{u}}{\partial\tilde{x}^2}\right)+\frac{\partial^2\tilde{u}}{\partial\tilde{z}^2}.$$

Due to the assumption that $h_{min} \ll B$, the terms containing $(h_{min}/B)^2$ are small compared to unity and can be neglected in equation C.9. This leads to

$$\frac{\bar{p}\,h_{min}^2}{\mu\,UB}\frac{\partial\tilde{p}}{\partial\tilde{x}} = \frac{\partial^2\tilde{u}}{\partial\tilde{z}^2}. \tag{C.10}$$

Equation C.10 expresses the fundamental principle in lubrication theory: the pressure forces balance the viscous forces. Furthermore, the correct scale for normalizing the pressure is found by

$$\bar{p} = \frac{\mu\,UB}{h_{min}^2}. \tag{C.11}$$

Thus, all dimensionless variables in the lubrication problem have been defined:

$$\tilde{x} = \frac{x}{B}, \qquad \tilde{y} = \frac{y}{L}, \qquad \tilde{z} = \frac{z}{h_{min}}, \tag{C.12}$$
$$\tilde{\rho} = \frac{\rho}{\rho_a}, \quad \tilde{p} = \frac{p h_{min}^2}{\mu U B}, \quad \tilde{u} = \frac{u}{U},$$
$$\tilde{v} = \frac{v}{V}, \quad \tilde{w} = \frac{wB}{h_{min}U}.$$

Introducing the results C.12 into the momentum equation for the $z-$direction yields:

$$Re^* \left(\frac{h_{min}}{B}\right)^2 \left[\frac{\partial}{\partial \tilde{z}}\left(\tilde{\rho}\,\tilde{w}^2\right) + \frac{\partial}{\partial \tilde{x}}\left(\tilde{\rho}\,\tilde{u}\tilde{w}\right)\right] = \tag{C.13}$$
$$-\frac{\partial \bar{p}}{\partial \tilde{z}} + \left(\frac{h_{min}}{B}\right)^2 \left[\left(\frac{4}{3}\frac{\partial^2 \tilde{u}}{\partial \tilde{x}\partial \tilde{z}} + \frac{1}{3}\frac{\partial^2 \tilde{w}}{\partial \tilde{z}^2}\right) + \left(\frac{h_{min}}{B}\right)^2 \frac{\partial^2 \tilde{w}}{\partial \tilde{x}^2}\right],$$

where Re^* is the modified Reynolds number defined as

$$Re^* = \frac{\rho_a U B}{\mu}\left(\frac{h_{min}}{B}\right)^2 \tag{C.14}$$

By virtue of the fact that $h_{min} \ll B$, all terms containing $(h_{min}/B)^2$ vanish and equation C.13 reduces to

$$\frac{\partial \tilde{p}}{\partial \tilde{z}} = 0. \tag{C.15}$$

Equation C.15 implies that there is no pressure gradient in the vertical direction.

Writing Equation C.10 in dimensional form using equation C.12 yields

$$\frac{\partial p}{\partial x} = \frac{\partial}{\partial z}\left(\mu \frac{\partial u}{\partial z}\right). \tag{C.16}$$

A similar order of magnitude analysis for the y-direction relates the pressure forces to the viscous forces in the y-direction according to

$$\frac{\partial p}{\partial y} = \frac{\partial}{\partial z}\left(\mu \frac{\partial v}{\partial z}\right). \tag{C.17}$$

C.2 Integration of the Continuity Equation

The integration of the continuity equation 4.12 over the film thickness is outlined in this appendix.

Rewriting equation 4.12 in integral form yields

$$\int_0^h \left[\frac{\partial \rho}{\partial t} + \frac{\partial}{\partial z}(\rho w) + \frac{\partial}{\partial x}(\rho u) + \frac{\partial}{\partial y}(\rho v)\right] dz = 0. \tag{C.18}$$

Reordering and integrating C.18 over the film thickness h yields:

$$\int_0^h \frac{\partial}{\partial z}(\rho w) dz = \rho w \mid_0^h = -\int_0^h \left[\frac{\partial \rho}{\partial t} + \frac{\partial}{\partial x}(\rho u) + \frac{\partial}{\partial y}(\rho v)\right] dz. \tag{C.19}$$

The vertical velocity of the flow w at the disk surface $z = 0$ is zero ($w(0) = 0$). The vertical velocity at the slider $w(h)$ can be written as:

$$w(h) = \frac{\partial h}{\partial t} + u \mid_h \frac{\partial h}{\partial x} + v \mid_h \frac{\partial h}{\partial y}. \tag{C.20}$$

The last two terms in C.20 are zero, since no slip is assumed at the boundary of the slider. The term $\partial h/\partial t$ is the velocity of the slider. Equation C.20 can be reduced to:

$$w(h) = \frac{\partial h}{\partial t}. \tag{C.21}$$

Substituting equation C.21 into equation C.19 one obtains

$$\rho \frac{\partial h}{\partial t} = -\int_0^h \left[\frac{\partial \rho}{\partial t} + \frac{\partial}{\partial x}(\rho u) + \frac{\partial}{\partial y}(\rho v)\right] dz. \tag{C.22}$$

The differentiation and integration of all three terms on the right hand side of equation C.22 can be exchanged by employing the Leibnitz rule,

$$\frac{\partial}{\partial x}\int_{y=a(x)}^{y=b(x)} f(x,y)dy = \int_a^b \frac{\partial f}{\partial x}dy + \frac{\partial b}{\partial x}f(y=b,x) - \frac{\partial a}{\partial x}f(y=a,x), \qquad \text{(C.23)}$$

Invoking the Leibnitz rule on equation C.22 results in:

$$\rho\frac{\partial h}{\partial t} = -\frac{\partial}{\partial t}\int_0^h \rho dz + \rho\frac{\partial h}{\partial t} - \frac{\partial}{\partial x}\int_0^h \rho u dz + \frac{\partial h}{\partial x}\rho u\mid_{z=h} - \frac{\partial}{\partial y}\int_0^h \rho v dz + \frac{\partial h}{\partial y}\rho v\mid_{z=0}. \qquad \text{(C.24)}$$

The no-slip condition at the boundary of the slider has to be applied to equation C.24. Thus, the terms $\frac{\partial h}{\partial x}\rho u\mid_{z=h}$ and $\frac{\partial h}{\partial y}\rho v\mid_{z=0}$ are equal to zero. Equation C.24 reduces to

$$\frac{\partial \rho h}{\partial t} = -\frac{\partial}{\partial x}\int_0^h \rho u dz - \frac{\partial}{\partial y}\int_0^h \rho v dz. \qquad \text{(C.25)}$$

Substituting the ideal gas law 4.13, and the velocity profiles 4.10, 4.11 into equation C.25 and integrating the new equation yields the two dimensional Reynolds equation for compressible flow

$$\frac{\partial}{\partial x}\left(ph^3\frac{\partial p}{\partial x}\right) + \frac{\partial}{\partial y}\left(ph^3\frac{\partial p}{\partial y}\right) = 6\mu\left(U\frac{\partial ph}{\partial x} + V\frac{\partial ph}{\partial y}\right) + 12\mu\frac{\partial ph}{\partial t}. \qquad \text{(C.26)}$$

.

C.3 Element Stiffness Matrix

For each element in a finite element formulation the field variables of the differential equation are approximated by shape functions. The shape functions are

also referred to as interpolation functions. Using 4-node elements the pressure in the physical space is interpolated by

$$p(x,y) = \sum_{i=1}^{4} N_i(x,y)\ p_i, \tag{C.27}$$

where N_i are the shape functions corresponding to node i and p_i is the pressure at node i. Similarly, one can define the pressure interpolation in the isoparametric space (Figure 4.3) by

$$p(r,s) = \sum_{i=1}^{4} N_i(r,s)\ p_i, \tag{C.28}$$

where r and s are the coordinates in the isoparametric space. To transform the physical coordinates into the isoparametric space the same interpolation functions are used

$$\begin{aligned} x &= \sum_{i=1}^{4} N_i(r,s)\ x_i \\ y &= \sum_{i=1}^{4} N_i(r,s)\ y_i, \end{aligned} \tag{C.29}$$

where x_i and y_i are the coordinates of node i. In the air bearing simulator developed at the Center for Magnetic Recording Research (CMRR), bilinear quadrilateral elements and linear triangular elements are implemented [12]. For the quadrilateral

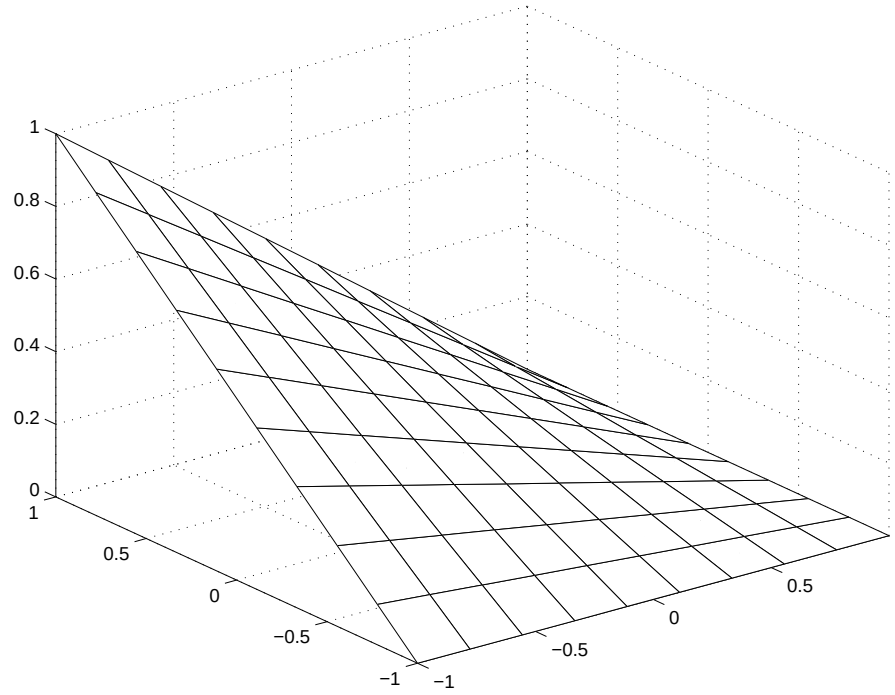

Figure C.1: Bilinear shape function N_4

bilinear elements the shape functions can be written as

$$\begin{aligned} N_1(r,s) &= \frac{1}{4}(1-r)(1-s) \\ N_2(r,s) &= \frac{1}{4}(1+r)(1-s) \\ N_3(r,s) &= \frac{1}{4}(1+r)(1+s) \\ N_4(r,s) &= \frac{1}{4}(1-r)(1+s). \end{aligned} \tag{C.30}$$

A graphical representation of the shape function N_4 is shown in Figure C.1 To implement the assumptions C.27 and C.29 in equation 4.37, the derivatives of the shape functions with respect to the isoparametric coordinates r and s are needed. The transformation of the derivatives from the physical space into the isoparamet-

ric space can be performed in four steps. First, an infinitesimal small element of the isoparametric space (dr, ds) is transformed in an infinitesimal small element of the physical space (dx, dy). Second, the transformation of the first step is inverted. Third, a formal definition of the inverse transformation is given. Fourth, a comparison between the results of the second and third step yields the expressions for the derivatives in the physical space x and y in terms of the isoparametric coordinates r and s.

The transformation of an infinitesimal small element of the isoparametric space (dr, ds) in an infinitesimal small element of the physical space (dx, dy) can be written as

$$\begin{Bmatrix} dx \\ dy \end{Bmatrix} = \begin{bmatrix} \frac{\partial x}{\partial r} & \frac{\partial x}{\partial s} \\ \frac{\partial y}{\partial r} & \frac{\partial y}{\partial s} \end{bmatrix} \begin{Bmatrix} dr \\ ds \end{Bmatrix}. \tag{C.31}$$

The matrix in equation C.31 is the Jacobian matrix $\boldsymbol{J}$. Multiplying equation C.31 with the inverse Jacobian yields

$$\begin{Bmatrix} dr \\ ds \end{Bmatrix} = \frac{1}{\det \boldsymbol{J}} \begin{bmatrix} \frac{\partial y}{\partial s} & -\frac{\partial x}{\partial s} \\ -\frac{\partial y}{\partial r} & \frac{\partial x}{\partial r} \end{bmatrix} \begin{Bmatrix} dx \\ dy \end{Bmatrix}. \tag{C.32}$$

The formal definition of the inverse transformation is given by

$$\begin{Bmatrix} dr \\ ds \end{Bmatrix} = \begin{bmatrix} \frac{\partial r}{\partial x} & \frac{\partial r}{\partial y} \\ \frac{\partial s}{\partial x} & \frac{\partial s}{\partial y} \end{bmatrix} \begin{Bmatrix} dx \\ dy \end{Bmatrix}. \tag{C.33}$$

Comparing equations C.32 and C.33 yields the desired derivatives

$$\begin{aligned}
\frac{\partial r}{\partial x} &= \frac{1}{\det \boldsymbol{J}} \frac{\partial y}{\partial s} \\
\frac{\partial r}{\partial y} &= -\frac{1}{\det \boldsymbol{J}} \frac{\partial x}{\partial s} \\
\frac{\partial s}{\partial x} &= -\frac{1}{\det \boldsymbol{J}} \frac{\partial y}{\partial r} \\
\frac{\partial s}{\partial y} &= \frac{1}{\det \boldsymbol{J}} \frac{\partial x}{\partial r}.
\end{aligned} \tag{C.34}$$

The results of equation C.34 can be used to express the first derivatives of a function $f = f(x, y)$ in terms of the isoparametric coordinates r and s. Applying the chain rule of differentiation to function f and using the equation C.34 one obtains

$$\begin{aligned}
\frac{\partial f}{\partial x} &= \frac{\partial f}{\partial r}\frac{\partial r}{\partial x} + \frac{\partial f}{\partial s}\frac{\partial s}{\partial x} = \quad \frac{\partial f}{\partial r}\frac{1}{\det \boldsymbol{J}}\frac{\partial y}{\partial s} - \frac{\partial f}{\partial s}\frac{1}{\det \boldsymbol{J}}\frac{\partial y}{\partial r} \\
\frac{\partial f}{\partial y} &= \frac{\partial f}{\partial r}\frac{\partial r}{\partial y} + \frac{\partial f}{\partial s}\frac{\partial s}{\partial y} = -\frac{\partial f}{\partial r}\frac{1}{\det \boldsymbol{J}}\frac{\partial x}{\partial s} + \frac{\partial f}{\partial s}\frac{1}{\det \boldsymbol{J}}\frac{\partial x}{\partial r}.
\end{aligned} \tag{C.35}$$

Applying equation C.35 to equation C.29, one can write the first derivatives of a function $f = f(x, y)$ with respect to the coordinates r and s of the isoparametric space as

$$\begin{Bmatrix} \dfrac{\partial f}{\partial x} \\ \dfrac{\partial f}{\partial y} \end{Bmatrix} = \frac{1}{\det \boldsymbol{J}} \begin{bmatrix} \displaystyle\sum_{k=1}^{4} \frac{\partial N_k}{\partial s} y_k & -\displaystyle\sum_{k=1}^{4} \frac{\partial N_k}{\partial r} y_k \\ -\displaystyle\sum_{k=1}^{4} \frac{\partial N_k}{\partial s} x_k & \displaystyle\sum_{k=1}^{4} \frac{\partial N_k}{\partial r} x_k \end{bmatrix} \begin{Bmatrix} \dfrac{\partial f}{\partial r} \\ \dfrac{\partial f}{\partial s} \end{Bmatrix}, \tag{C.36}$$

where the determinant of the Jacobian $\det \boldsymbol{J}$ can be computed from

$$\det \boldsymbol{J} = \left(\sum_{k=1}^{4} \frac{\partial N_k}{\partial r} x_k\right)\left(\sum_{k=1}^{4} \frac{\partial N_k}{\partial s} y_k\right) - \left(\sum_{k=1}^{4} \frac{\partial N_k}{\partial r} y_k\right)\left(\sum_{k=1}^{4} \frac{\partial N_k}{\partial s} x_k\right) \tag{C.37}$$

The results of equations C.36 and C.37 applied to the pressure approximation

of equation C.27 yields the first derivatives of the pressure

$$\frac{\partial p}{\partial x} = \sum_{i=1}^{4} \frac{\partial N_i}{\partial x} p_i \text{ and } \frac{\partial p}{\partial y} = \sum_{i=1}^{4} \frac{\partial N_i}{\partial y} p_i, \tag{C.38}$$

where the derivatives of the shape functions can be expressed according to

$$\begin{Bmatrix} \frac{\partial N_i}{\partial x} \\ \frac{\partial N_i}{\partial y} \end{Bmatrix} = \frac{1}{\det \boldsymbol{J}} \begin{bmatrix} \sum_{k=1}^{4} \frac{\partial N_k}{\partial s} y_k & -\sum_{k=1}^{4} \frac{\partial N_k}{\partial r} y_k \\ -\sum_{k=1}^{4} \frac{\partial N_k}{\partial s} x_k & \sum_{k=1}^{4} \frac{\partial N_k}{\partial r} x_k \end{bmatrix} \begin{Bmatrix} \frac{\partial N_i}{\partial r} \\ \frac{\partial N_i}{\partial s} \end{Bmatrix}. \tag{C.39}$$

An analytical integration is generally difficult when an isoparametric formulation is used in conjunction with the residual formulation 4.37, since the determinant of the Jacobian $\det \boldsymbol{J}$ is not constant. Therefore a numerical integration method is used. The so-called "Gaussian quadrature" approach is implemented in the CMRR air bearing simulation code. In Gaussian quadrature the integration is replaced by the sum of function evaluations at the Gauss points. Gaussian quadrature in two dimensions is given by

$$\int_{-1}^{1}\int_{-1}^{1} f(r,s)drds = \sum_{N=1}^{M}\sum_{m=1}^{N} f(r_m, s_n) w_m w_n \tag{C.40}$$

where w are weighting factors that depend on the number of Gauss points used. Gaussian quadrature is accurate for polynomials of order $2N-1$, where N is the number of Gauss points used.

In the CMRR air bearing simulator, quadrilateral bilinear elements are used. For such an element formulation the element equation 4.38 consists of a stiffness matrix $[\boldsymbol{k}]^e$ of dimension 4×4, a vector of unknowns $\{\boldsymbol{dp}\}^e$ of dimension 4×1,

and the right hand side vector $\{\boldsymbol{r}\}^e$ of dimension 4×1. The element equation can be written

$$\begin{bmatrix} k_{11} & k_{12} & k_{13} & k_{14} \\ k_{21} & k_{22} & k_{23} & k_{24} \\ k_{31} & k_{32} & k_{33} & k_{34} \\ k_{41} & k_{42} & k_{43} & k_{44} \end{bmatrix} \begin{Bmatrix} dp_1 \\ dp_2 \\ dp_3 \\ dp_4 \end{Bmatrix} = \begin{Bmatrix} r_1 \\ r_2 \\ r_3 \\ r_4 \end{Bmatrix}. \tag{C.41}$$

Substituting the shape functions C.30 and their derivatives C.39 into the residual formulation 4.37, the elements of the stiffness matrix can be written

$$\begin{aligned} k_{ij} = \int_{-1}^{1}\int_{-1}^{1} \big\{ & \overline{Q} h^3 (\nabla p_0 \cdot \nabla N_i) N_j + \overline{Q} h^3 p_0 \nabla N_j \cdot \nabla N_i \\ & + 6\mu N_i (h\mathbf{V} \cdot \nabla N_j + N_j \mathbf{V} \cdot \nabla h) \big\} \det \boldsymbol{J} \; drds. \end{aligned} \tag{C.42}$$

Similarly, the right hand sight can be calculated by

$$r_i = -\int_{-1}^{1}\int_{-1}^{1} \big\{ p_0 h^3 (\nabla p_0 \cdot \nabla N_i) + 6\mu N_i \mathbf{V} \cdot (p_0 \nabla h + h \nabla p_0) \big\} \det \boldsymbol{J} \; drds. \tag{C.43}$$

A 2×2 Gaussian quadrature rule is used for the integration of equations C.42 and C.43.

The triangular element implementation realized in the CMRR simulator code is adopted from Hughes [7]. Here, a triangular element is considered a degenerated quadrilateral element. Figure C.2 shows the process of degenerating a quadrilateral element into a triangular element.

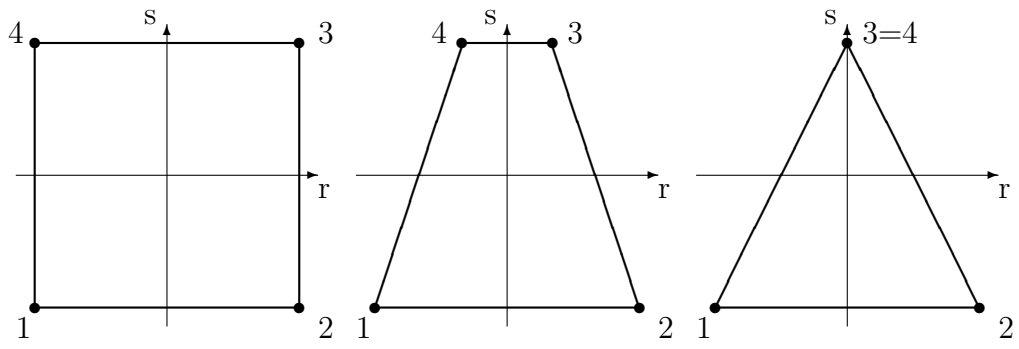

Figure C.2: Triangle element as a degenerated quadrilateral element

Using a degenerated quadrilateral element for the implementation of triangular elements allows the use of an existing quadrilateral element implementation in the simulation program. During the reading of the connectivity information the coordinates of node number three of each element have to be assigned to node three and four in the quadrilateral element. To implement a triangular element without an existing quadrilateral formulation, the shape functions would have the form

$$\begin{aligned} N_1 &= \frac{1}{4}(1-r)(1-s) \\ N_2 &= \frac{1}{4}(1+r)(1-s) \\ N_3 &= \frac{1}{2}(1+s). \end{aligned} \tag{C.44}$$

These functions are visualized in Figures C.3 to C.5.

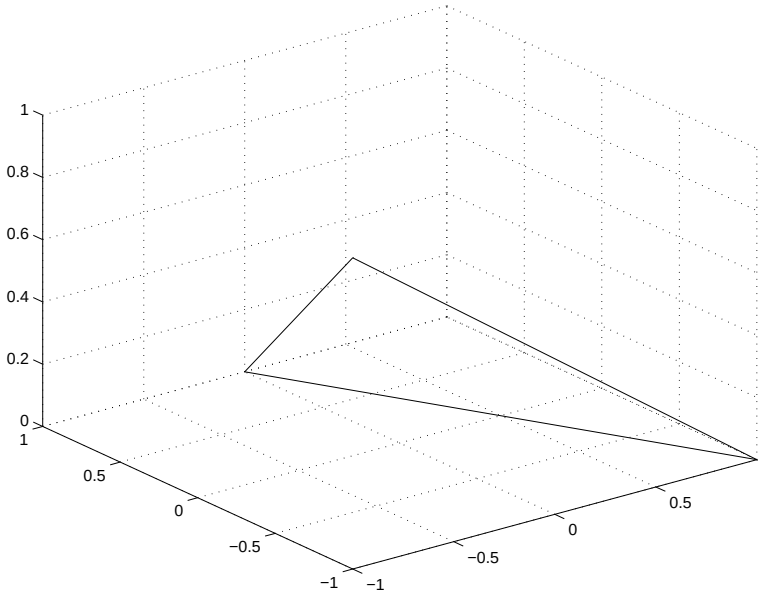

Figure C.3: Shape function N_1

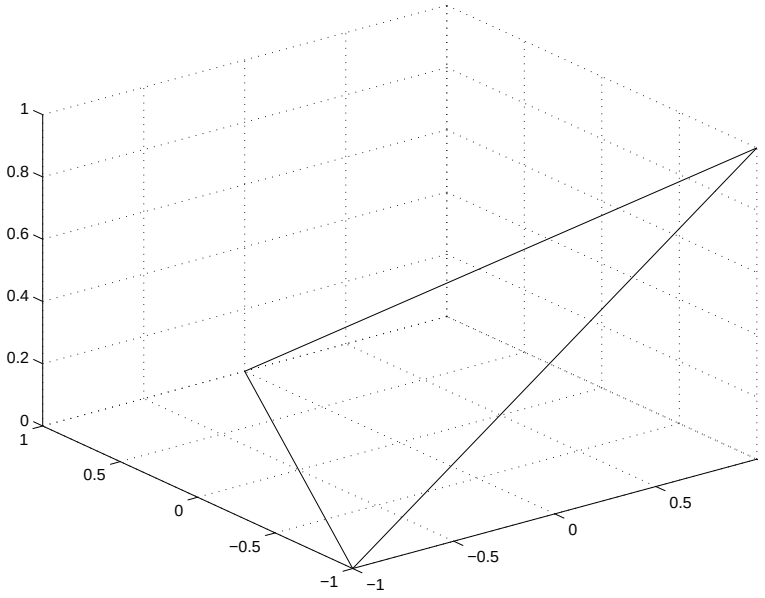

Figure C.4: Shape function N_2

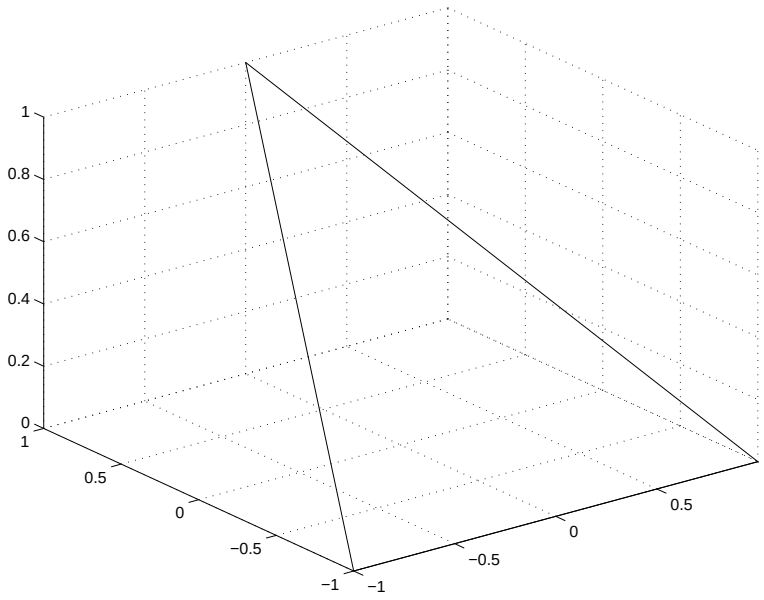

Figure C.5: Shape function N_3

C.4 Simultaneous Newton-Raphson Scheme for Steady State Slider Air Bearing Simulations

Chapter 4 outlines the mathematical modeling of the slider air bearing in computer hard disk drives. For steady state simulations the Reynolds equation and the slider equilibrium equation have to be satisfied simultaneously. In the CMRR simulator a simultaneous Newton-Raphson Scheme is implemented. The implementation of the scheme is described in this section.

The simultaneous Newton-Raphson Scheme is a powerful second order accurate method. To implement it, the stiffness matrix in equation 4.39 has to be expanded

by three rows and columns, corresponding to the three degrees of freedom of the slider and the slider equilibrium equations 4.44. The augmented matrix is not longer a banded matrix. Special consideration for storage and solution are necessary. In the CMRR simulator a sparse matrix scheme and a sparse matrix solver are implemented. The Newton-Raphson scheme is applied to the coupled system of equations. In partitioned form it can be written as

$$\begin{bmatrix} \dfrac{\partial \mathbf{R}}{\partial \mathbf{p}} & \dfrac{\partial \mathbf{R}}{\partial \xi} \\ -\dfrac{\partial \mathbf{F}}{\partial \mathbf{p}} & \mathbf{K_s} \end{bmatrix}^n \begin{bmatrix} \mathbf{dp} \\ \mathbf{d}\xi \end{bmatrix} = \begin{bmatrix} -\mathbf{R^n} \\ \mathbf{F^n} - \mathbf{F_{ext}} \end{bmatrix}, \tag{C.45}$$

where $\mathbf{R}$ is the discretized Reynolds equation rewritten in vector notation form,

$$\mathbf{R}(\xi, \mathbf{p}(\xi)) = \mathbf{0}, \tag{C.46}$$

and the other terms are related to the slider equilibrium equations 4.44

$$\mathbf{F}(\mathbf{p}(\xi)) - \mathbf{F_{ext}} = \mathbf{K_s}\mathbf{d}\xi. \tag{C.47}$$

A finite element formulation can be derived following the procedure described in section 4.3. Further descriptions can be found in [12].

The block diagram C.6 shows how the simultaneous Newton-Raphson scheme is implemented. To maintain convergence, the Newton Raphson scheme starts with an initial guess for the pressure distribution close to the expected solution. Providing the algorithm with this initial guess is difficult especially when new slider design are under investigation. Therefore the static pressure distribution

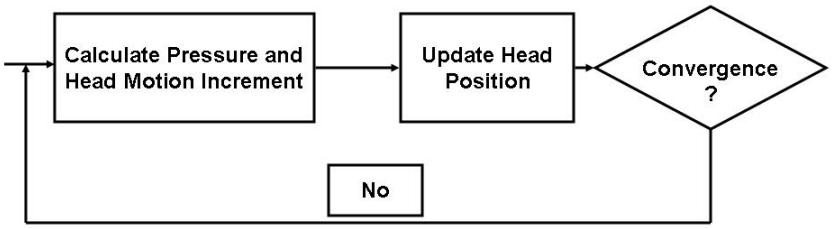

Figure C.6: Simultaneous Newton-Raphson scheme

is calculated first. To calculate the static pressure distribution an initial position between slider and disk is provided and the Reynolds equation is solved. After the static pressure has been calculated the Newton Raphson scheme iterates until an equilibrium position is found.

Bibliography

[1] Argento, C. and French, R. *Parametric Tip Model and ForceDistance Relation for Hamaker Constant Determination from Atomic Force Microscopy.* J. Appl. Phys., 80(11):6081–6090, 1996.

[2] Biggs, S. and Mulvaney, P. *Measurement of the Forces between Gold Surfaces in Water by Atomic Force Microscopy.* J. Chem. Phys., 100(11):8501–8505, 1994.

[3] Bogy, D. and Talke, F. *Laser Doppler Interferometry on Magnetic Recording Systems.* IEEE Trans. Magn., 21(5):1332–1337, 1985.

[4] Bretterbauer, K. et al. *Christian Doppler, Leben und Werk. Der Dopplereffekt.* Amt der Salzburger Landesregierung, 1988.

[5] Bushan, B. *Tribology and Mechanics of Magnetic Storage Devices.* Springer, 2nd edition, 1996.

[6] Hamaker, H. *The London van der Waals Attraction between Spherical Particles.* Physica (Amsterdam), 4:1058, 1937.

[7] Hughes, T. *The Finite Element Method.* Prentice-Hall, INC., 1987.

[8] Isrealachvili, J. *Intermolcular and Surface Forces.* Academic Press, 1992.

[9] Jagota, A. and Argento, C. *An Interface Stress Tensor.* J.Coll.Interf, 191:326–336, 1997.

[10] Physical Acoustics Corporation. *www.pacndt.com.*

[11] Polytec GmbH. *www.polytec.com.*

[12] Wahl, M., Lee, P., and Talke, F. *An Efficient Finite Element-Based Air Bearing Simulator for Pivoted Slider Bearings using Bi-Conjugate Gradient Algorithms*. STLE Trib. Trans., 39 (1), 1996.

[13] Weissner, S., Tonder, K., and Talke, F. *Surface Roughness Effects in Compressible Lubrication*. In *Proceedings of AUSTRIB 1998, Brisbane*. 1998.

[14] Wu, L. and Bogy, D. *Effects of the Intermolecular Forces on the Flying Attitude of Sub-5 NM Flying Height Air Bearing Sliders in Hard Disk Drives*. Trans. ASME, 124:562–567, 2002.